Thermal Acoustic Flow inside an Ultrasound Resonator

Enrico Corato

LUND
UNIVERSITY

Master's Thesis in Biomedical Engineering
Faculty of Engineering LTH
Department of Biomedical Engineering

Supervisors: Dr. Per Augustsson
Dr. Marco Rasponi

Cosupervisor: Dr. Wei Qiu

Academic Year 2019-2020

Abstract

This thesis aims at investigating the interaction between thermal gradients and acoustic fields in microfluidic devices. In the research branch of acoustofluidics, which bridges together acoustics and fluid dynamics, inhomogeneity in the medium has gained great interest due to the novel physics behind and the potential in manipulating submicrometer particles. Concentration gradients of solute molecules have already been proven in previous studies to be effective means to obtain differences in fluid properties, such as density and compressibility, which induce acoustic body force and heavily affect the acoustic streaming. In this project another approach was taken, i.e. generating the inhomogeneity by thermal fields, to achieve a more stable and smooth variation in the thermophysical properties of the medium across the microchannel.

The thesis work developed mainly in two subsequent phases. Firstly, a set-up which is able to generate and maintain a temperature gradient across a channel cross-section was designed, built, and then automated via software control. Secondly, this platform was tested with a glass-silicon-glass microfluidic chip, recording the fluid motion by tracking micrometric particles via *General Defocusing Particle Tracking* (GDPT) technique. This experiment was done for three conditions: only with thermal field, only with acoustic field and with the two combined.

The results validate the effectiveness of the platform in generating and maintaining the thermal field and have a good agreement with literature, although the acoustic field appeared undesirable due to some channel geometry flaws. The novelty of the project, i.e. the thermal-acoustic interaction, revealed itself to be quite complex. As predicted, high velocity fields were observed, associated with some unexpected flow behaviours, particularly along the length of the channel. Further measurements using a device with ideal channel geometry, together with a closer collaboration with the theoreticians who are able to explain the underlying physics, are needed to reveal the full picture of this novel phenomenon.

Preface

The hereby thesis work is submitted to complete the Master's Double Degree T.I.M.E. program in Biomedical Engineering at Politecnico di Milano (PoliMi) and Lunds Universitet (LU). The project presented had been developed and performed during the whole 2019/2020 academic year at the Biomedical Engineering Department (BME) at Lunds Tekniska Högskola (LTH) in Lund, Sweden, and it corresponds to 18 ECTS credits at PoliMi and 30 ECTS credits at LTH.

I would love to acknowledge who had made this work possible, helping and supporting me during its realisation both in and outside the University.
First of all, I want to thank my supervisor, Per Augustsson. It is only because of him that I have taken this journey in the acoustofluidics and found myself totally amused by it. I am also extremely grateful to Wei Qiu, my co-supervisor, for being always there for me and for all the interesting discussion and ideas about possible (and impossible) experiments. A great acknowledgement goes to Luca Spigarelli as well, for trying explaining me the theory behind acoustofluidics in our own language, failing, and then switching back to English. Of course, thanks also to the rest of the Acoustophoresis group and the whole BME department in Lund, for being so welcoming and making me feel like home. In particular, I want to express my gratitude to Axel Tojo for teaching me all the secrets about milling and being so patient with me. Furthermore, I want to thank Jonas Helboe Jørgensen from DTU, for helping with his model and for the digital discussions we had trying to find some sense in all the data. In addiction, I would like to thank my supervisor at PoliMi, Marco Rasponi, and my double degree coordinator, Alberto Redaelli, for their support from distance, even in these strange times.

Last but not least, I want to thank all the people outside or around University that have accompanied me in this first voyage, both in Lund and in Italy. I cannot mention everyone, but each of you knows how important you are.
And of course, the biggest thanks goes to my family, on which I can always rely, no matter how many kilometers apart we are.
Let's hope that this was just the beginning.
Thank you, grazie, tack and gracias.

Enrico

Contents

List of Figures

List of Tables

List of Symbols

Symbol	Description	Unit
A	Area of a surface	m^2
a	Generic particle radius	m
C_p	Heat capacity	$J\ K^{-1}$
c	Speed of sound	$m\ s^{-1}$
c_p	Specific heat capacity	$J\ K^{-1}\ kg^{-1}$
D_i	Diffusion constant for the species i	$m^2\ s^{-1}$
$D_t\square$	Material derivative of $\square$	
$\mathbf{E}$	Electric field	$N\ c^{-1}$
E	Energy	J
E_{ac}	Acoustic energy	J
E^{adv}	Advective energy	J
E^{cond}	Conductive energy	J
E^k	Kinetic energy	J
E^P	Potential energy	J
E^{visc}	Viscous energy	J
$\mathbf{f}$	Force density	$N\ m^{-3}$
$\mathbf{f_{ac}}$	Acoustic body force	$N\ m^{-3}$
$\mathbf{g}$	Gravity acceleration	$m\ s^{-2}$
h	Relative condensation	
$\mathbf{J}$	Mass density current	$kg\ m^{-2}\ s^{-1}$
j	Imaginary unit	
K	Bulk modulus	Pa
k_B	Boltzmann constant	$J\ K^{-1}$
k_i	Wave number in the direction i	m^{-1}
k_{th}	Thermal conductivity	$W\ m^{-1}\ K^{-1}$
L	Characteristic length of a system	m
m	Mass	kg
p	Pressure	Pa
Q	Heat	J
q	Heat flux	$J\ m^{-2}$

Symbol	Description	Unit
R_a	Amplitude reflection coefficient	
R_I	Intensity reflection coefficient	
$\mathbf{r}$	Cartesian position vector	
S	Entropy	$J\ K^{-1}$
s	Specific entropy	$J\ K^{-1}\ kg^{-1}$
T	Oscillation period	s
T	Temperature	°C, K
T_I	Intensity transmission coefficient	
t	Time	s
u	Velocity along x	$m\ s^{-1}$
V	Volume	m^3
$\mathbf{v}$	Velocity vector	$m\ s^{-1}$
v	Velocity along y	$m\ s^{-1}$
v_i	Generic velocity magnitude along direction i	$m\ s^{-1}$
W	Channel width	m
w	Velocity along z	$m\ s^{-1}$
Z	Acoustic impedance	$Pa\ s\ m^{-1}$
α	Thermal diffusivity	$m^2\ s^{-1}$
$\boldsymbol{\delta}$	Unit tensor	
ζ	Bulk viscosity	$Pa\ s$
κ	Compressibility	Pa^{-1}
η	Dynamic viscosity of a fluid	$Pa\ s$
λ	Wavelength	m
ν	Kinematic viscosity	$m^2\ s^{-1}$
$\mathbf{\Pi}$	Momentum-flux-density tensor	$N\ m^{-2}$
ρ_e	Electric charge density	$C\ m^{-3}$
$\boldsymbol{\sigma'}$	Stress tensor	Pa
$\boldsymbol{\tau}$	Shear stress tensor	Pa
Φ	Acoustic contrast factor	
ϕ	Velocity potential	$m^2\ s^{-1}$
ω	Angular frequency	Hz
$\square$	Generic mathematical object or function	
$\partial_{\square}$	Partial derivative with respect to $\square$	
$\square^T$	$\square$ transposed	
$\nabla\square$	Gradient of $\square$	
$\nabla\cdot\square$	Divergence of $\square$	
$\nabla^2\square$	Laplcian of $\square$	
$\lvert\square\rvert$	Absolute value of $\square$	
$\langle\square\rangle$	Time average of $\square$	

Chapter 1

Introduction

1.1 Microfluidics and Lab-on-a-Chip systems

Thanks to technological development in the last few decades, performing experiments at a very small scale has become much easier and consequently the comprehension of phenomena at the micro-scale (and their applicability) has greatly improved. One could say that microfluidics has its origins in the 1960s, when microfabrication methods made possible to create and tune microstructures. This technique was first used in integrated circuit fabrication, thus allowing the electronics miniaturization race that is still going on to these days. The first application involving fluids appeared in 1965 and it was the ink-jet printing [1], that exploit the instability of a falling continuous flow of liquid to break it down to discrete droplets. This flow was forced through a vibrating micrometric nozzle and then the method was further developed to arrays of nozzles in 1977 [2], making possible to commercialize the technology in the following decade. It was around those years that the true potentiality of microfluidics in analytic field started to unfold, with a 1979 research in Stanford which explains how to fabricate a functional microscale gas chromatography system [3]. However, it was only in the 1990s that started being widely used not only in chemistry, but in many other fields, such as biotechnology, with the concept of micro total analysis systems (µTAS) [4]. The application of this technology to biology and medicine opens up the possibility to conduct complete physical-chemical analysis in so-called *microfluidic chips*: sub-millimeter channels embedded in an unique structure by various techniques, for example silicon etching (from which the name that resembles the more known *electronic* chips). To have an idea of the dimensions involved in such systems, one could have a look to Fig. 1.1, in which the scales that are usually dealt with in microfluidics are compared with more familiar objects.

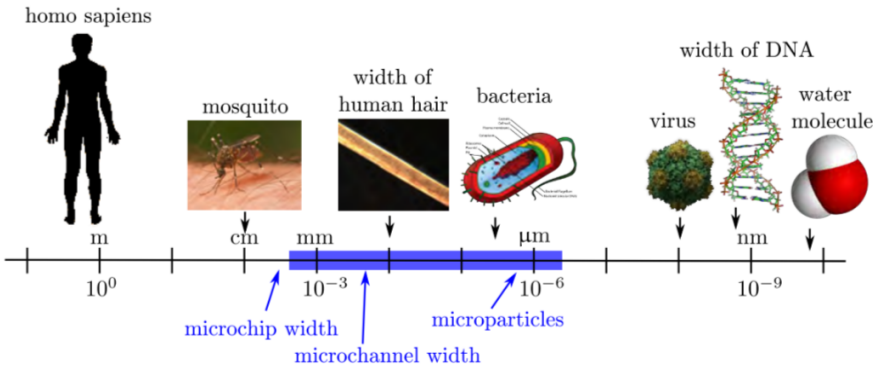

Figure 1.1: A logarithmic scale showing the dimensions of different objets. In blue it is highlighted the metric region usually involved in microfluidic systems. Figure courtesy of Rune Barnkob, from [64].

The possibility to perform multiple various operations in sequence in a controlled environment created the idea of Lab-on-a-Chip systems (LoC systems): more or less complex circuits in which different fluids, gases or liquids, interact with each other. The name wants to resonate the fact that the activities conducted in a whole analysis laboratory could in principle be scaled and processed on a suitable chip, thus tremendously improving in efficiency, reliability and reproducibility.
The expectations on the new-born field of microfluidic were enormous and they haven't of course been met yet. This is due to the fact that the smaller the scale L, the more different the fundamental physic is from the macroscopic classically studied fluid dynamics, with effects that are commonly negligible becoming dominant. This concept can be express by the surface-to-volume ratio:

$$\frac{\text{surface}}{\text{volume}} \sim \frac{L^2}{L^3} = \frac{1}{L}$$

This relation expresses the fact that the smaller the scale L becomes, the more predominant surface effects, such as viscosity, surface tension and adhesion, will be against volume ones (like gravity, momentum and kinetic energy). This allows to have high controlled and predictable flows (usually in microfluidic devices the flow is laminar, concept that will be deepened in section 2.6), for which the mathematical modelling results way less computational power-demanding. Besides modelization, the advantages of using microfluidics are numerous, but mainly the small volumes involved grant little reagents and samples consumption: this, alongside the fast time-scale required to perform experiments in such a small scale, implies great saving in both time and money. The highly controlled environments in which the operations take place and the chips small dimensions allow the scalability and parallelisation of a lot processes. These concepts alongside a great level of automation (thanks to the sensors and controls that are usually implied in microfluidic devices) are making the field exiting the research environment to be employed in the real industry (from product quality check, to diagnostics).

1.1.1 Fabrication processes

The gold standard in microfluidic chip fabrication was silicon etching. As in circuit board, the microstructures are usually obtained by photolithography: coating a silicon wafer with a polymer resist that can be then degraded or cured (depending if it is a negative or positive tone) by UV-exposure through a mask with the desired design, as shown in Fig. 1.2.

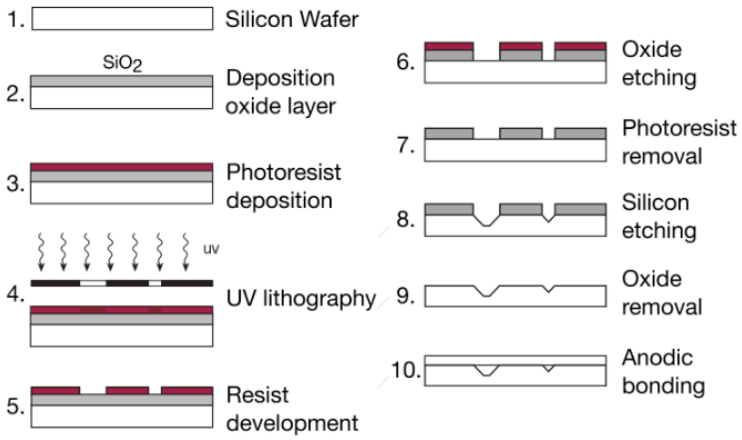

Figure 1.2: Silicon etching process via positive photoresisty photolithography. The process starts with a silicon buffer that then undergoes several steps before being etched, cleaned and anodically bonded to glass to create the microchannels. Reproduced from [5] for the courtesy of Giulia Core and the original author, Andreas Lenshof [6].

Then the silicon is chemically etched [7], process in which the atomic disposition (i.e. the crystalline planes in the solid) is crucial [8]. Different etching agents on different materials have isotropic or anisotropic etching, meaning that the material will be engraved differently in different directions. This can lead to various wall geometries in the microfluidic device, letting the researchers to be creative in designing solutions for their experiments. The etched silicon buffer is then anodcally bonded to glass, in order to actually create the channels and at the same time to allow visualisation, as shown in the last passage (number 10) in Fig. 1.2.

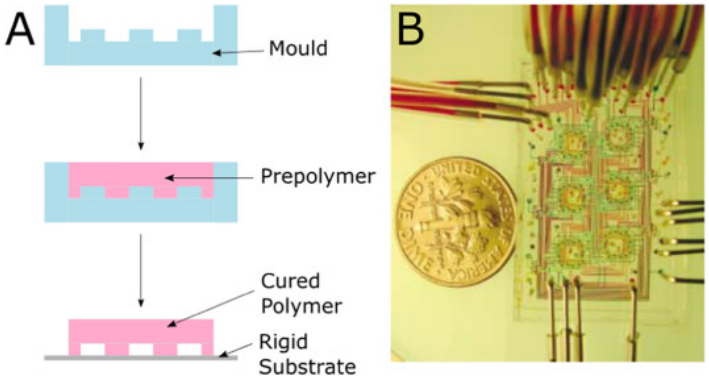

Figure 1.3: A: Schematic representation of how the moulding process for building polymeric chips works. Reproduced from [10] B: A replica-mould microfluidic device compared with a coin to give an idea of the small channel dimensions achievable. Reproduced from [9]. Reprinted with permission from AAAS.

Another interesting method consists of replica moulding [9]: this implies pouring pre-polymer against a mould (that has been usually produced by silicon etching) and then cure it, like in Fig. 1.3. The downside of this technique is that it is not an automated process, thus making industrial applicability impossible [10]. To counter this, micro-injection moulding has been developed. The fab-

rication method involves the injection of molted polymer into a closed mould, allowing the production of many uniform parts; the macro-scale version of this approach has been extensively used after WWII to manufacture goods in large scale. There are definitely some issues for applying injection moulding to micro-fabrication (like non uniformity, bubbles and thermal stresses during the cooling process), but there are successful examples in using this technique to fabricate working microfluidic devices [11].

Lately rapid prototyping (RP) has emerged as a possible solution as cheap and customized mean of fabrication. Classic RP methods include fuse deposition modelling (FDM), in which little quantity of a thermoplastic polymer is extruded by a heated nozzle along a pre-established pattern. Once one layer is completed, the printer shift to the next one, which is deposited on top of the previous one, thus building the object in 3D. Even if the nozzle dimensions have greatly decreased during the past two decades, the surface resolution and smoothness reached by FDM is not good enough [10]. This makes almost impossible to perform fluid dynamic experiments in such built channels, but they are still useful for reaction ones as in [12] and [13]. An approach similar to RP but much more precise is two-photon polymerisation lithography (2PPL): this involves a photopolymerisable pre-polymer bath in which an infrared laser is focused in the 3D space. Only where the laser beam is on focus the two-photon absorption occurs, thus polymerising the material with high resolution (as low as 120 nm [14]).

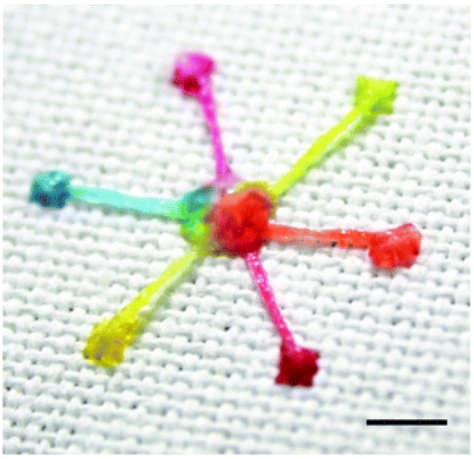

Figure 1.4: Example of a mixing thread-device, in which threads that are surface-treated allow to create the shown pattern (scale bar: 5 mm). Reproduced with permission from [17].

Interestingly, analytical microfluidic devices can also be built with really cheap materials and they can be designed in such a fashion that they work without the need of external forces. This is the concept behind paper [15] and thread [16] microfluidics, which exploit capillarity to drag fluid into the material matrix, thus making it react with substrates embedded on the paper or threads or carried by other capillary pathways. In these techniques, surface treatments (mainly related to the hydrophobicity or hydrophylicity of the material) are fundamental in designing the device, as in Fig. 1.4. Surprisingly, these materials allow for more complex structures than more canonical and precise fabrication methods, being that the 3D structure of the material itself can be exploited to guide fluid along different planes [18].

1.1.2 Applications

Microfluidic applications are various and they span across many different fields. While there are already consumer products relying on this technology (such as disposable pregnancy test and urine glucose test [19]), most of the applications are still in research or have made it just to small sectors of medicine (like insulin pumps [20]). Interesting new applications that could soon reach the market span from wearable electronics, in which microfluidics can play a key role (thanks to the versatility it has in collecting, amplifying and even power supplying [21]), to smart bandages, able to monitor real time the state of a wound [22], as shown in Fig. 1.5.

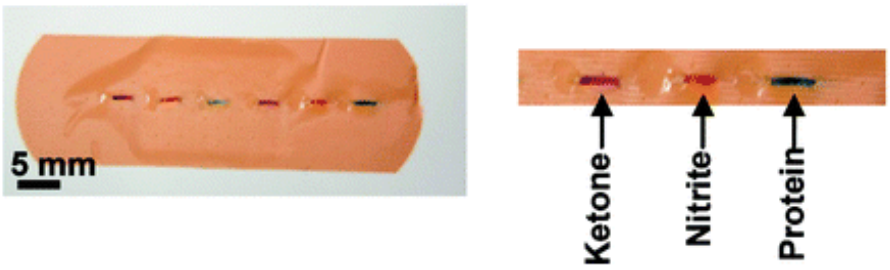

Figure 1.5: Woven-thread bioassays used to monitor the state of a wound in a common bandage. Adapted with permission from [22]. Copyright 2010 American Chemical Society.

Microfluidics played a key role in the Human Genome Project, which started in 1990 and it involved researcher for more than 15 years for mapping the whole human genome: the sequencing techniques available at the time had to greatly improve if they wanted to make it. So capillary electrophoresis was developed [23], reaching more than twice better resolution in one third of the time compared with classical slab gel electrophoresis. Subsequent steps were taken in order to magnify the genetic signal, meaning performing polymerase chain reaction (PCR) in a more efficient way: this led to the first PCR thermocycler chip [24], idea that with the years has greatly improved in throughput and automation [25].

Even more interesting (and recent) applications are the so-called *organs-on-a-chip*, in which a complex structure with different tissues is grown thanks to microfluidics techniques. Thanks to the versatility of the various microfluidic platforms, researchers could implement not only automated medium exchange in such cell culture, but also mechanical [26], chemical [27] and even electrical [28] stimulation to the cell populations. This approach aims to substitute the canonical cell culture methodology, which is limited to 2D structure or to organoids (i.e. different tissues growing together but without the physiological spatial arrangement): the ultimate goal will be to have different chips simulating different organs and the possibility to connect them. This would greatly enhance the complexity of the in-vitro experiments, making them much more resembling an actual functioning organism and thus allowing to test drugs much more efficiently, safely and way more inexpensively. The progress in this field is forecast to keep going at an incredible pace till the dream of a *human-on-a-chip* will be reached (as depicted in Fig. 1.6).

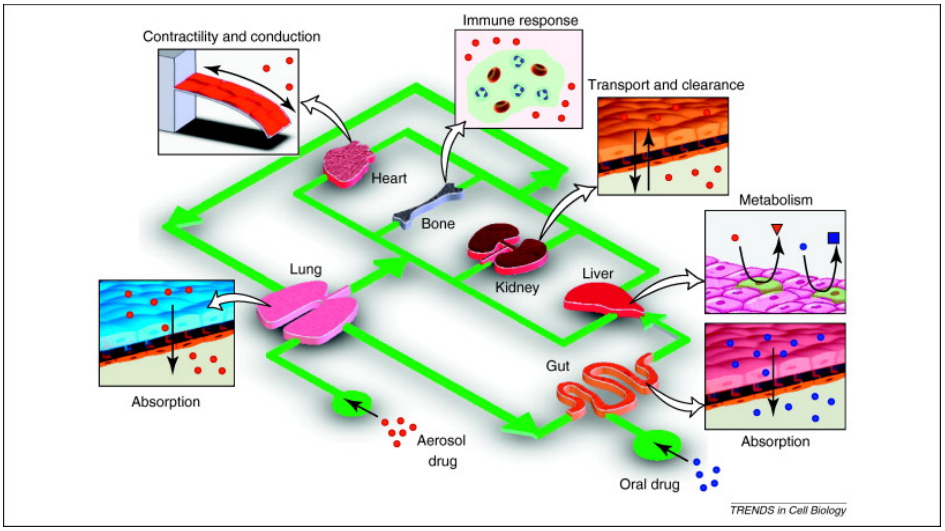

Figure 1.6: Scheme representing the *human-on-a-chip* concept. Every organ with its own different tissues is reproduced on a microfluidic chip and then, via suitable connections that resemble the physiological ones, multi-organ interaction for drugs/treatments can be studied. Reproduced with permission from [29].

Another broad field in which microfluidics has been widely used is cell or particles assessments through different techniques, some biomimetics (i.e. taking inspiration from biological processes), like fluid margination [30], and some exploiting complex artificial structures, such as deterministic lateral displacement (DLD) [31], in which arrays of micro-obstacles in the fluid path are used to separate suspended particles according to their dimension. Other examples in handling suspensions are micro-filters [32] or dielectrophoresis [33]. In the next section, the particle manipulation technique on which this thesis work focuses on, called acoustophoresis, will be introduced.

1.2 Acoustofluidics

The term *acoustofluidics* refers to the interaction between ultrasonic waves and suspensions. The ultrasound-generating element is usually a piezo-electric transducer made of a ceramic material that responds to oscillating currents with corresponding oscillating mechanical deformations. It can thus transmit sound waves inside the microchip and this is the base concept for bulk acoustic waves (BAW) devices. This has been shown to affect the streaming of the fluid and the behaviour of particles inside acoustic resonator [34].

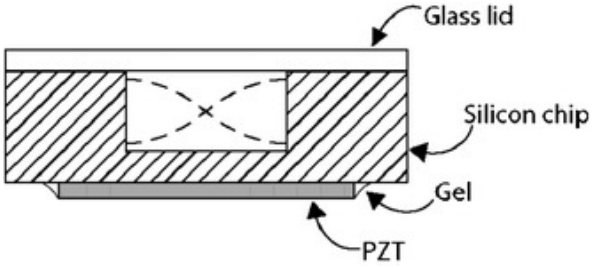

Figure 1.7: Basic design of a separation chip for continuous flow, consisting in a silicon-etched channel bond with a glass lid. The lead zirconate titonate (PZT) transducer generates an acoustic standing wave (the oscillating pressure field is represented by the dashed line) that allows gentle manipulation of particles. This approach has been called the *Lund method*. Reproduced with permission from [34].

One fundamental property of the forces generated by such an actuation is the low mechanical stress induced on the particles in suspensions: this opens up the possibility of manipulating delicate objects, such as cells and other suspended materials in biological samples [35].
The term *acoustophoresis* refers to the control of suspensions via sound waves and it derives from the Greek words *acousto* (sound) and *phoresis* (migration). The parameters on which this separation technique heavily depends are the size of the suspended particles and their relative density and compressibility compared with the surrounding medium. The size matters because the acoustic radiation force scales with the volume (i.e. the bigger the particle, the larger the force), while relative density and compressibility are important in determining the direction of such a force (via the so-called *contrast factor*).

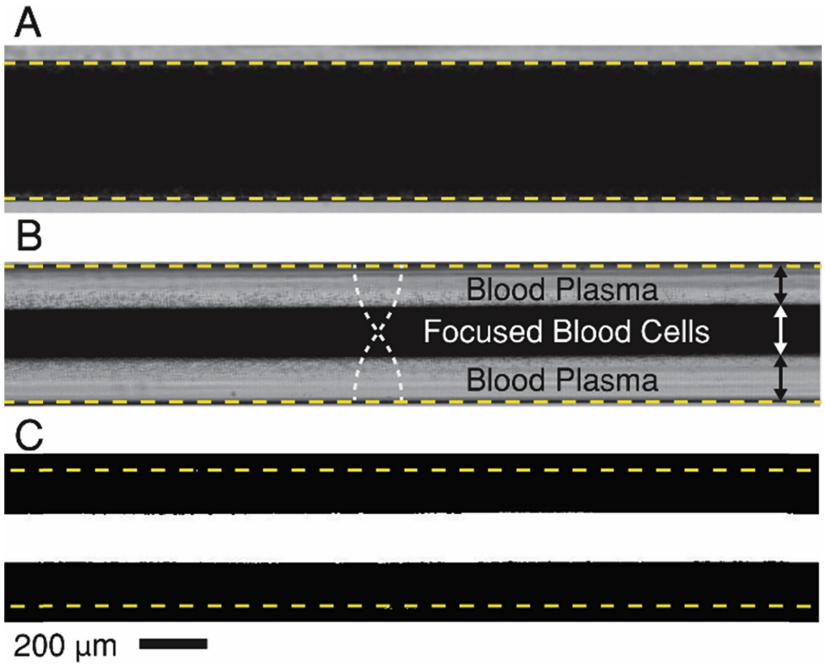

Figure 1.8: Whole blood in a microfluidic channel when (A) no sound field is present, (B) the sound field is actuated and thus the cells are then focused to the center, leaving the plasma at the side. (C) By introducing a simple threshold it is then possible to measure the hematocrit of the sample. Reproduced with permission from [36].

Taking as an example whole blood flowing inside an acoustic resonator [36], the cells (more dense

and less compressible than the surrounding fluid) have positive contrast factor and are thus focused at the center, while the plasma keeps flowing at the side (Fig. 1.8). Another example might be raw milk analysis via acoustophoresis [37], in which lipids (less dense and more compressible than the surrounding medium) are pushed to the acoustic antinodes (negative contrast factor), while the cells are once again focused at the center, as shown in Fig. 1.9.

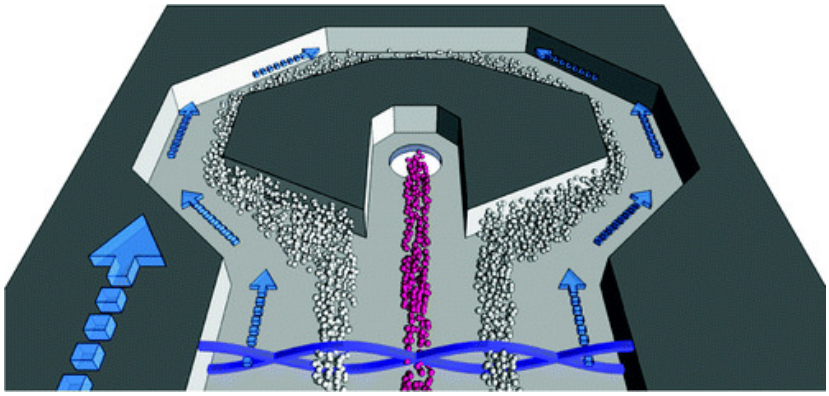

Figure 1.9: Three-nodal acoustophoresis is useful to separate cells from lipids in raw milk. The blue arrows indicate the flow directions. The cells go to the pressure node, while the lipids to the pressure antinodes: with the right flow tuning at the inlet, lipid depletion above 90 % can be achieved. Reproduced with permission from [37]. Copyright 2009 American Chemical Society.

The manipulation of suspended particles in fluids thanks to their acoustic properties has been proven useful in different biomedical applications, such as cancer cell enrichment [38] or separation of cell populations [39]. This latter technique exploits the fact that different cells have different acoustic properties and thus it is possible to differentiate them in an acoustic resonator with a chemical gradient (Fig. 1.10). This new technique is really powerful due to the fact that it allows cell sorting without using harmful or laborious labelling techniques, which could change the cell properties or not target the whole population. Of course even this technique, called *iso-acoustic focusing*, has indeed limitations: for example the different populations do not have clear intervals of density, but they have usually gaussian distributions that slightly overlay, making the separation between cell-types not optimal.

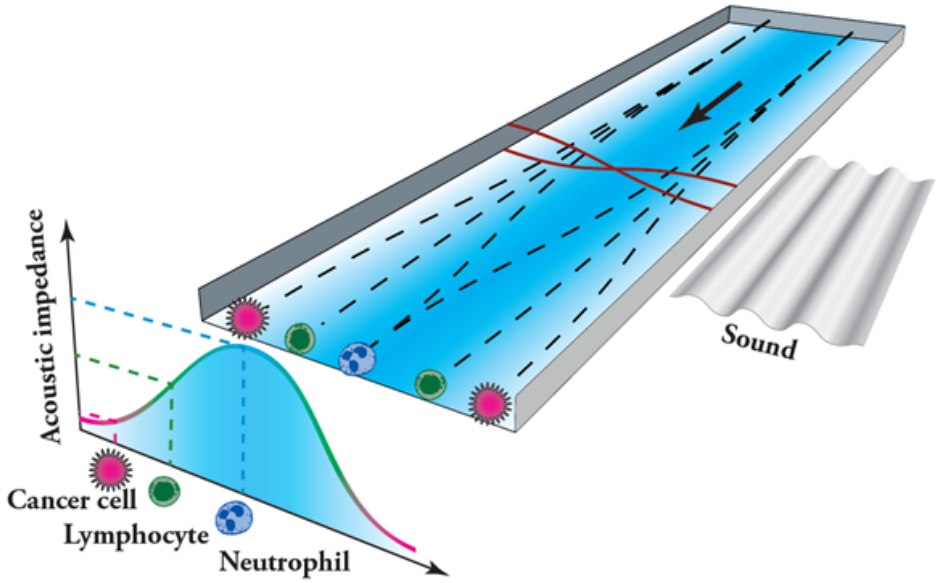

Figure 1.10: Schematic representation of iso-acoustic focusing: the cells, undergoing the sound field, will be subjected to a force till they reach a point in which there is no difference in acoustic impedance between them and the surrounding medium. This makes possible to differentiate among different cell populations only thanks to their intrinsic physical properties and without labeling. Figure courtesy of Per Augustsson.

However, standing waves generate not only the acoustic radiation force, but also acoustic streaming. This latter is the reason why this powerful tool has a size limitation, meaning that too small particles cannot be focused due to the drag force by the acoustic streaming. Recent development in theory and corresponding experimental observations have however proven that this limitation can be overcome by suppressing the acoustic streaming either by geometry tuning [40] or by introducing an inhomogeneity in the material properties of the medium within the channel [41].

The link between fluid inhomogeneity and acoustic has become clearer and clearer in the past few years, thanks to several studies and researchers putting a lot of effort into it, among which some works on fluid relocation [42] are fundamental for this thesis. As in experiments and explained by modeling, the acoustic field generates an acoustic body force able to stabilize or relocate fluids with different density inside a microchannel, as shown in Fig. 1.11.

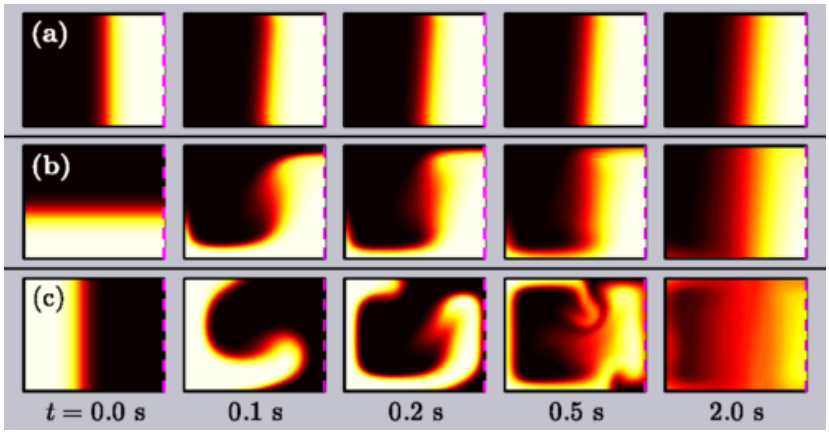

Figure 1.11: Halfchannel (mid-line is dashed in magenta) with two different miscible fluids with high (white) and low (black) density in three different situations. (a) the denser fluid is in the center at the initial time and so it remains due to the stabilizing effect of the body fore. (b) the denser fluid starts at the bottom of the channel, but, once the sound field is turned on, it relocates at the center, meaning that the acoustic body force can overcome gravity. (c) opposite situation as (a), with the denser fluid starting on the side but then relocating at the center once the acoustic field is on. It is worth noting the enhanced diffusion due to the fluid motion. Reproduced with permission from [42].

1.3 Thermal control in microfluidic devices

Managing the temperature inside a microfluidic device is challenging. There are several factor to consider, that can be coarsely divided in two main areas: generating the temperature field [43] and mapping the temperature [44].

There are several useful techniques to generate thermal fields in microfluidic systems. One commonly employed is external heating. One of the easiest techniques is using hot or cold fluids flowing parallel to the analytical channels. Doing so, the temperature in these latter ones will be influenced by the heat reservoir at their side. This method has for example been used to generate linear gradients across an array of parallel microchannels [45], as shown in Fig. 1.12.

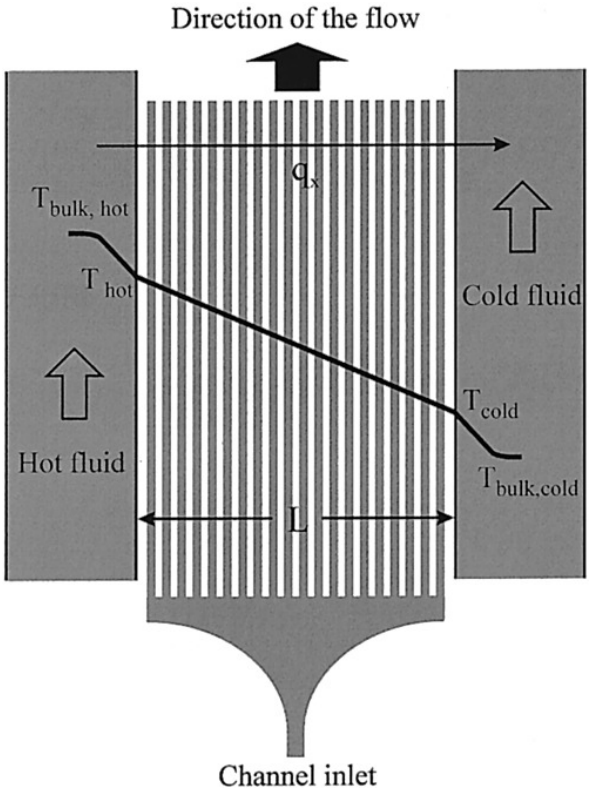

Figure 1.12: Two fluids (one hot to the left and one cold to the right) acting as thermal reservoir and thus making possible to have heat transfer from the left to the right, so generating a thermal gradient in the microchannel array. Reproduced with permission from [45]. Copyright 2002 American Chemical Society.

One of the drawbacks of this technique is the T stability, considering that while flowing in the device there will be a temperature change in the hot/cold fluids, even if small. Another approach that has been extensively used in literature is attaching to the device (or to its holder) thermo-electric elements, such as resistors or peltier elements [46]. Doing so it is possible to conduct heat in and out the microchannels, in presence of good thermal coupling of course. It was also possible for some researchers to integrate micro-peltier of size 0.6 x 0.6 x 1 mm^3, thus enabling measuring and control of temperature in super localised regions and thereby heating/cooling fluids in the nanoliter scale [47]. This last approach bridges between external heating and integrated heating techniques. These latter ones differ from the previous ones because the temperature control system is embedded within the microfluidic device. There are indeed several ways to build such a system. Chemical reactions in channels parallel to the analytical one (Fig. 1.13) is one example [48]: endothermic reactions (such as evaporation) or exothermic ones (such as acid dissolution) are used to control the temperature.

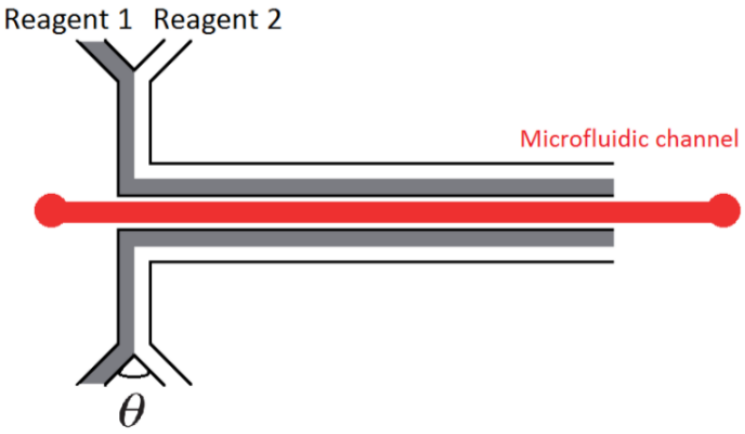

Figure 1.13: Schematic representation of how the chemical mean of temperature control works: on the side of the analytical channel, two reagents are mixed, causing either an endo- or an exo-thermal reaction. The mixing angle θ is an important parameter especially for cooling [49]. Reproduced from [43].

It has been proven that managing the flow rates of the reagents and the geometry of the channels in which the reactions happen (especially for cooling) can provide precise temperature control [49]. However, the most common integrated technique for managing the temperature is Joule heating, which relies on the dissipated power in a resistor (as function of the applied electric potential) [50]. Thanks to platinum (Pt) or gold (Au) wires embedded in the microfluidic device, it is possible to control the temperature in their proximity by making an electric current flow through. It is even possible to built arrays of such micro-heaters to localize heating and making it as uniform as possible [51], as shown in Fig. 1.14. One major downside of this technique is that the temperature cannot be controlled for low values, but just in a range that is higher than the room T.

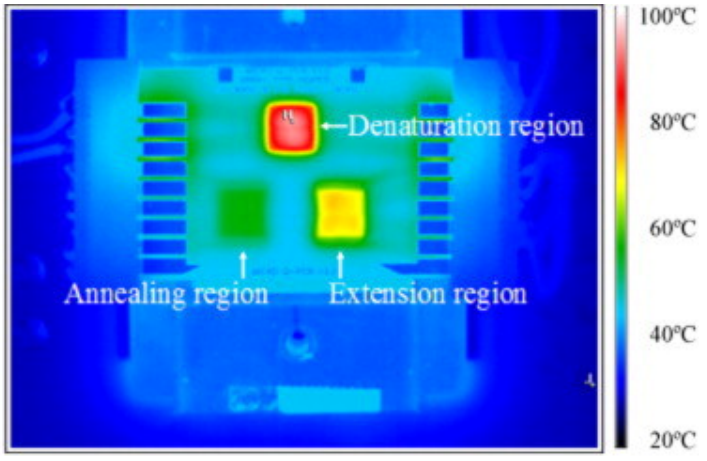

Figure 1.14: Micro-heaters made up by metal arrays to localize as much as possible the heat generation. The image shows the three different chambers to perform PCR at the three different T required, plus the heat sinks (dark blue) on the side. Reproduced with permission from [51].

Electromagnetic waves can also be used to perform heating of the liquid. These approaches differ from the ones presented above because they do not need contact to deliver energy. Microwaves (in the

range from 3 to 20 GHz) can be used to make liquids like water heat up by several degrees. Building miniaturized microwave heating elements and integrating them in microfluidic devices allow to precisely control temperature in localized regions (used for example, for PCR [52]). Another approach is the use of lasers: the high spatial resolution offered (around 1 µm) allows for precise temperature control, allowing heating of really small volumes and thus low reagents consumption. Applications can cover a wide and variegated range, like homogeneus temperature fields for real-time PCR [53] and thermal gradients for droplet control via thermocapillary effects [54]. Also for these electromagnetic techniques one of the major drawback is the lack of control in cooling the system, leaving it at just the thermal dissipation between the microfluidic device and the surrounding environment.

Once heat has been added to (or removed from) a system, its not trivial to quantify the temperature in such configuration, especially when considering microfluidic devices in which the small dimensions make direct probing very difficult. Of course modelling the system can help to have an idea of the temperature distribution, but the numerical models have the limitation of being idealized systems (for example complex geometries or imperfect boundaries conditions). Thus, there are several methods being applied to measure the temperature and it is possible to group them in three categories: invasive, semi-invasive and non-invasive.
Invasive techniques consist in temperature probes put in direct contact with the medium to be analysed: commonly used probes are thermo-electrical materials that change their resistivity with T, such as nickel (Ni) [55] or platinum (Pt) [56]. These are not so widely used due to difficulties in fabrication processes (the wires need to be deposited inside the channels/chambers) and because, despite being extremely small, they nonetheless affect the fluid dynamics inside the device.
Semi-invasive techniques measure the temperature at distance, but the medium to be analysed needs to be treated with an ad hoc probe. These ones generally work by collecting images of the device with the thermosensitive probe by optical microscopy and linking back its intensity with a pre-established calibration curve. Initially thermochromic liquid crystals were used in such applications [57], but their big dimensions (around 10 µm) prevent their applicability in many microfluidic devices. Nowadays kinetic fluorescent probes are more commonl used: they are molecules that can be exited by light at a certain wavelength, for then emitting photons at a higher wavelength. Examples of such molecules are Rhodamine B [58], acridine yellow [59] and many more [44].

Non-invasive techniques allow to measure the temperature from distance without the use of any pretreatment. One of these methods is infrared thermography, that quantifies the emitted light at low wavelength that every heated body emits [60]: an example of this visualisation can be seen in Fig. 1.14. A drawback is that solvents like water highly absorb wavelengths beyond 1 µm, but mainly this technique has the defect of the low spatial resolution due to diffraction. Another technique is backscatter interferometry [61], that measures variations in the optic path due to heating: it is a well known property of fluid to change refractive index in dependence on temperature.

1.4 Aim and outline of the thesis

This master thesis work has two main subsequent goals: designing an automated set-up to control the temperature inside a microfluidic device and then testing it on an acoustic resonator to see the interaction between the thermal and the acoustic field.
Once the goals were clear, the temperature control set-up was conceptualized and built in every part: from the design (done in Autodesk® Fusion 360™ software), to the actual milling of all the components. The automation of the system was done controlling the heating/cooling elements and imaging via the National Instrument software LabView [86], together with the open source image acquisition software Micro-Manager [87]. The interaction between the thermal and acoustic fields was documented by tracking particles inside the microchannel in the three possible scenarios: only thermal field, only acoustic field and the two combined. Doing so, the fluid motion could be characterized and the differences between the various situations highlighted. investigating the interactions between external temperature fields and standing sound waves inside an acoustic resonator. Hence, following the work as in [39], the inhomogeneity in this work will not be generated by a chemical mean, but exploiting the thermo-physical properties on the liquids at different temperatures.

This thesis consists of three main parts followed by an Appendix (with detailed materials and methods), plus of course the hereby introduction, that aims to give a context in which this scientific investigation has been conducted and the reasons why. The other three main parts are briefly summarized below.

Theoretical background (Chapter 2) This chapter aims to give a brief introduction to the basic laws of physics useful to describe the phenomena involved in the thesis work. The three different areas/disciplines to be comfortable with for designing and performing such an experiment are fluid dynamics, acoustics and heat transfer. Each of them has its own section that starts from the basic principles for then building up the complexity needed to describe the physics behind the observations and formulate solutions or improvements to the experiments.

Experimental section (Chapter 3) This chapter deals with the practical work done for this thesis. It starts with a short introduction to the used chip and holder, plus a brief explanation of the methods involved in the automated temperature control and the particle tracking. Subsequently, the results are introduced and discussed. They are divided into three main areas: temperature field characterization, acoustic actuation and thermal acoustic actuation. The first one starts showing a COMSOL model that is used to understand the expected thermal field with different set-ups; then it introduces the temperature calibration technique and the subsequent temperature gradient characterization, with the induced fluid motion. The second section deals with the acoustic actuation, in which the sound field has been characterized both with particles focusing and streaming to see how much it resembles the expected one. Lastly, the thermal acoustic actuation is investigated: this is the novelty of this project. The aim was to understand how a temperature gradient and an acoustic field interact when propagating along the same direction (across the channel width). This was done using particle tracking in a spot and an actuation frequency at which a "regular" acoustic streaming was observed, as proven in the previous section.

Conclusion and Outlook (Chapter 4) This chapter summarizes the project work findings, its limitations and suggests future developments and prospects for this thermal-acoustic interaction.

Chapter 2

Theoretical Background

2.1 Fluid dynamics

This section aims to introduce the basic concept of fluid dynamics and to briefly explain which physical phenomena are to be described in order to perform microfluidic experiments.
The main sources used to write this section are a fundamental physics text, *Transport Phenomena* by Bird, Stewart and Lightfoot [62], a text more related to the microfluidic topic, *Theoretical Microfluidics* by Henrik Bruus [63], and a PhD thesis by Rune Barknob, *Physics of microparticle acoustophoresis-Bridging theory and experiments*, from Bruus' group [64].

2.1.1 Viscosity and the continuum hypothesis

Fluids is the definition given to materials that are not solids, thus without a proper shape because they continuously deform under applied shear stress. Both gases and liquids fall in this category, but they are different in density determined by the intermolecular space (e.g. 0.3 nm for liquids and 3 nm for gases), due to atomic forces that bind matter together. Focusing on pure liquids, these forces confine the movements of each molecule, that are anyway always in motion as "vibration" in the space among its neighbours. These interactions are the primary cause of fluid viscosity, which may be defined as the tendency of the molecules to stick together under shear stresses. Seen in another perspective, given a fluid with a certain velocity, viscosity is its capability to transfer momentum from the moving molecules to the steady state ones, in the opposite direction of the velocity gradient.

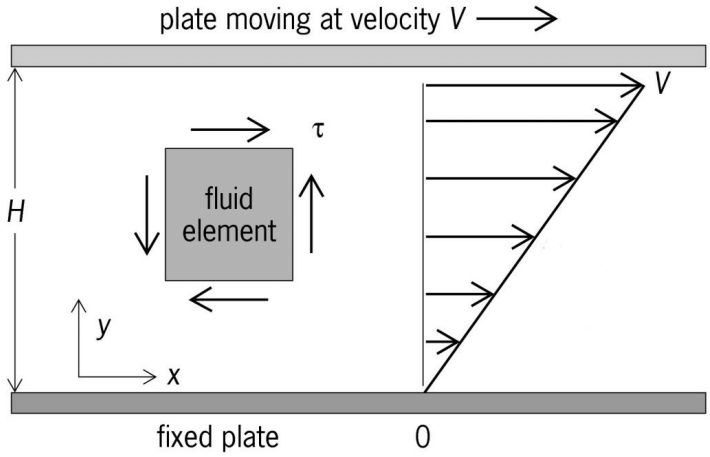

Figure 2.1: A fluid element with the shear stresses τ applied on its surface. The plate at distance $y = H$ from the fixed plate is moving at constant velocity $\mathbf{v}$. McGraw-Hill Concise Encyclopedia of Physics. Copyright 2002, from [65].

This observation was first mathematically formulated by Sir Isaac Newton, who noticed how in a liquid constantly moving with velocity $\mathbf{v}$ a force rises, proportional to the area A and its velocity, but inversely proportional to the distance H from the steady wall:

$$\mathbf{F} = \eta A \frac{\mathbf{v}}{H}$$

in which η is the dynamic viscosity, that quantify the "stickiness" of a fluid or better, its resistance to flow. Going to the differential formulation and considering not a force, but the *shear stress* (that is a force per unit area):

$$\boldsymbol{\tau} = -\eta \frac{\mathrm{d}\mathbf{v}}{\mathrm{d}y} \tag{2.1}$$

its generalisation in three dimensions is possible considering the tensor notation:

$$\boldsymbol{\tau} = -\eta(\nabla \mathbf{v} + (\nabla \mathbf{v})^T) + (\frac{2}{3}\eta - \zeta)(\nabla \cdot \mathbf{v})\boldsymbol{\delta} \tag{2.2}$$

Here there are the two coefficients characterizing the fluid: the dynamic viscosity η (relation between the shear stress and strain in one direction) and the dilatational (aka bulk) viscosity ζ, related to the fluid resistance to dilatation and compression.

While for gases the momentum transfer arises from molecule collisions, for liquids it depends on the intermolecular forces mentioned above and this explains their different viscosity dependence on T: for gases it usually increases with T (more collisions), while for fluids the higher kinetic energy of individual molecules makes the intermolecular forces less predominant, thus resulting in a decrease in viscosity with T. Furthermore, for liquids the viscosity may be dependent on the applied shear strain velocity, especially true if the molecular weight is high or if we are dealing with suspension instead of pure liquids: if the stress-strain proportionality is constant (i.e. constant viscosity), the fluid is defined as Newtonian, otherwise it is considered as non-Newtonian.

Considering molecules of mass m_i and velocity v_i in a volume ΔV large enough for the physical properties to be statistically invariant, in an Eulerian coordinate system, the density and the velocity

field of this volume can be defined as:

$$\rho(\mathbf{r}, t) \equiv \frac{1}{\Delta V} \sum_{i \in \Delta V} m_i \tag{2.3a}$$

$$\mathbf{v}(\mathbf{r}, t) \equiv \frac{1}{\rho(\mathbf{r}, t)\Delta V} \sum_{i \in \Delta V} m_i v_i \tag{2.3b}$$

In which the velocity has been defined through the concept of momentum. Another characteristic for the dimensions of ΔV is to be small enough to not be subjected to external forces: considering such a fluid particle as basic element, the whole fluid can be approached as a continuous structure made up of these constituents. This is the so-called continuum hypothesis and given that there is no defined size for the particle elements, it is natural that the mathematical description of the phenomena deals with definitions per unit volume. However, typical fluid particle dimensions are in the range of 10 nm, well in between the intermolecular distance and the system characteristic dimensions (ca 10 um).

2.1.2 Conservation equation

Assuming a compressible, thermoviscous, Newtonian fluid particle, one can mathematically describe the conservation equations of mass, energy and momentum balancing the quantities variation within the volume ΔV with the fluxes entering or exiting it.

Mass

It follows simply by the continuum definition, meaning that mass can vary only with mass flows in/out through the surface dV and it is possible to define a consequent mass density current $\mathbf{J}$.

$$M(\Delta V, t) = \int_{\Delta V} d\mathbf{r} \rho(\mathbf{r}, t) \tag{2.4}$$

$$\mathbf{J}(\mathbf{r}, t) = \rho(\mathbf{r}, t)\mathbf{v}(\mathbf{r}, t) \tag{2.5}$$

It can be derived that

$$\partial_t \rho = -\nabla \cdot (\rho \mathbf{v}) \tag{2.6}$$

This equation compare the rate of increase the fluid particle density (mass per unit volume) on the left side with the net rate of mass that is added to the particle volume due to convection (right side). To give a visualisation of this, let's imagine to observe from a bridge the fishes swimming underneath the observer position. In the volume of interest, the density of the animals will change over time due to their movement in the river: according to the different velocities at which the fishes will enter or exit the volume, there will be an increase or a decrease in density over time. In order to link back to Eq. 2.6, it's enough to consider instead of the single animals each fluid molecule and as volume of interest a fluid particle and thus the concept of density takes its more natural sense (as in Eq. 2.3a).

Energy

This balance looks at the energy accumulation in a fluid particle, disregarding any heat source or sinks in the sample volume.

$$\partial_t E = \partial_t E^{adv} + \partial_t E^P + \partial_t E^{visc} + \partial_t E^{cond} \tag{2.7}$$

Defining all the energies in term of entropy s, stresses $\boldsymbol{\sigma}'$, velocity $\mathbf{v}$ and temperature T, the balance becomes:

$$\rho T\Big[\partial_t s + (\mathbf{v}\cdot\nabla)s\Big] = \boldsymbol{\sigma}' : \nabla\mathbf{v} + \nabla\cdot(k_{th}\nabla T) \tag{2.8}$$

This equation would be useful in this thesis for the description of both the temperature filed in the acoutic perturbation theory and the thermal gradient built across the system, especially with the term E^{cond}.

Momentum

To get the third conservation equation, let us consider a fluid particle, its momentum density and the momentum fluxes that go in and out of the surface. It is the fluid equivalent of Newton's II law:

$$\rho\ D_t\mathbf{v} = \sum_j \mathbf{f}_j \tag{2.9}$$

in which D_t represents the material derivative, that shows how a physical property changes in a material element (in this case, a fluid particle) with a time and space dependent velocity field. To easily explain this type of derivation, let's go back to the fish observation example; this time, one can imagine an observer on a raft going with the current (velocity v_x, v_y and v_z) on a river, observing the fish concentration c underneath: reporting the change in the animals concentration, the observer has to count his own movement as well. At each instant, this change is given by:

$$\frac{Dc}{Dt} = D_t\ c = \frac{\partial c}{\partial t} + v_x\frac{\partial c}{\partial x} + v_y\frac{\partial c}{\partial y} + v_z\frac{\partial c}{\partial z}$$

or in compact form:

$$D_t\ c = \frac{\partial c}{\partial t} + (\mathbf{v}\cdot\nabla c)$$

From 2.9, it can be derived that:

$$(\partial_t\rho\mathbf{v} + (\rho\mathbf{v}\cdot\nabla)\mathbf{v}) = -\nabla p + \eta\nabla^2\mathbf{v} + (\frac{1}{3}\eta + \zeta)\nabla(\nabla\mathbf{v}) + \rho\mathbf{g} + \rho_e\mathbf{E} \tag{2.10}$$

In which the left side represents the rate of increasing momentum within the fluid particle (one term for the internal increase in time, the other for the addiction by convection), while on the right side there are losses due to pressure, viscous friction and body forces (gravity and external electric fields).

2.1.3 Fluid solutions

To give a possibility to solve the dynamic and kinematic fields of a fluid in different states, the conservation equations in the previous paragraph (Eq. 2.6, 2.8 and 2.10) have to be combined with

the particular material constitutive equations (that bind stresses and strains) and the thermodynamic relations defining density and entropy per mass unit as function of temperature T and pressure p.

$$\mathrm{d}\rho = (\partial_T \rho)_p \mathrm{d}T + (\partial_p \rho)_T \mathrm{d}p \tag{2.11}$$

$$\mathrm{d}s = (\partial_T s)_p \mathrm{d}T + (\partial_p s)_T \mathrm{d}p \tag{2.12}$$

In Eq. 2.11 the density change $\mathrm{d}\rho$ is defined as function of the derivative with respect of T at constant pressure and of the derivative with respect of p at constant temperature. Analogously, in Eq. 2.12 it is described the entropy change $\mathrm{d}s$.
For every medium in which an adiabatic compression takes place, small changes in pressure are related to small changes in density $p' = (\partial p/\partial \rho)_s \rho'$. It is therefore possible to define the isentropic compressibility κ, linking the compression of the fluid to changes in pressure, the bulk modulus K, that is the inverse of κ, and the isentropic speed of sound (c) as follows:

$$\kappa = -\frac{1}{V}\Big(\frac{\partial V}{\partial p}\Big)_s = \frac{1}{\rho_0}\Big(\frac{\partial \rho}{\partial p}\Big)_s \tag{2.13a}$$

$$K = \frac{1}{\kappa} = \Big(\frac{\partial p}{\partial V/V}\Big)_s \tag{2.13b}$$

$$c = \sqrt{\frac{1}{\rho_0 \kappa}} = \sqrt{\Big(\frac{\partial p}{\partial \rho}\Big)_s} \tag{2.13c}$$

For a Newtonian fluid Eq.2.2 may be used to determine the shear stresses, while the hydrostatic components can be found with equilibrium considerations. Of course, in order to find a solution for the system of differential equations, suitable initial and boundary conditions are needed.

2.1.4 Boundary

In order to solve the system of differential equations, one needs to find suitable boundary conditions, meaning knowing (or hypothesising) the velocity or stresses values at the boundaries of the system. One of the most common boundary conditions is the so called *no-slip* condition, which states that tangent velocity components are the same at every side of the interface. For a solid-liquid interface this equality is valid for the velocity normal component as well, so that the fluid velocity matches the solid surface one. This assumes the complete momentum relaxation between the solid molecules to be at rest and that the fluid molecules that collide with the wall. Whatever boundary conditions are applied, a usual assumption is that there is no material passing through the interface, meaning that no absorption, adsorption, dissolution, chemical reaction, evaporation and melting happens at the interface, if not stated otherwise.

2.1.5 Diffusion

Diffusion is the motion of particles (solute) in a liquid (solvent) from the regions of high to low concentration: it originates from the thermally induced random motion of particles. The i-th solute one-dimensional flow J_y along y at a steady state can be described by the *Fick's first law* of diffusion:

$$J_y = -D_i \frac{\mathrm{d}C_i}{\mathrm{d}y} \tag{2.14}$$

in which $D_i = (k_B T)/(6\pi\eta a)$ is Einstein's diffusion constant definition for the i-th solute and C_i is the steady concentration variation along y for the i-th species. Its generalisation in three dimensions is possible considering the vector form:

$$\mathbf{J} = -D_i \nabla C_i \tag{2.15}$$

In order to describe diffusion at a transition state, *Fick's second law* of diffusion can be used:

$$\partial_t C_i = D_i \nabla^2 C_i \tag{2.16}$$

The so-called diffusion length, that is the average distance covered by a particle in a time t, can be expressed as $L_{3D} = \sqrt{6 D_i t}$ when considering the movement in three dimensions and as $L_{1D} = \sqrt{2 D_i t}$ in one dimension. The dependence on the square root of time makes diffusion really effective over short distances, while a very slow process over long distances.

2.1.6 Laminar flow

As the adjective suggests, this type of flow has to be thought as different fluid lamina streaming one adjacent to the other, in an ordered way; it is juxtaposed to "turbulent", a more chaotic flow in which fluid rolls (called eddies) greatly enhance the mixing. One gets the latter one if the convective term in the momentum flux results predominant, while the former one is characterized by a dominance by viscous forces. In order to understand which flow regime a case study has, one can evaluate the Reynolds number, one of the dimensionless number of fluid dynamics that relates the ratio between inertial and viscous forces.

$$Re = \frac{\rho v L}{\eta} \tag{2.17}$$

if $Re < 1$ it means that the inertial forces are small compared with the viscous one and thus the flow is orderly. The more this number increases, the more the momentum is transferred by convection than by viscous dissipation, meaning that the flow would present more and more vortices (called *eddies*) that would make the flow more chaotic and thus making it harder to have proper mathematical field characterisations (Fig. 2.2). There is no clear cut between Re number for laminar or turbulent flow, but by convention if $Re > 4000$ the flow is considered to be fully turbulent [10].

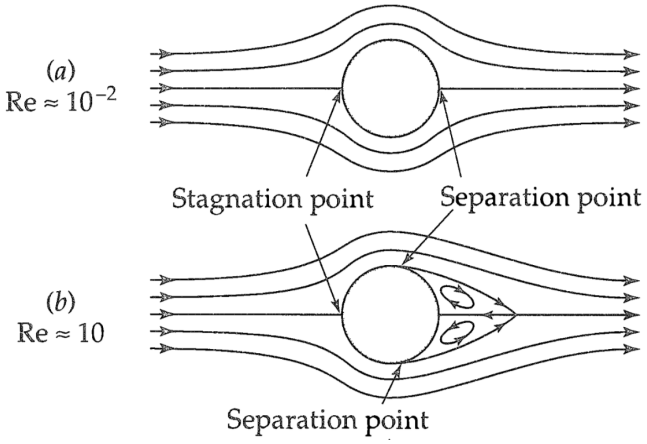

Figure 2.2: Scheme of the effects of flows with different Reynolds numbers on a steady sphere. As one can see, with very low Re (a) there is perfect continuity of the flow, but as soon as Re increases (b), some eddies start to form downstream of the sphere. Adapted with permission from [62].

To summarize, the change between viscosity-dominated motion to inertia-dominated one it is not sudden, but with increasing Re the inertia will have more and more influence and it is for really high Re that the flow is completely chaotic.
It is typical for microfluidic to have small characteristic lengths and little fluid velocity, meaning that the resulting Reynolds number is usually well below 1: this allows to have a good mathematical description and thus modelization of the transport phenomena within the system, making possible to forecast pure fluids or suspensions behaviour with good approximation.

2.1.7 Creeping flow and drag force

Consider the situation in Fig. 2.2, in which a static sphere of radius a surrounded by a fluid with density ρ_f in motion in one direction (as example z) with velocity v_∞, characterized by $Re \ll 1$. The submersed body would modify the fluid trajectory and this latter would in contrast exert some forces on the sphere. As discussed in paragraph 1.4, the velocity at the surface is null, being the sphere assumed static: the stress tensor can be obtained from the velocity distribution, computed together with the pressure field as explained in paragraph 2.1.3 (in this case the spherical coordinate approach is preferable and the reader who wants to deepen the topic may refer to [62]).
In order to obtain the force applied by the fluid to the sphere, one could integrate the z-components of the normal and tangent tensors over the sphere surface, exploiting the simple observation of symmetry around the z-axis that evens out the other components.
The fluid exerts a normal force per unit area which is the sum of the pressure and the radial component of the stress tensor, resulting in the force F_z^n.

$$F_z^n = \frac{4}{3}\pi a^3 \rho_f g + 2\pi\eta a v_\infty \tag{2.18}$$

The force has the first component representing the buoyant force (mass of moved fluid times gravity) and the second component gives the "from drag", proportional to the fluid approaching velocity v_∞ and related to the shape, thus to the resistance offered.
The tangent z-component of this force per unit area is just dependent on the stress tensor. Again,

this will be multiplied by the infinitesimal surface area and then integrate along the whole sphere, resulting in the force F_z^t.

$$F_z^t = 4\pi\eta a v_\infty \tag{2.19}$$

This force is also known as "friction drag", related to the dissipation on the body surface caused by the flow.

Hence the total force that the fluid exerts on the sphere is given by the sum of these two terms:

$$F_z^{tot} = \frac{4}{3}\pi a^3 \rho_f g + 6\pi\eta a v_\infty \tag{2.20}$$

The first term, as previously stated, is the buoyant force that is present even with the fluid at rest; on the other hand, the second term refers to the kinetic force resulting by the fluid motion, also known as *Stoke's law*. This law is useful just for Re up to 1, at which it already predicts a force about 10% too low ([62], 2.6).

2.2 Acoustics

In this section an introduction to acoustic is given, followed by the physical concepts needed to perform experiments in an acoustic resonator and the basics of acoustofluidics.
The main sources for this section are a basic physics book, *Fundamentals of Acoustics* by Kinsler and Frey [66], two PhD thesis, *Physics of microparticle acoustophoresis- Bridging theory and experiments* by Rune Barnkob [64] and *On microchannel acoustophoresis- Experimental considerations and life science applications* by Per Augustsson [67], and the Acoustofluidics tutorials on *Lab on a Chip* [68]. It is stated when more precise referencing is needed.

2.2.1 Acoustic wave equation and its solution

Sound can be thought as a pressure difference p that moves through matter: there is no net displacement of molecules or atoms, but each of them "vibrates" around its equilibrium position with a relative displacement $\mathbf{s}$, meaning that there is no mass transport, but just energy transfer. Depending on the nature of the medium in which it moves, this pressure wave can propagate in different ways; a transverse wave would arise if the displacement is perpendicular to the wave propagation, while in a longitudinal wave the displacement is parallel to the wave propagation. This thesis work focuses on fluids that, as explained in section 1.1, have no shear elasticity: hence fluids cannot transmit transverse waves, but just longitudinal ones.
Considering the continuity equation as in Eq. 2.6 and decomposing the instantaneous density $\rho = \rho_0(1+h)$ in a constant mean term ρ_0 and a relative condensation $h = -\mathrm{d}V/V$ due to the travelling acoustic wave, if one consider ρ_0 independent of time and with small variation in space, with the assumption of h being small compared to unity, it is possible to rewrite the continuity equation as:

$$\frac{\partial h}{\partial t} + \nabla \mathbf{v} = 0 \tag{2.21}$$

The motion induced by a moving acoustic wave does not introduce rotational motion of fluid particles [66], meaning that the velocity is an irrotational vector that can be represented as the gradient of a scalar potential $\phi = \phi(x, y, z, t)$, known as *velocity potential*, so that:

$$\frac{\partial \phi}{\partial x} = u; \qquad \frac{\partial \phi}{\partial y} = v; \qquad \frac{\partial \phi}{\partial z} = w$$

Hence, Eq. 2.21 can be rewritten as:

$$\frac{\partial h}{\partial t} + \nabla^2 \phi = 0 \tag{2.22}$$

To find a relationship between ϕ and h one can consider the forces acting on a fluid particle only subjected to an acoustic wave. The momentum balance as in Eq. 2.10 will result in a balance between the rate of momentum increase in time and the instantaneous pressure p' gradient:

$$\frac{\partial(\rho \mathbf{v})}{\partial t} = -\nabla p' \tag{2.23}$$

Introducing again $\rho = \rho_0(1+h)$ with the assumption $h \ll 1$ and considering each component independently, it is possible to obtain:

$$\frac{\partial p'}{\partial x} = -\rho_0 \frac{\partial u}{\partial t}$$
$$\frac{\partial p'}{\partial y} = -\rho_0 \frac{\partial v}{\partial t}$$
$$\frac{\partial p'}{\partial z} = -\rho_0 \frac{\partial w}{\partial t}$$

Multiplying the first equation by dx, the second by dy and the third by dz and then summing up the three, one gets:

$$\frac{\partial p'}{\partial x}dx + \frac{\partial p'}{\partial y}dy + \frac{\partial p'}{\partial z}dz = -\rho_0 \frac{\partial}{\partial t}\Big(u\ dx + v\ dy + w\ dz\Big) \tag{2.24}$$

Upon simplification and reintroducing the velocity potential ϕ, it becomes:

$$dp' = -\rho_0 \frac{\partial}{\partial t} d\phi \tag{2.25}$$

Integrating at any random time instant and considering the initial resting condition $p' = p_0$, it is possible to write the incremental pressure p:

$$p = p' - p_0 = -\rho_0 \frac{\partial \phi}{\partial t} \tag{2.26}$$

Recalling the bulk modulus K from Eq. 2.13b and noting that the volume strain corresponds to a negative condensation h

$$\frac{dV}{V} = -\frac{d\rho}{\rho_0} = -h$$

it is possible to write:

$$p = hK = \rho_0 c^2 h \tag{2.27}$$

In which the speed of sound definition $c^2 = K/\rho_0$ has been used (from Eq. 2.13c).
Combining the previous equation with Eq. 2.26, it is possible to express h as function of ϕ, thus, insrting it in Eq. 2.22, the so-called *acoustic wave equation* in its three dimensional form can be written:

$$\frac{\partial^2 \phi}{\partial t^2} = c^2 \nabla^2 \phi \tag{2.28}$$

Its solutions represent the propagation of a velocity potential ϕ with velocity of propagation c, from which all the other acoustic variables might be readily obtained by using relations such as:

$$p = -\rho_0 \frac{\partial \phi}{\partial t}, \quad h = \frac{p}{\rho_0 c^2}, \quad u = \frac{\partial \phi}{\partial x}, \quad v = \frac{\partial \phi}{\partial y}, \quad \text{etc.}$$

Considering a sound wave travelling in the y direction, with zero velocity component in x and z, Eq. 2.28 can be written in its 1D form:

$$\frac{\partial^2 \phi}{\partial t^2} = c^2 \frac{\partial^2 \phi}{\partial y^2} \tag{2.29}$$

The most important solution to this equation is made by harmonic waves, that in complex form can

be for example expressed as:

$$\phi = j(A\ e^{j(\omega t - ky)} + B\ e^{(\omega t + ky)}) = \phi_+ + \phi_- \tag{2.30}$$

In which ϕ_+ and ϕ_- represent two travelling waves with same frequency and speed, travelling respectively in the positive and negative direction. Hence, considering the different relations between the velocity potential and the other acoustic variables, the acoustic pressure difference p, y-velocity v and displacement s have the form:

$$p(y,t) = -j\omega\rho_0(\phi_+ + \phi_-) \tag{2.31a}$$

$$v(y,t) = -jk(\phi_+ - \phi_-) \tag{2.31b}$$

$$s(y,t) = \int v\ dt = -\frac{1}{c}(\phi_+ - \phi_-) \tag{2.31c}$$

It is worth noting that pressure p and velocity v are in phase when travelling in the positive direction, but shifted by π (i.e. opposite sign) when going in the negative direction. They are nonetheless $\pi/2$ phase-shifted with respect to displacement s.

2.2.2 Acoustic impedance

Analogously to electrical impedance, the resistance to the wave motion for a specific medium i can be generally defined as the ratio between the driving force (pressure) and the flow (local particle velocity v):

$$Z^i = \frac{p}{v} \tag{2.32}$$

Thus, considering the harmonic solutions for p and v in one direction as formulated above, the specific acoustic impedance becomes:

$$Z^i_+ = \frac{p_+}{v_+} = \rho_i c_i \tag{2.33a}$$

$$Z^i_- = \frac{p_-}{v_-} = -\rho_i c_i \tag{2.33b}$$

respectively for a wave travelling in the positive and negative direction. As an example, not taking in consideration the wave directions, below there are the compressibility and speed of sound values for two materials involved in this thesis work, such as water and pyrex glass, and their straightforward acoustic impedance.

$$\rho^{wa} = 997\ kg\ m^{-3} \quad c^{wa} = 1497\ m\ s^{-1} \implies Z^{wa} = 1.49\ MPa\ s\ m^{-1}$$

$$\rho^{gl} = 2230\ kg\ m^{-3} \quad c^{gl} = 5640\ m\ s^{-1} \implies Z^{gl} = 12.6\ MPa\ s\ m^{-1}$$

As one can easily see, the impedance of a rigid material like glass is much higher than the one for a fluid like water: this is because of the amount of energy needed to compress the single molecules of the bulk, which is indeed much higher the more ordered and compact a substance is.

2.2.3 Interface: reflection and transmission

Like any other wave, sound waves as well are affected when meeting the interface between two media with different acoustic impedance $Z^1 \neq Z^2$. Given an incident pressure wave $p_i = A_i e^{j(\omega t - k_1 y)}$, interacting with the interface one part will bounce back (*reflected*) $p_r = A_r e^{j(\omega t + k_1 y)}$ and another part will travel across (*transmitted*) $p_t = A_t e^{j(\omega t - k_2 y)}$. Two boundary conditions have to be satisfied at any point of the surface separating the two media: continuous acoustic particle motion across the interface to not cause medium disruption (i.e. the normal velocities are equal) and equal acoustic pressure on the two sides of the boundary. Formalizing the latter one for the interface set at $y = 0$: meaning

$$p_i + p_r = p_t; \qquad A_i e^{j\omega t} + A_r e^{j\omega t} = A_t e^{j\omega t}; \qquad A_i + A_r = A_t \tag{2.34}$$

Recalling the definition of acoustic impedance $Z_i = \rho_i c_i$, it is possible to write:

$$v_i = \frac{p_i}{\rho_1 c_1}, \quad v_r = -\frac{p_r}{\rho_1 c_1} \quad \text{and} \quad v_t = \frac{p_t}{\rho_2 c_2}$$

Expressing the first boundary condition regarding the equal velocities at the interface as $v_i + v_r = v_t$ and inserting the relationship between pressure and velocity (again evaluated for $y = 0$):

$$\frac{A_i e^{j\omega t}}{\rho_1 c_1} - \frac{A_r e^{j\omega t}}{\rho_1 c_1} = \frac{A_t e^{j\omega t}}{\rho_2 c_2}; \qquad \rho_2 c_2 (A_i - A_r) = \rho_1 c_1 A_t \tag{2.35}$$

Combining Eq. 2.35 with Eq. 2.34, one can eliminate A_t, leaving just the incident and reflected amplitudes A_i and A_r:

$$\rho_2 c_2 (A_i - A_r) = \rho_1 c_1 (A_i + A_r); \qquad A_i(\rho_2 c_r - \rho_1 c_1) = A_r(\rho_2 c_2 + \rho_1 c_1) \tag{2.36}$$

Thus, it is possible to write the expression of the ratio between the amplitude of the reflected on the incident wave at the interface, the so-called *amplitude reflection coefficient* R_a:

$$R_a = \frac{p_r}{p_i} = \frac{A_r}{A_i} = \frac{Z_2 - Z_1}{Z_1 + Z_2}$$

Looking at the phenomenon from an energy perspective, the *intensity reflection coefficient* R_I can be defined analogously to the previous one, but considering the intensity of the reflected (I_r) and incident (I_i) waves:

$$R_I = R_a^2 = \frac{I_r}{I_i} = \frac{(Z_2 - Z_1)^2}{(Z_1 + Z_2)^2}$$

Using the simple principle of energy conservation ($I_i = I_r + I_t$), the intensity transmission coefficient T_I results: $T_I = 1 - R_I$.

Taking in consideration the example in the previous subsection, one can see that at the interface between glass and water the majority of the incident wave is reflected, due to the large difference in acoustic impedance between the two materials:

$$R_I^{gl-wa} = \frac{(Z_{gl} - Z_{wa})^2}{(Z_{wa} + Z_{gl})^2} \approx 78\%$$

Standing waves and acoustic resonance

When two or more waves meet, they interact with one another giving raise to the phenomena of interference. This means that at every time instant there would be a sum of pressure (i.e. displacement) waves in every spacial point, like a superposition of effects. Hence, a sound wave would interact with its reflected part once it bounce back from the interface, generating a standing wave (subscript $_{SW}$). Assuming for simplicity a travelling wave in the positive direction p_i incident on a perfect rigid boundary ($R_I = 1$, meaning $A_r = A_i = A$) and its reflected wave p_r, from Eq. 2.31a one can write the equation for the interference of the two waves as:

$$p_{SW} = p_i + p_r = \rho_0 \omega A \Big(\cos(\omega t - ky) + \cos(\omega t + ky) \Big)$$

that yields to:

$$p_{SW} = 2\rho_0 \omega A \cos(ky) \cos(\omega t) \tag{2.37}$$

Analogously for the velocity definition as in Eq. 2.31b, one can write:

$$v_{SW} = v_i + v_r = kA \Big(\cos(\omega t - ky) - \cos(\omega t + ky) \Big)$$

that would give:

$$v_{SW} = 2kA \sin(ky) \sin(\omega t) \tag{2.38}$$

Applying the definition of displacement as time integral of the velocity:

$$s_{SW} = \int v_{SW} \, dt = -\frac{2}{c} A \sin(ky) \cos(\omega t) \tag{2.39}$$

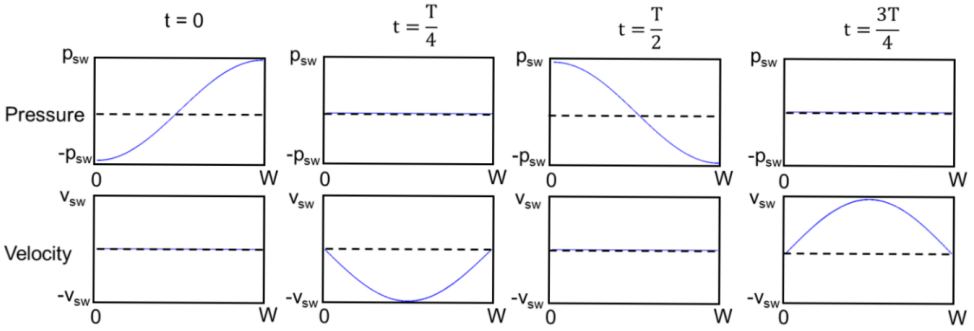

Figure 2.3: Pressure and velocity during a period T for a standing wave resonating in a channel having width $W = \lambda/2$. Figure courtesy of David Van Assche, from [69].

The displacement function will be zero at intervals of half a wavelength, in which the medium particle do not move and thus these stationary points are defined as displacement *nodes*. The maximum oscillations are alternated to these latter points by quarter of a wavelength in the so-called displacement *antinodes*. Nodes and antinodes can be analogously defined as done for displacement for every standing wave.

It is worth noting the phase shift of $\pi/2$ in space between displacement and pressure waves, while

in time they behave the same (only with opposite sign). On the other hand, velocity and pressure have a $\pi/2$ displacement both in time and in space. This means that the total energy of the system is periodically converted between potential energy $E^p = -\int_{V_0}^{V}(p/V)dV$ (linked to the pressure and stored as compression/rarefaction) and kinetic energy $E^k = \frac{1}{2}\rho_0 v^2$ (linked of course to the velocity). Considering the conservation of energy for volume unit and the time average of time harmonic fields, one can write the total time-averaged acoustic energy density as:

$$E_{ac} = E^p + E^k = \frac{1}{4}\Big(\rho_0 v^2 + \kappa_0 p^2\Big) = \frac{|p_{SW}|^2}{4\rho_0 c_0^2} = \frac{|p_{SW}|^2 \kappa_0}{4} \tag{2.40}$$

in which $|p_{SW}|$ represents the pressure standing wave amplitude.

If the frequency is well tuned to the system geometry and the wave meets the interface at a multiple of half a wavelength, the phenomenon of resonance occurs, greatly amplifying the wave energy thanks to the resulting constructive interference; in ideal system, the energy would go towards infinite, but in reality there is an upper limit to the energy waves resonance can achieve due to the dissipation within the medium where the wave propagates. There are many reasons why it is advantageous to operate acoustofluidic devices at the resonance mode: besides delivering the maximum acoustic power from the transducer to the fluid, it makes the phenomena reproducible and stable. This has allowed to study and exploit the phenomena of acoustic radiation force on particles and of acoustic streaming in fluids, both of which are explained in the following section.

2.2.4 Acoustic Waves in fluids

In order to bridge the acoustics theory and its applications in microfluidics, it is necessary a premise. The mechanical vibration in the microchip derives by a lead zirconate titonate(PZT) transducer, actuated by a sinusoidal current; this current is usually in the MHz range, in order to generate waves in resonance with the acoustic cavity in the device. One fundamental concept is the coupling between the actuator and the chip. Usually the PZT is fixed on it by using some glue, with what is called the *acoustic coupling layer*: non uniform thickness in this latter one can generate huge variability and make the modelization of the whole system extremely difficult. Furthermore, the resonance in the dimension of interest is definitely not the only physical phenomenon that takes place: resonances in the other dimensions, mechanical energy dissipation and particle-particle interactions are just few of the observable interactions that arise in such systems. A scheme of the acoustofluidic physics is shown in Fig. 2.4.

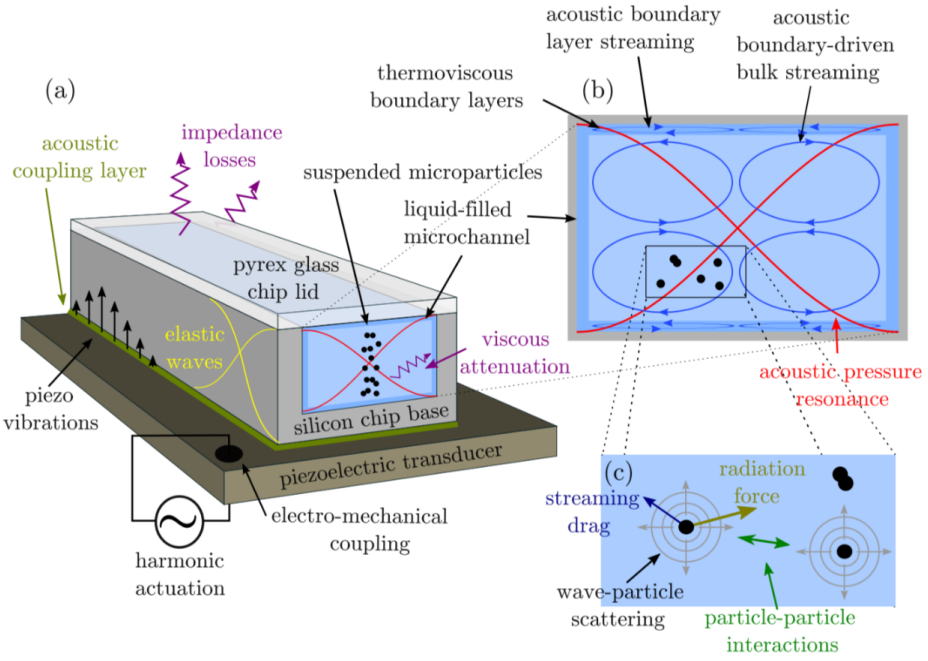

Figure 2.4: (a) A schematic of a classic acoustofluidic device: the PZT (brown) is glued via the acoustic coupling layer (green) to the microchip (gray) and it is harmonically actuated. This generates physical phenomena both in the chip bulk and in the channel (light blue). (b) A transverse half-standing wave (red) is imposed in the channel cross-section, generating acoustic streaming. (c) zoom-in on the microparticles (•), subjected to the streaming-induced drag force and to the acoustic radiation force. Figure courtesy of Rune Barnkob, from [64].

Below the two principle phenomena of interest in acoustofluidics are explained: the primary radiation force and the acoustic streaming. These are both dependent on the non-linear effects of the acoustic resonance, meaning that they arise from effects that have non-zero time-average in an harmonic oscillation. Then, after the critical-size derivation, the acoustic body force is introduced, which aims to give a coherent ed unique mathematical description of all the above mentioned phenomena.

Primary radiation force

When an acoustic wave travelling in a suspension meets a particle having different acoustic properties compared to the surrounding fluid (i.e. $\rho_p \neq \rho_0$ and $\kappa_p \neq \kappa_0$), a so-called *primary acoustic radiation force* (PRF) arises. This phenomena was first studied by King [70] in 1934 for incompressible particles in inviscid fluid and later expanded for compressible ones by Yosioka and Kawasima [71]; their works were summarized by Gorkov for plane acoustic waves in 1962 [72], while more recently the phenomenon was described taking also into account the fluid viscosity by Settnes and Bruus in 2012 [73]. Travelling acoustic waves would be scattered by the difference in acoustic impedance between the fluid and the particles, thus generating a momentum transfer on the suspended bodies that then, averaged in time, results in the PRF causing the particles motion relative to the fluid. In this work, the Gorkov's approach to approximate the PRF with 1D standing planar waves has been considered.

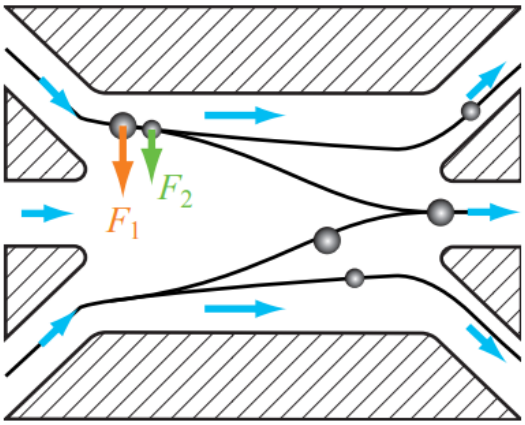

Figure 2.5: The Primary Radiation Force (PRF) magnitude is heavily dependent on the particle radius: bigger particles would be subjected to larger forces (orange arrow), while smaller particles to smaller forces (green arrow). It is then possible to perform particle size-separation tuning the inlet/outlet flows. Figure courtesy of Per Augustsson, from [67].

Hypothesising particles of radius a much smaller than the acoustic wavelength λ, the PRF for a half wavelength standing wave can be written as:

$$\mathbf{F_{rad}} = 4\pi\Phi a^3 k_y E_{ac} \sin(2k_y y)\mathbf{e_y} \tag{2.41}$$

in which

$$\Phi = \frac{\rho_p - \frac{2}{3}(\rho_p - \rho_0)}{2\rho_p + \rho_0} - \frac{1}{3}\frac{\kappa_0}{\kappa_p} \tag{2.42}$$

that is the *contrast factor*: if positive, it would result in a force pointing towards the pressure nodes, while if negative it would make the particles move towards the pressure antinodes. Neglecting the particles momentum, it can be written the equilibrium for the forces acting on a particle considering the balance between the acoustic force and the one due to the friction as in Eq. 2.20:

$$\mathbf{F_{rad}} + \mathbf{F_{Stokes}} = 0 \tag{2.43}$$

From this balance it is possible to obtain the expression for the particle radiation velocity $\mathbf{u_{rad}}$:

$$\mathbf{u_{rad}} = \frac{2\Phi}{3\eta} a^2 k_y E_{ac} \sin(2k_y y)\mathbf{e_y} \tag{2.44}$$

For plane wave it is safe to say that the only PRF component that matter is the one in the wave propagation direction, while the one in the perpendicular direction is orders of magnitude smaller [79] and then safe to be neglected for the scope of this work.

Acoustic streaming

Sound propagating into a real homogeneous fluid would inevitably generate acoustic streaming. This is due to the viscosity effect that implies dissipation of energy both with the distance travelled by the wave and with the boundaries of the system. The phenomena is bound to the non linearity in the second-order pressure and velocity fields of the acoustic wave, according to the perturbation scheme (the reader willing to know more about the topic is referred to [64], [74] and [75]) The dissipation

mechanism makes part of the wave energy to be converted into fluid motion [76]: it is possible to identify three different type of streaming:

- Eckart streaming, that is due to bulk attenuation of the sound wave and it is characterized by a scale much larger than the acoustic wavelength (reason why it is not consider in this thesis work, being the focus on a physical scale similar to the sound λ);
- Schlichting streaming, also known as *inner boundary layer streaming*, has a scale that is much smaller than the acoustic wavelength;
- Rayleigh streaming, also known as *outer boundary layer streaming*, has a scale comparable to the acoustic wavelength.

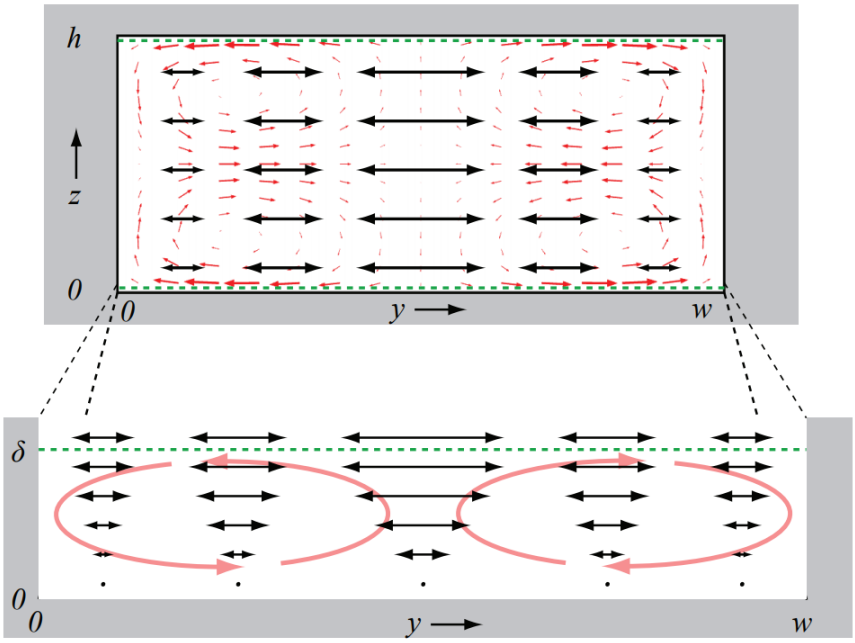

Figure 2.6: Acoustic streaming in a half-wavelength resonator. In black it is shown the oscillating first order velocity field. In the zoomed in part one can see the velocity going to zero at the walls, causing a steep velocity gradient and the consequent Schlichting streaming. It is this inner boundary layer streaming that drags along the four streaming rolls observable in the fluid bulk. Figure courtesy of Per Augustsson, from [67].

Schlichting and Rayleigh streaming are tightly bounded. The former one originates from the zero velocity that the wall impose on the fluid molecules adjacent to it (as already explained in section 1.4). The oscillatory pressure in the bulk implies a non-zero velocity of those fluid particles, while at the same time the boundary condition impose a zero velocity: this creates a very steep velocity gradient in the thin fluid layer close to the wall (<1 µm). Due to the different magnitude of the oscillatory velocity in the bulk, there will be differences in the gradient that is generated depending on the spacial coordinates across the resonator width. This will generate the streaming in the thin boundary layer that, as a consequence, will drag the bulk fluid in a counter flow due to the viscosity of the different fluid lamina sliding on one another. This macroscopic streaming occurring in the bulk is named after Lord Rayleigh, who first described mathematically the phenomenon of a streaming

velocity induced by standing waves parallel to a rigid surface [77]. Hence, the velocity in the bulk can be mathematically expressed as:

$$u_{str} = -\frac{3}{8}\frac{|v_{ST}|^2}{c_0}\sin(2k_y y) = -\frac{3}{2}\frac{E_{ac}}{\rho_0 c_0}\sin(2k_y y) \tag{2.45}$$

For more depth in the analytical solutions of acoustic streaming in rectangular cross-section the reader is referred to [78].

Critical size

Considering a suspension in a rectangular cross-section of width W in which a half wavelength standing wave is applied, like the case in study in this thesis work, the phenomena of acoustic radiation force and acoustic streaming coexists. As seen in the previous two sections, the former acts directly on a particle, while the latter affects the surrounding fluid; a comparison between the velocities induced by these two would give:

$$\frac{u_{str}}{u_{rad}} = \frac{9\eta}{8\pi\Phi a^2 \rho_0 f} = \frac{9\eta W}{4\pi\Phi a^2 \rho_0 c_0} \tag{2.46}$$

From this equation it is possible to derive a critical particle radius a_c for which the magnitude of the streaming and radiation velocity are equal. For particles below this critical size the streaming would dominate the motion, while particle bigger than a_c the radiation force would be dominant; so, if we balance the two velocities (i.e. a ratio equals to 1), one can derive a formula for the critical radius from Eq. 2.46:

$$a_c = \sqrt{\frac{9\eta W}{4\pi\Phi\rho_0 c_0}}$$

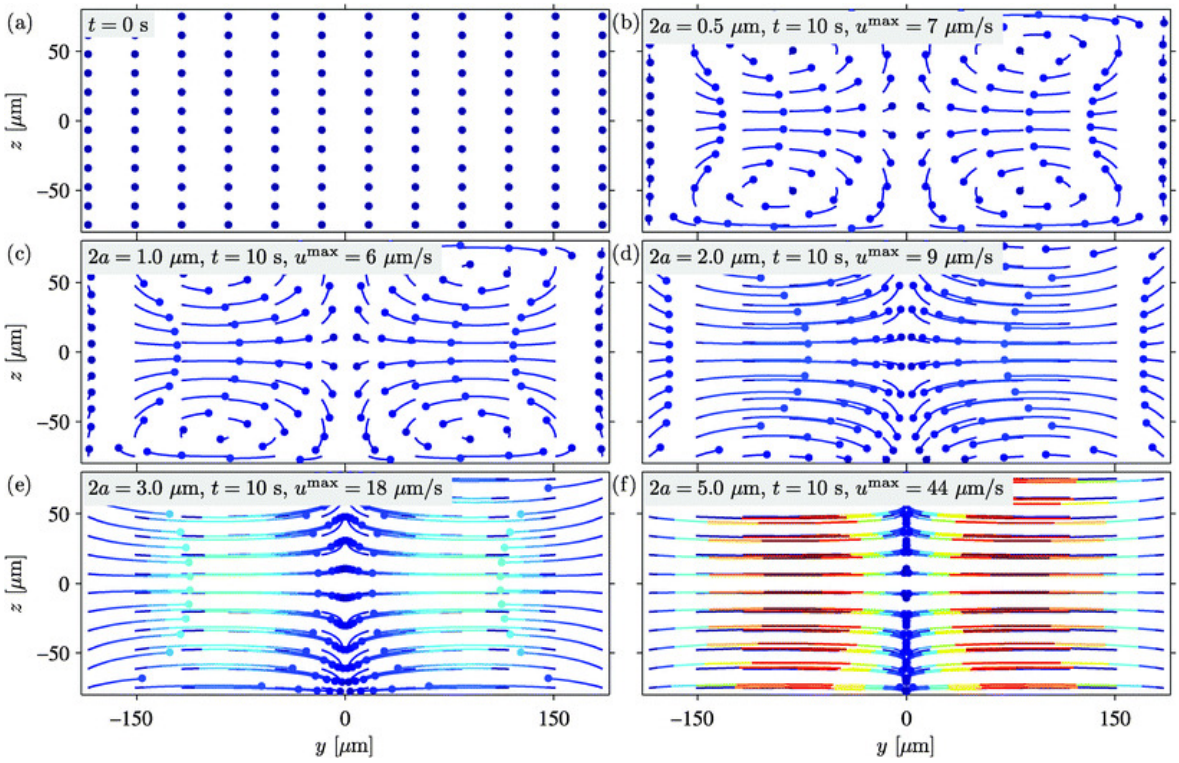

Figure 2.7: Plots showing different behaviour inside an acoustic resonator depending on the different particle sizes. Starting with an initial position at t=0 equal for everyone (a), the particles after 10 s have behaved quite differently according to their size: (b) 0.5 µm and (c) 1 µm particles follow pretty well the acoustic streaming rolls, while with larger radius like (d) 2 µm, (e) 3 µm and (f) 5 µm the primary radiation force dominates, focusing the particles at the center. Reproduced with permission from [79]

In any case, assuming as an example any size particle with positive contrast factor Φ, the PRF would be null at the center of the channel, thus yielding to no u_{rad} and, knowing that there is no component in the z-direction, only u_{str} would affect the particle motion: if focused, the particle will therefore end up to the ceiling or the bottom of the channel, no matter how large it is.

Acoustic body force

It has been shown recently that a similar phenomenon to the PRF occurs when there is a difference in acoustic impedance between adjacent fluid particles [80]: a force density $\mathbf{f_{ac}}$ is generated due to the nonzero divergence of the time-averaged momentum-flux-density tensor $\mathbf{\Pi}$ at the interface [81]:

$$\mathbf{f_{ac}} = -\nabla \cdot \langle \mathbf{\Pi} \rangle$$

This means that there is no difference when a sound wave meets an object or a fluid particle, the important is the acoustic impedance change. This concept allowed researchers to stabilize or even relocate fluid with different densities in order to have density gradient across the channel width [81], formulating the body force as:

$$\mathbf{f_{ac}} = -\frac{1}{4}\nabla\kappa|p_1|^2 - \frac{1}{4}\nabla\rho|v_1|^2 \tag{2.47}$$

At the interface between two fluids with different physical properties (great differences in κ and

ρ), the body forces thus generates a stabilizing effect that greatly suppress the acoustic streaming, as shown by Qiu et al [82]. The stability is nonetheless affected by diffusion, meaning that the chemical gradient, even in absence of convection, fades out according to Fick's laws (as explained in Section 2.1.5). Hence, the acoustic streaming will not be suppressed indefinitely, but its magnitude will actually increase faster and faster with time: with the early diffusion the acoustic impedance difference decreases, allowing the streaming to gain strength and creating more convection that would sum up to the diffusion, thus increasing the initial effect in a positive feedback. So with this technique the streaming suppression will be secured just for a limited amount of time.

2.3 Heat exchange

In this section the fundamentals of heat transfer are introduced, followed by the physics laws and concepts needed to understand the thermal field in microfluidic devices.
The main sources used for this chapter are two basic physics book, *Transport phenomena* by Bird, Stewart and Lightfoot [62] and *Concepts in Thermal Physics* by S.J. Blundell and K.M. Blundell [83].

2.3.1 Temperature and heat

There is no clear and unique definition of temperature (T), but a trivial one might be that it defines how hot, or cold, a body is. Empirically, one can easily experience the implications of the concept of temperature: if two insulated bodies 1 and 2 are at temperature $T_1 > T_2$ and they are then placed in thermal contact with each other, there will be an energy transfer from 1 to 2, untill they reach the same T_f. This process can be called *thermalization* and it has been framed as the 0th law of thermodynamics.
From the atomic/molecular point of view, it is possible to define T in two related ways. A kinetic definition, more intuitive and easily applicable to material such as gas, and a probabilistic definition, more complicated to understand, but much more reliable and useful for describing physical phenomena.

To define the temperature in a kinetic fashion, a useful example is to consider a monoatomic gas. T is a quantification of the kinetic energy each atom has, meaning the higher it is, the faster the atom moves. If this gas is placed in contact with another gas at a lower T, the molecules of the hotter one will have higher chances of colliding with the second ones, thus transferring them energy via elastic collision. This is a rough definition of kinetic temperature. The concept gets more tricky when approaching more complex materials, such as liquids and solids. In these cases, binding the definition of temperature to the translational kinetic energy is reductive if not completely wrong. It makes much more sense relating it to the vibration and rotation of the single molecules and the links between them, considering that the translation is quite small in liquids and non-existing in solids. In order to help visualizing this, let's imagine that the atoms in a metal were balls bound together by springs: the higher the temperature, the more this spring will be strained by the larger motion of the two balls, until the deformation is such that the spring yields, resulting in a melted material.

To approach the probabilistic definition, the concept of micro- and macro-state of a system have to been introduced. The macrostate is what is commonly measured for each part of a system and it can be characterized by temperature, volume, pressure and other macroscopic quantities. It does not change with time in an isolate system. A microstate, on the contrary, focus on the energy level of every molecule at each time instant: it is like an instantaneous photo of all the energy configurations each basic constituent a system has. The following instant, the microstate will be different because the single molecules will have different position, velocity or energy, but the overall total energy of the whole has not changed. Again, it is easier to visualize this concept thinking of a monoatomic gas in an insulated environment: if at a time $\bar{t}$ each atom has its own velocity and position, the instant $\bar{t} + \mathrm{d}t$ every atomic configuration will be different, although only slightly, due to their random movements and collisions. The same thing is valid for solids, even if in this case it is the vibration of the atoms around their equilibrium position and not their translation to give the variability. The fundamental assumptions are that every single microstate is possible and equally likely to occur, and a system, if given sufficient time, will experience all the possible states and spend equal amount of time in each

one of them. Considering that, as it has been stated above, the microstate is continuously changing while the macrostate is not, thus this latter one can be thought as the configuration resulting from the largest number of microstates. Hence, in probabilistic terms, the macrostate is the arrangement at which the number of corresponding possible microstate has been maximized. Linking these concepts back to the *thermalization*, two systems will exchange energy in order reach a configuration with the most microstates, a process normally known as "having the same T". Considering a system with number of microstates Ω and energy E, its temperature T can be defined as:

$$\frac{1}{k_B T} = \frac{\mathrm{d} \ln \Omega}{\mathrm{d}E} \tag{2.48}$$

in which k_B is the Boltzmann constant. In statistical mechanics, this expression can be rearranged defining the quantity $k_B \ln \Omega$ as the entropy S of a system, which is, put in very simple terms, a measure of its disorder:

$$\frac{1}{T} = \frac{\mathrm{d}S}{\mathrm{d}E} \tag{2.49}$$

Linking the probabilistic and the kinetic definitions of temperature there is the velocity distribution theorized by Maxwell-Boltzmann, who derived the average velocity of a gas molecule as a function of its temperature T and mass m, making hence possible to link the mean kinetic energy with the temperature:

$$\langle E_k \rangle = \frac{1}{2} m \langle v^2 \rangle = \frac{3}{2} k_B T \tag{2.50}$$

The reader interested in deepening these concepts is referred to [83].

To link back this concepts of temperature with the fluids, it is useful to look at the dependence on T of two quantities already introduced in the previous sections: density and speed of sound.

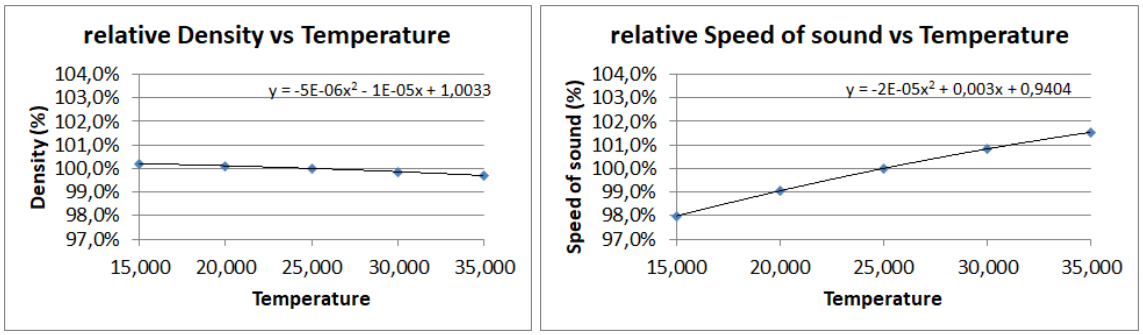

(a) (b)

Figure 2.8: The two quantities are represented relative to the values measured at 25°C. All the measurment were performed by the Acoutofluidics group at BME, Lund University.

As one can easily notice, the density (Eq. 2.3a) decreases with T, due to the higher kinetic agitation of the molecules that makes fewer of them fit in the same volume ΔV. The speed of sound (Eq. 2.13c), on the contrary, increases with T. With higher temperatures there is in fact higher level of motion of the fluid molecules, meaning that less energy is needed to induce the same pressure change.

Heat, on the other hand, can be easily defined as thermal energy in motion, here expressed with the letter Q. Intuitively, the experience of heat is one of the most natural ones: sitting in front of a fire can make easily perceiving the warming feeling coming from it, while holding a piece of ice in

the hand can be easily associated to a heat flux leaving the body and melting it. Hence, heat can be thought as energy transfer and there are different ways in which the it can happen:

- **Conduction**, that can be defined as molecular energy transport. This concept will be deepened in section 3.2.
- **Advection**, that is energy transport due to bulk motion of a fluid. It depends heavily on the forces acting on the fluid and its density and it can act at great distances: it is the main way in which heat is transported across the globe by oceans with surface or abyssal currents.
- **Radiation**, that is the only energy transfer that does not require physical contact and can act at incredible long distances. An example is how the sun irradiates and warms Earth with its rays.

The more known term of "convection" is referred to the combination of advection and conduction, meaning that the contributions due to the bulk velocity of a fluid and to the spatial gradients within it are both considered.
The amount of heat $\mathrm{d}Q$ necessary for a system to increase its temperature of $\mathrm{d}T$ (at constant pressure) can be quantified thanks to its heat capacity C_p:

$$C_p = \frac{\mathrm{d}Q}{\mathrm{d}T}$$

which can be expressed independently on the mass of the system m by the specific heat capacity c_p:

$$c_p = \frac{C_p}{m}$$

The specific heat capacity is a physical material property and it helps defining the amount of heat that needs to be given to an object unit mass in order to increase its temperature: as explained above, there are multiple factors that can influence how heat is distributed in a system and thus how the T changes. For example, constant volume or pressure can have heavy impact on these experiments and thus the specific heat capacity has been sampled with different constrained, mapping in tables its changes for various materials.

2.3.2 Heat conductivity and conduction

Another interesting material properties is heat conductivity k_{th}. This indicates how easily heat can spatially flow from a region of high temperature to one with low T. This relation has been formalized into the Fourier's law of heat conduction, that in the 1D formulation along a direction y can be expressed as:

$$q_y = -k_{th}\frac{\mathrm{d}T}{\mathrm{d}y} \tag{2.51}$$

in which $q = Q/A$ is the heat flux, that has the expression of an heat flow Q through a surface A. This means that the flow of thermal energy along one direction is proportional to the temperature decrease along that direction. The negative sign indicates that the heat moves from the higher T to the lower one, against the temperature gradient. Considering that this mechanism applies in all directions, its

generalization in 3D for an isotropic material can be written as:

$$\mathbf{q} = -k_{th}\nabla T \tag{2.52}$$

in which $\mathbf{q}$ is the vector representing q_x, q_y and q_z. In case of an anisotropic material, the thermal conductivity k_{th} can be substituted by the thermal conductivity tensor $\mathbf{k_{th}}$, that is a symmetric second order tensor representing the different $k_{th}^{ij} = k_{th}^{ji}$ in every direction combination.

As the heat capacity, the thermal conductivity has been mapped for different materials and, if not tabulated for the conditions of interest, it can be derived by using state-charts that express k_{th} as function of T, with different curves according to the pressure p at which the measures have been conducted. In general, k_{th} for low density gases increases for increasing T, while for liquids it decreases with increasing T. This makes sense linking back with the kinetic definition of temperature: on one hand, for a gas the heat transfer happens mostly via collision between moving molecules/atoms, hence the faster they move, the easier it will be to transfer heat. On the other hand, for liquids it is not translational energy but mostly vibrational and rotational energy that play a key role in heat transport: with higher T, the distance between molecules increases, making the transfer less effective. Nonetheless, polar liquids such as water may have a maximum in the dependence of k_{th} on T. Solids like metals mainly transfer heat through electron movements and their thermal conductivity k_{th} decreases with T, due to the higher atomic agitation.

It is pretty obvious to see a parallelism between Eq. 2.51, the 1D Fick's law on diffusion in Eq. 2.14 and the 1D formulation of Newton's law of viscosity as in Eq. 2.1: in all cases there is a flow proportional to the negative gradient of a macroscopic variable, in which the proportionality coefficient is a physical properties of the material (that depends on temperature and pressure). When comparing the 3D formulations of such laws (Eq. 2.52, 2.15 and 2.2) there are some differences between the former two and the latter one, mainly due to the fact that energy and mass transfer are scalars while momentum is a vector, meaning that in three dimensions the former flows become vectors, while the momentum flow is a second order tensor.

2.3.3 The heat equation

To look at how heat (and thus temperature) change with time, one has to approach the so-called heat diffusion equation. Considering an isolated volume V with surrounding closed surface A, it is possible to write an equilibrium equation considering the heat flux $\mathbf{q}$ leaving the system and the variation of internal energy:

$$\int_A \mathbf{q}\ \mathrm{d}A = -\frac{\partial}{\partial t}\int_V C_p T\ \mathrm{d}V \tag{2.53}$$

Applying the divergence theorem, one can write:

$$\int_A \mathbf{q}\ \mathrm{d}A = \int_V \nabla\cdot\mathbf{q}\ \mathrm{d}V$$

Inserting this relation into Eq. 2.53, it is possible to write:

$$\int_V \Big(\nabla\cdot\mathbf{q} + \frac{\partial}{\partial t}C_p T\Big)\mathrm{d}V = 0 \tag{2.54}$$

that is true when the integral argument is 0. This yields to:

$$\nabla \cdot \mathbf{q} = -C_p \frac{\partial T}{\partial t} \tag{2.55}$$

Combining this equation with Eq. 2.52, one gets the expression of the thermal diffusion equation:

$$\frac{\partial T}{\partial t} = \alpha \nabla^2 T \tag{2.56}$$

in which $\alpha = k_{th}/\rho c_p$ is the thermal diffusivity. The Fourier's law on conduction is a particular case of the heat equation, considering a steady state (i.e. $\frac{\partial T}{\partial t} = 0$)

2.3.4 Energy balances and T distributions

In order to understand the temperature distributions across a system, one can formulate the heat equation using the so-called *shell* balance. This approach consists in an energy balance over a suitable thin region, taken with heat flow perpendicular to its surface: doing so it is possible to obtain the heat flux distribution out of it (as in Eq. 2.55). Then, substituting this into the Fourier law for conduction gives the first-order differential equation of T depending on the position. Of course, suitable boundary conditions are needed: the T has to be specified at a surface, q normal to the surface must be given and the continuity of T and q at interfaces is essential. Furthermore at a solid-liquid interface, the normal heat component is related to the difference in T between the wall temperature and the fluid bulk one.
Doing so, one can formulate energy balances and calculate the consequent T distributions across composite system, with good approximation and suitable boundary conditions.

2.3.5 Electric circuit analogous

Considering a composite system (i.e. made up by several materials in thermal contact with each other) at steady state, an heat flux flowing between them will cause the T profile to behave differently in each material, according to its physical properties. A simple way of looking at this problem might be an "electrical" approach to the heat exchange: as in Eq. 2.51, one can notice that there is a flux proportional to some kind of driving force or potential (in this case a difference in temperature). So, rewriting the equation as in the most known of Ohm's rules $\Delta V = RI$ and considering the resistance $R = 1/\sigma * l/A$, with σ electrical conductivity (material property), l length and A area of the material to be crossed (geometrical property):

$$\nabla T = -\frac{1}{k_{th}} q$$

that, integrated in one dimension (between the initial and final points y_i and y_f) with suitable boundary conditions and constant $q = Q/A$, yields to:

$$\Delta T = T_f - T_i = -\frac{y_f - y_i}{k_{th}} \mathbf{q} \tag{2.57}$$

where $-\frac{y_f - y_i}{k_{th}}$ is the material thermal resistance per unit area. This make sense because the easier the conduction is (higher k_{th}), the lower the resistance is, while the longer the path the heat has to transit inside the material, the higher the resistance is.

2.3.6 Conduction VS Convection

When looking at the two heat transport mechanisms that happens when there is thermal contact between fluid and solid, meaning conduction and convection, one has to understand which one is predominant in order to determine the phenomenon that influence the most the system T profile. In order to do this, it is useful to calculate some non-dimensional numbers characterizing the ratio between these motion components.

$$Pr = \frac{\nu}{\alpha} = \frac{\eta/\rho}{k_{th}/\rho c_p} = \frac{c_p \eta}{k_{th}} \tag{2.58}$$

in which ν is the kinematic viscosity and α the heat diffusivity. This number, called Prandtl number for the German engineer Ludwig Prandtl, shows the ease in which momentum versus energy transport can happen in a system. Pr is a dimensionless quantity only depending on material physical properties. Another useful adimensional number is Peclét number: in a system with characteristic length L and fluid bulk velocity v it expresses the ratio between the advective motion and the diffusive one:

$$Pé = \frac{Lv}{\alpha} = \frac{Lv\eta/\eta}{k_{th}/\rho c_p} = \frac{\rho L v}{\eta} * \frac{c_p \eta}{k_{th}} = Re * Pr \tag{2.59}$$

This compares the preponderance of the quantity of energy that is exchanged via fluid motion (at the numerator) with the one exchanged via diffusion (at the denominator).
The time scales at which the diffusion occurs along one direction y can be derived by the heat equation as:

$$t_{1D} = \frac{y^2}{2\alpha} \tag{2.60}$$

while the time scale at which convection happens along the y direction is more related to the bulk velocity v of the fluid, meaning that it can be estimated by reversing the simple definition of velocity:

$$t = \frac{y}{v} \tag{2.61}$$

Chapter 3

Experimental procedure

In this section the experimental work done in this thesis is presented and discussed. It starts with a brief introduction to the set-up used, both regarding the holder fabrication and the T control automation, while more detailed information on the materials and methods can be found in Appendix. Every part making up the investigation has its own paragraph, in which the methodology is briefly explained and then the results are discussed; once again, for details about the materials and methods used, the interested reader is referred to Appendix.

3.1 Set-up and experiment design

The fundamental part for a microfluidic experiment is of course the chip. Furthermore for acoustofluidics, as explained in the theoretical background, channel geometry plays an important role: it is at the interface between different materials that the sound waves are reflected and thus a standing wave is generated. Ideally for a single-node acoustic resonator, one would have a rectangular cross-section with a width equal to half a wavelength of the actuating sound: this latter should also match the resonating frequency of the piezo-electric element, in order to generate the highest possible energy in the mechanical vibration. With a resonating PZT 1 mm thick, one gets its resonating frequency f as:

$$\frac{\lambda_{PZT}}{2} = 1\ mm; \quad f = \frac{c_{PZT}}{\lambda_{PZT}} = \frac{4000\ m/s}{2\ mm} = 2\ MHz$$

Considering then the speed of sound in water $c_w = 1500\ m/s$, one would get a sound wavelength λ:

$$T = \frac{1}{f}; \quad \lambda = cT \quad \Longrightarrow \quad \lambda = \frac{c}{f} = 750\ \mu m$$

Hence, the channel width should be $\lambda/2$, i.e. around 375 µm.
The chip that was used in this thesis work was produced by the Ångström laboratory, Uppsala University. It was designed as a glass-silicon-glass microfluidic device, with a silicon wafer (150 µm thick) etched through and then anodically bonded on both sides with glass lids, one thin (200 µm) and one thick (1.1 mm). The channel cross-section was supposed to be rectangular, as high as the silicon wafer thickness and with width 375 µm, equals to the previously calculated half wavelength at 2 MHz. However, probably due to some problems during the etching, the channel had in reality a trapezoidal cross-section, as shown in Fig. 3.1, with upper base of roughly 420 µm and lower one of

roughly 520 µm.

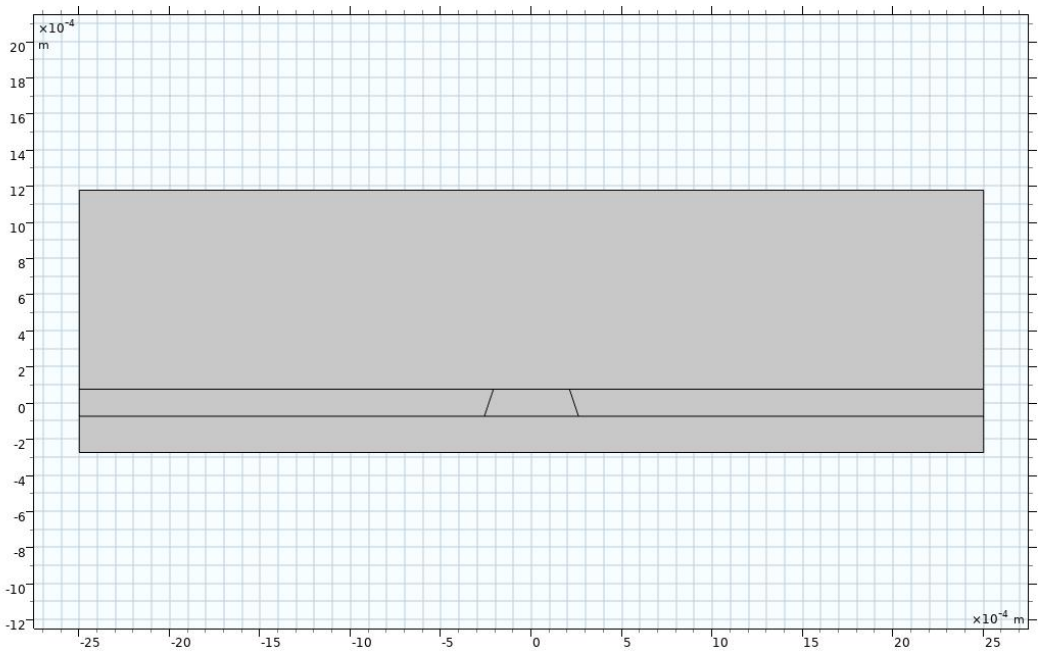

Figure 3.1: Schematic of the chip cross-section: the middle layer is silicon in which the channel had been etched (with the skewed side walls). Above it there is the thick glass (1.1 mm), while below there is the thin one (200 µm).

This was quite a big issue, since with this chip configuration the fields generated inside the acoustic resonator was severely altered compared to a rectangular cavity, but it is impossible to easily know to what extent. Nonetheless, the glass-silicon-glass configuration was thought to be more important than the channel geometry (in section **T field characterization** the reason will be explained in details), so the sandwich chip was used regardless of its channel geometry flaws.

3.1.1 Holder fabrication

One intuitive and reliable way to generate and maintain a temperature gradient across a microchannel is by heat conduction. In order to achieve that, the chip holder was designed with aluminum plates able to conduct heat to the channel from a heat source (peltier elements in this case). Preliminary results had shown that there were some deformations in the metal when heated, thus generating a shift in the depth at which the channel is placed during the observation (the chip image blurs with changing T). This led to the design of the final holder (Fig. 3.2), in which two thin (400 µm) aluminum plates were placed in a PMMA support that would act as insulation. Not only the pockets for the aluminum plates were milled in the polymeric base, but also a slot through the whole polymeric base thickness precisely below where the channel sits, in order to guarantee thermal decoupling of the two sides.

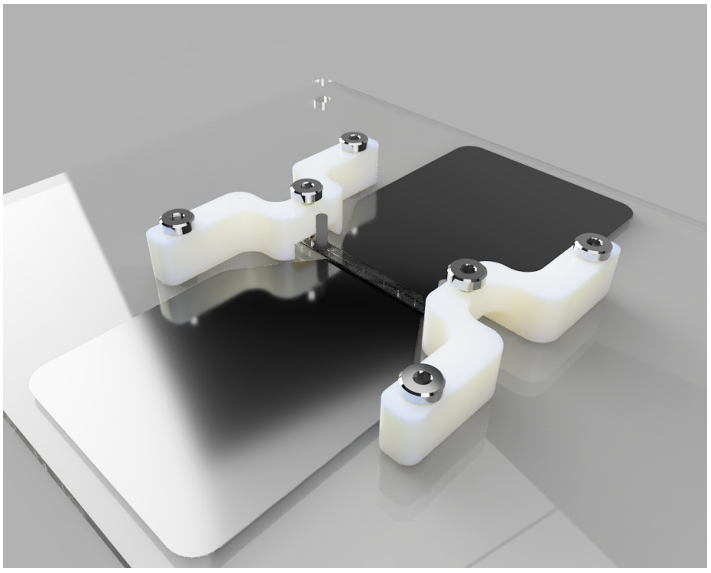

Figure 3.2: Rendering of the holder, designed via Fusion 360$^{\text{TM}}$. The PMMA base (transparent) and the two aluminum plates (dark gray) were milled to perfectly fit each other. The geometry guarantees heat conduction to the central region of the chip and thermal decoupling between the two sides. The two clamps for holding the chip in place (shown in white) were not produced.

Despite the modifications to the design, blurring still occurred; nonetheless, it was measured that if the focus was placed at the channel mid-height at room temperature, the defocused images intensity resulting from the aluminum thermal deformation would be quite similar, differing of just few percentage points. However, the blurring made the image processing more complicated, since the channel walls were not as easily detectable when the images were out of focus and this kept changing with the different set temperatures.

3.1.2 Experimental set-up

- **Automated T control**
  Two peltier element controllers (PID controller) were used to set and maintain the desired temperature on the aluminum plates. The temperature was measured via thermo-resistances Pt1000: one was placed on each aluminum plates to get the feedback for the controllers, while another one was placed on the top glass of the chip, to get a sense of the T stabilization. However, these resistances were proven to have a constant offset in the measured temperature, but it wasn't possible to fully characterize it with statistical significance for each resistance due to lack of time. The software *LabView* was then used to input settings to the two controllers and to store T data from their temperature sensors. Furthermore, another temperature probe was placed on the top of the chip on the thick glass, to help monitoring the T stability inside the channel; again, the data were recorded via a multimeter controlled via *LabView*. The goal of the software interface is to automate the set-up, allowing an user to set a range of temperatures independently on the two PID controllers and the time intervals at which the T shift has to happen, while at the same time recording the T data and images (with independent sampling rate).

- **Particle tracking**

General defocusing particle tracking (GDPT) [84] was used to track 1µm-diameter polystyrene particles inside the microchannel. This technique was applied on images collected using a cylindrical lens to have astigmatism in the measurements: the algorithm can then correlate the defocused image of the particle with a previously taken calibration stack, giving an estimate of the height at which it was in the recorded frame.
This approach was used to characterize the particle motion in the three situations involved in this thesis work, meaning a channel with only thermal gradient, with only acoustic field and with the two combined. It is good to keep in mind that the tracking algorithm assumes classic rectangular cross-section for the channel. Thus in the results the trajectories in such a plane will be displayed as if the channel was rectangular, with height of 150 µm (the silicon layer thickness) and width of 420 µm, like the upper (and smaller) base of the trapezoidal cross-section (as shown in Fig. 3.1).

3.2 Temperature field characterization

3.2.1 COMSOL model

A simple stationary thermal 2D model was set in COMSOL Multiphysics® 5.5 for the thermal gradient simulation in the system cross-section. Thanks to Jonas Helboe Jørgensen from DTU, who provided the basic model, it was possible to modify and simulate different configurations, both regarding the holder design and the experiment settings. The 2D configuration was defined via several parameters, both geometrical and physical, allowing to modify both the design and the material properties. Going from the bottom to the top, the displayed model represents the PMMA base, the thin aluminum plates and then the chip sitting on top of them, as a bridge in between. The model try to exemplify how the thermal gradient (set between 36 and 16°C) would develop: with a classic silicon-glass chip or with a glass-silicon-glass chip (so-called *sandwich*), as one can see respectively in Fig. 3.3 and 3.4.

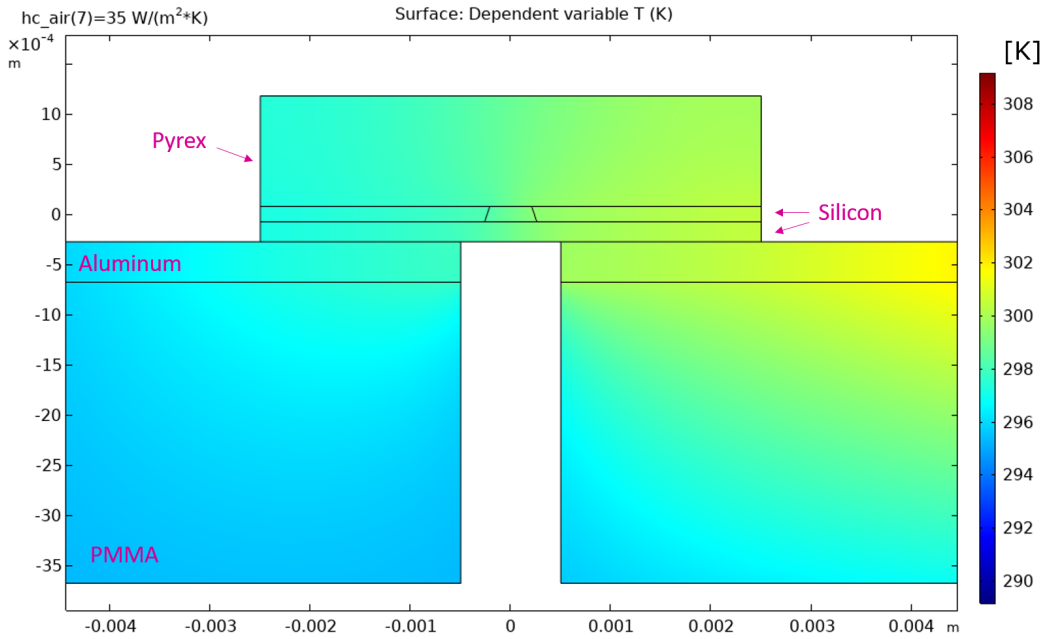

Figure 3.3: T color-map for a classic glass-silicon chip: as one can notice, the temperature decreases all along the system, from the hot peltier (right) to the cold one (left). The different materials of the chip are indicated in magenta.

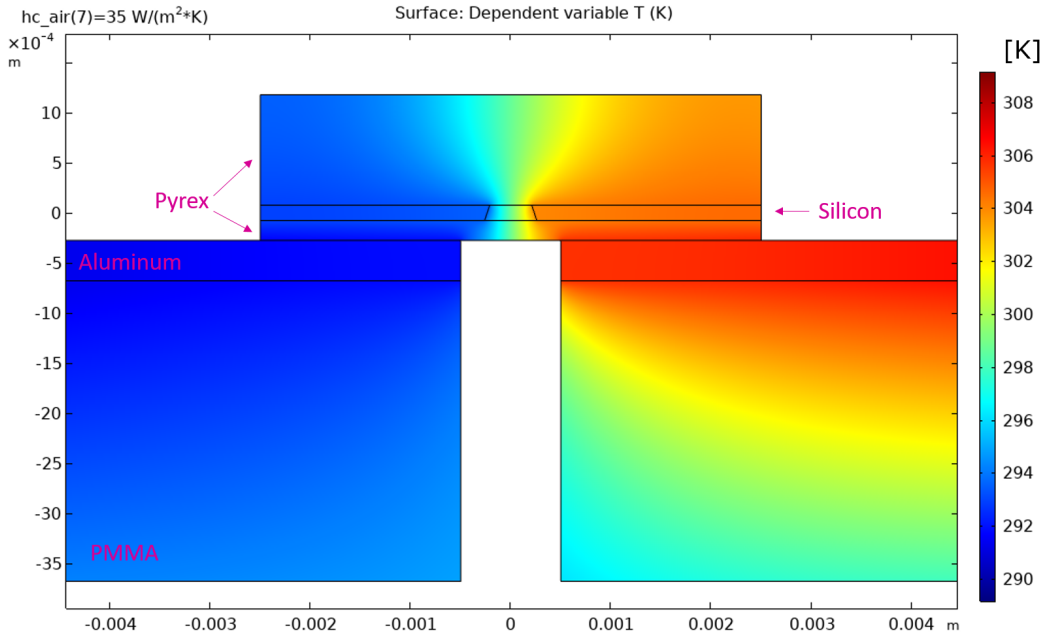

Figure 3.4: T color-map for a sandwich glass-silicon-glass chip: the temperature decreases steeply across the channel, with almost uniform high T to the right and low T on the left. The different materials of the chip are indicated in magenta.

The only difference in these two configuration is the material that is in contact with the aluminum plates: in the case of the more classic glass-silicon chip (Fig. 3.3), silicon is in contact with the aluminum. Thus, there is a low thermal resistance path directly linking the two peltier elements, going through aluminum, silicon and then aluminum again. This results in a gradient that develops

all along the system, meaning that the temperature difference across the actual channel is quite low, as shown in Fig. 3.5.

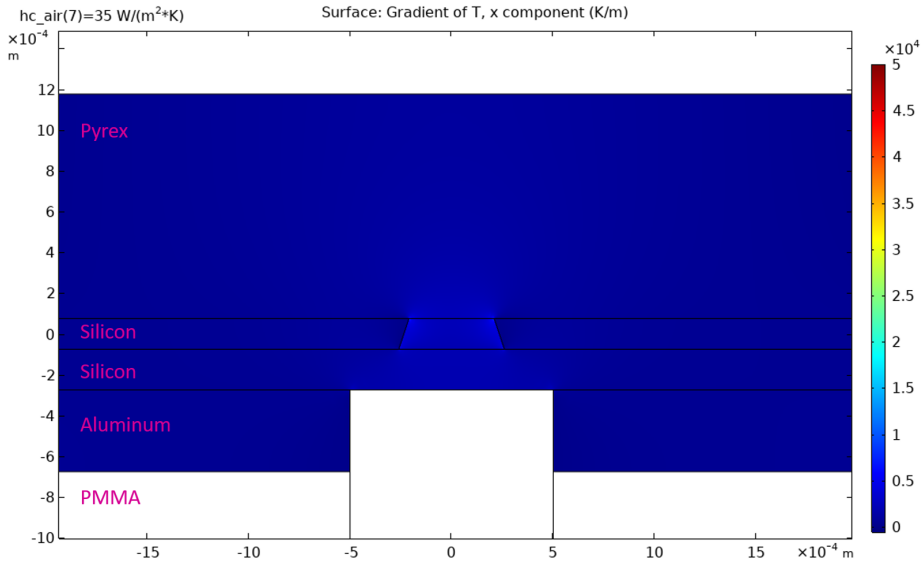

Figure 3.5: T gradient along the width dimension in a classic glass-silicon chip: most of the temperature variation is still across the channel, but clearly there are non-zero values all along the system. The different materials of the chip are indicated in magenta.

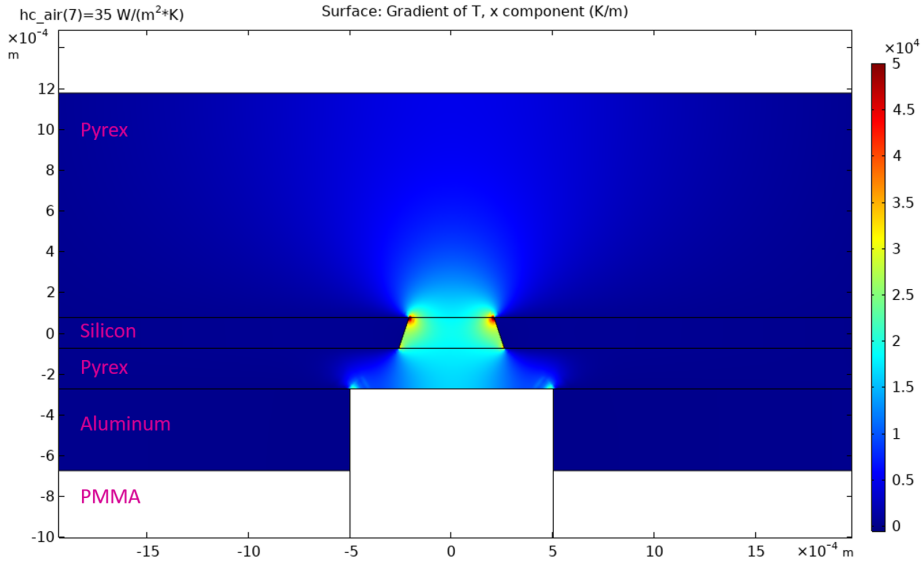

Figure 3.6: T gradient along the width dimension in a sandwich glass-silicon-glass chip: the temperature decreases steeply across the channel and its close surroundings, while in the rest of the system the T variation is very low. The different materials of the chip are indicated in magenta.

On the other hand, with the bottom of the chip made of glass, the lowest resistance path (according to the different material thermal conductivity k) that the heat flux can take is to go from the right aluminum plate to the glass for then reaching the silicon. From this one it goes through the water-filled channel to the silicon again, and then it proceed through the glass to reach the cold aluminum on the left. As one can see in Fig. 3.6, the temperature variation happens mainly across

the channel, while in the rest of the system it is close to zero. It is worth noting the different order of magnitude in Fig. 3.5 and 3.6: in the latter one the displayed variation is 10 times the scale in the former one, with roughly the same values across the whole system.

One of the aims of the model, besides chip design optimization, was to investigate the ideal temperature field generated inside the channel. With set temperatures of 36 °C on the right peltier and 16°C on the left one, the modelled T profile (Fig. 3.7) is quite linear and just near the walls has some nonlinear effects for the ceiling and bottom of the channel, while at the center is perfectly linear.

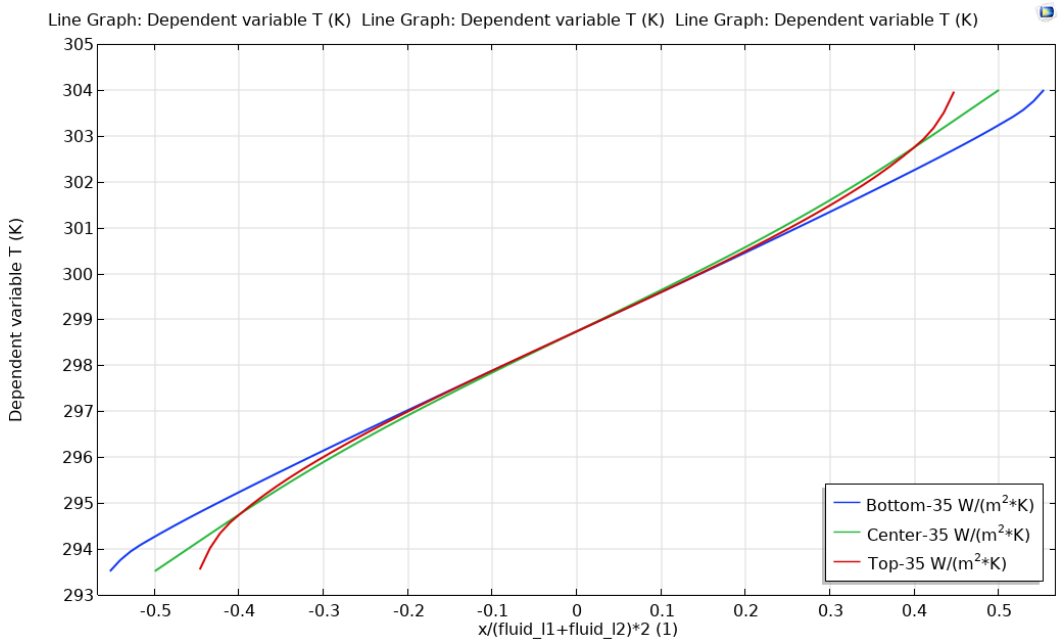

Figure 3.7: T profile across the channel width at three different height: bottom (blue), middle (green) and top (red) of the channel. As one can notice the total temperature drop across the channel is around 10 degrees.

It is worth noting that with a set 20°C difference between the two peltier elements there is only a 10°C gradient across the channel, meaning that the heat transfer is not very efficient even according to the model. Efficiency in this model would imply a clear path for heat flow confined as much as possible in the microfluidic chip, with the only high resistance component represented by the water-filled channel. With better insulation the heat wouldn't leak in the polymeric plates as in Fig. 3.4, thus making the aluminum plates to conduct the heat only towards the chip. Furthermore, thicker aluminum plates would give more mass and hence more thermal energy to be stored inside them: this means more heat that can flow.

3.2.2 Temperature calibration

In order to measure the temperature inside the channel, a thermosensitive fluorescent molecule, Rhodamine B (RB) [58], was used. It was selected thanks to its linear behaviour in the range 0°C-100°C, meaning that the fuorophore intensity proportionally decreases with increasing T. To achieve a correlation between the RB solution intensity and the temperature, a calibration curve was needed. Thus, the two controllers were set to the same T, let them stabilize and then an image set (20 images) was

collected for that single temperature; this process was done from 20°C to 30°C, with steps of 2°C in between (total of six stacks of 20 images each). Each stack was averaged to get one single less noisy temperature-image representing the intensity at that T. Then the channel central line was found (Fig. 3.8a) and the channel was calculated with the same number of pixel to the left and right from the central line (for a total of 80% of a focused channel), as in Fig. 3.8b.

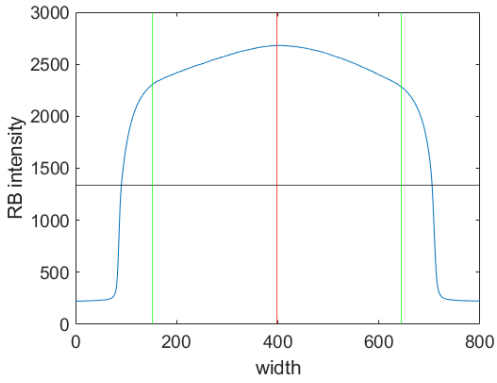

(a) Mean intensity along the length of the channel (blue), with threshold 50% of the maximum intensity in black. The channel central line (red) has been identified as the median of the positions vector above the threshold. The green lines are the considered side of the channel, obtained by taking 40% of the positions vector length both right and left from the central line. Thus the channel is 80% of the pixels above the threshold.

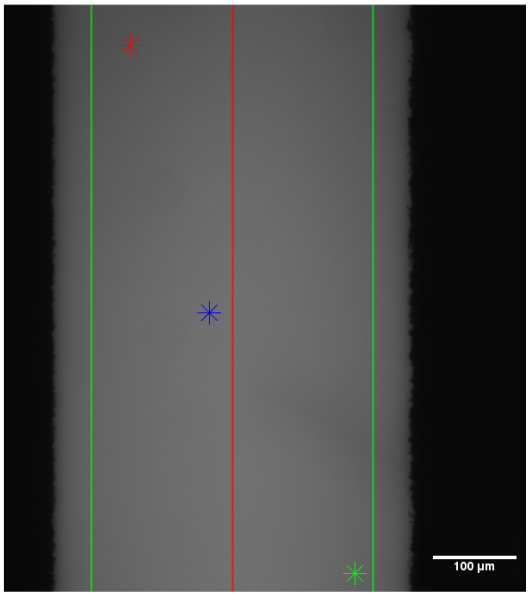

(b) Resulting cropped channel in a raw image. The central line (red) and the side walls (green) are calculated as explained in Fig. 3.8a. The red, blue and green markers correspond to three sample-pixels used to check the calibration curves. Scale bar is 100 µm.

Figure 3.8: Method to identify the channel for each image, applied in order to cope with the drift due to thermal bending.

This approach was taken in order to make sure that the same size channel was segmented every time, at roughly the same distance from the walls: not too close (to avoid the wall distortions due to the blurring), but not too far either (thus making the analysis non-significant). The next step was to calculate the calibration curve (a line) that would describe the relationship between T and channel intensity. Being a first order polynomial, only one coefficient and one offset parameters are needed. These were calculated pixel-wise, meaning that every pixel in the cropped image got its own calibration curve: to reduce the noise, an averaging filter was convoluted with every image. Then for every position in the image, the intensity at each T was fitted to extrapolate the slope and offset of the calibration curve for that single pixel. The result is a 3D coefficient matrix with a two component vector for every position of the cropped images. The calibration curves for the three highlighted pixels in Fig. 3.8b are shown in Fig.3.9, in which the different positions are color-coded.

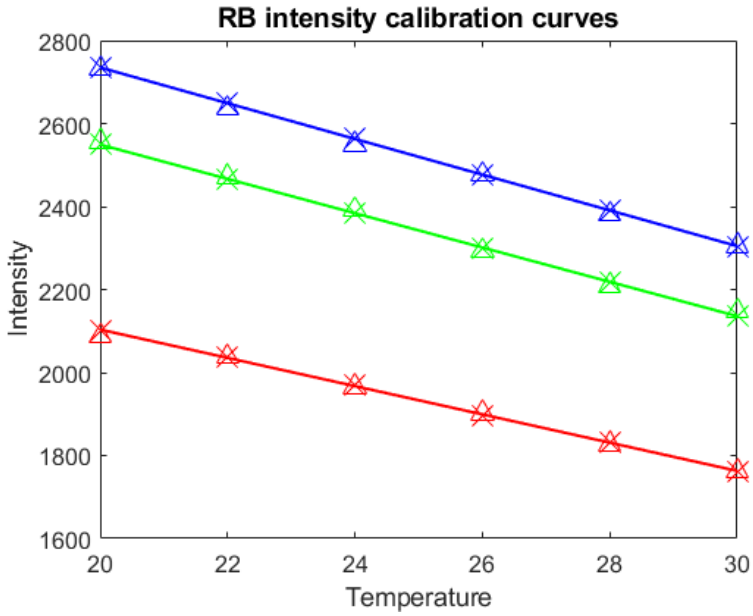

Figure 3.9: Three curves representing the RB intensity dependence on T. The color-code specify the position of the investigated pixel as in Fig. 3.8b. The triangles are the intensity value at the pixel before the neighbourhood averaging, while the crosses are the value after the filter was convoluted with the image.

This kind of approach was applied to avoid optical issues that could heavily impact the intensity distribution along the image: doing a "local" averaging smooths out the noise of a single pixel (already reduced by the image stacks mean), but the small dimensions of the neighbourhood prevent losing the particular intensity aberration that may be present in that region of the image. As shown in Fig. 3.9, the intensity from the mean image at a certain T slightly differs from the smoothed one with the local filtration: this latter perfectly fit in a first order polynomial in dependence on T. It is worth noting as well that the slope at different positions is roughly the same, with only different offsets: this is because the change in intensity heavily depends on the RB concentration, while the actual intensity value depends on the light optical path and distribution. With the coefficient matrix it was hence possible to take an image with an unknown T field on the channel (filled of course with a solution with the same RB concentration as the calibration) and then extract the temperature map, pixel by pixel.

3.2.3 Temperature gradient

The temperature gradient contour calculated by using the calibration matrix is shown in Fig. 3.10, in which it is possible to see the T gradient as a color-map (with the two peltier-controllers set to 16°C and 36°C, like in the model).

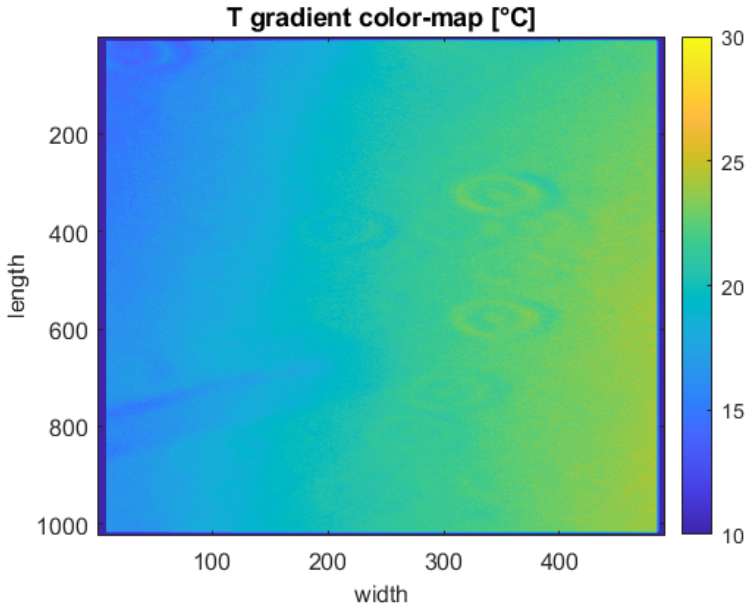

Figure 3.10: Temperature gradient color-map, in which every pixel intensity was correlated with its position-specific calibration curve from the coefficient matrix.

As one can see there are some circular aberrations in the map, due to the fact that there were some spots in the field of view (either on the optics or on the camera sensor): considering that the channel slightly moves during the temperature calibration acquisition, these spots are not in the same position all throughout the calibration stack. Thus these thin circular shapes are formed.

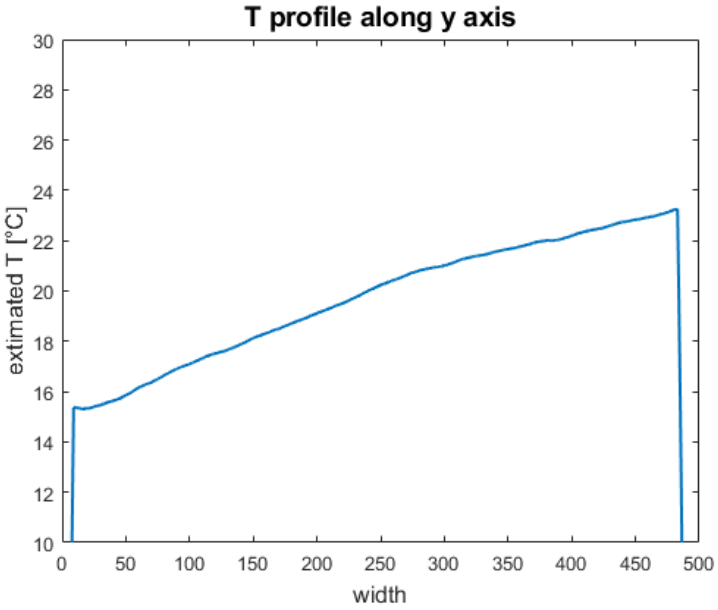

Figure 3.11: T gradient along the channel width, obtained by averaging temperature values in the length direction. As one can see, the gradient is roughly linear.

The averaged temperature in the channel as function of the width is shown in Fig. 3.11. It can be seen that the profile is quite linear, but the absolute values are definitely incorrect: it is impossible that the temperature on the left side (cold one) goes below 16, being this one the T set for the peltier

element. However, even if the absolute measured T might be incorrect, such a relative difference could be actually present inside the channel. A ΔT of roughly 8°C is reasonable if compared with the model prediction (roughly 10°C), considering that in reality there is no way to get a perfect thermal coupling between the aluminum plates and the chip: the real heat conduction would thus be less efficient than how much it was forecasted by the COMSOL simulations. Furthermore, the constant offset of the thermal resistances and the linear dependence of RB on T make plausible the fact that such a thermal gradient would be shifted in value (higher temperature), but keeping the same relative difference. Ultimately, it is the trend of the gradient and the magnitude of the difference that matters when checking the change of the thermo-physical properties along the channel width. As one can easily see in both Fig. 3.10 and 3.11, there are some issues at the boundaries due to the fact that the averaging filter, when going through the images, does zero-padding at the edges: thus the values calculated for such pixels loose sense completely (the measured temperature went down to -250°C)

Considering that the estimated temperature difference is about 8°C, the density difference in the liquid will not be large. Thus the driving force for the convective motion inside the channel, i.e. the difference in hydrostatic pressure due to the colder and hotter liquid columns side-by-side, is really low. To characterize this motion, the GDPT was performed and the recorded particle motion was very slow, as expected. As one can see in Fig. 3.12, the average velocity was below 1 µm/s. The particle movement is induced by a gradient in hydrostatic pressure generated by the water different densities in adjacent liquid columns across the channel.

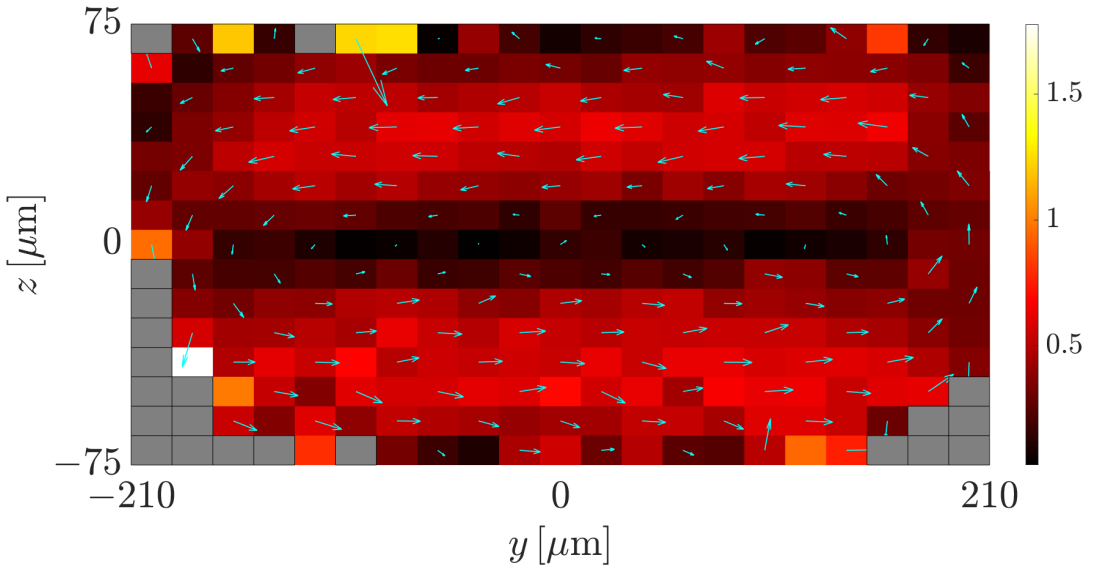

Figure 3.12: Thermal convective flow originating by the T gradient across the channel (the two controllers were set to 36°C on the right and to 16°C on the left). The particle (1µm-diameter polystyrene) motion was recorded with a sampling rate of 2 Hz and then tracked using GDPT.

This gravity-induced convection can be explained as follow: at the bottom of the channel there will be the largest density difference, with a pressure gradient from the denser (i.e. colder) liquid to the hotter one; at the walls the fluid gets either cooled or heated and gravity pushes it respectively down or up. The recorded motion resembles pretty well the theorized behaviour in such a situation,

to which everyone can relate from daily life, thinking of the air flow in a room heated by a radiator.

3.3 Acoustic actuation

A 2 MHz piezo-electric transducer was glued to the chip in order to make it vibrate and thus generating an acoustic standing wave in the acoustic cavity. The resonating frequency was found to be around 1.5 MHz, way off the PZT resonating frequency (around 2 MHz), meaning that it was impossible to get all the acoustic energy that the oscillating element was able to generate. As one can see in Fig. 3.13, in the channel used in this thesis work it was not possible to obtain a perfect acoustic field: the skewed walls are for sure affecting the sound waves resonance, resulting in a non-classical sound field and non uniform distribution of the acoustic energy density. A non-uniform acoustic energy causes the radiation force to have different components at different positions along the channel width, resulting in a focusing commonly called *snaky* focusing, meaning that the pressure node location along y changes depending on the channel length coordinate. Thus it was expected to have a difficult comparison between the results obtain with such a configuration and more established experiments (and the related published theory).

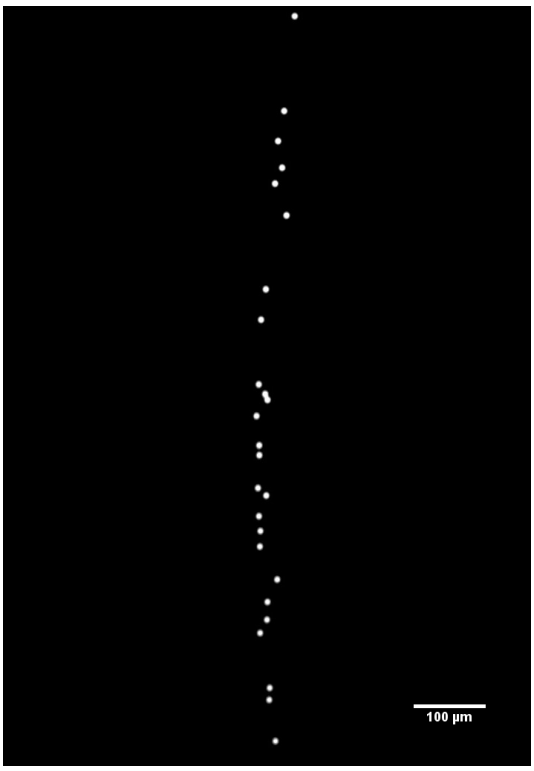

Figure 3.13: 5µm-diameter polystyrene particle focused in the channel: as one can clearly see, the particles are not focused at the same width-coordinate along the channel length (*sneaky* focusing). The PZT actuation was at 1.55 MHz with a 1 ms linear frequency sweep of 10 kHz. Scale bar is 100 µm.

In order to understand the fluid motion, smaller particles were used in this experiment as well. As with the thermal motion tracking, the same 1µm-diameter polystyrene particles (the motion of which

is expected to be dominated by acoustic streaming) were injected in the channel; the imaging was performed at the same spot as in the thermal recordings, with acoustic actuation at 1.562 MHz and 10 V peak-to-peak.

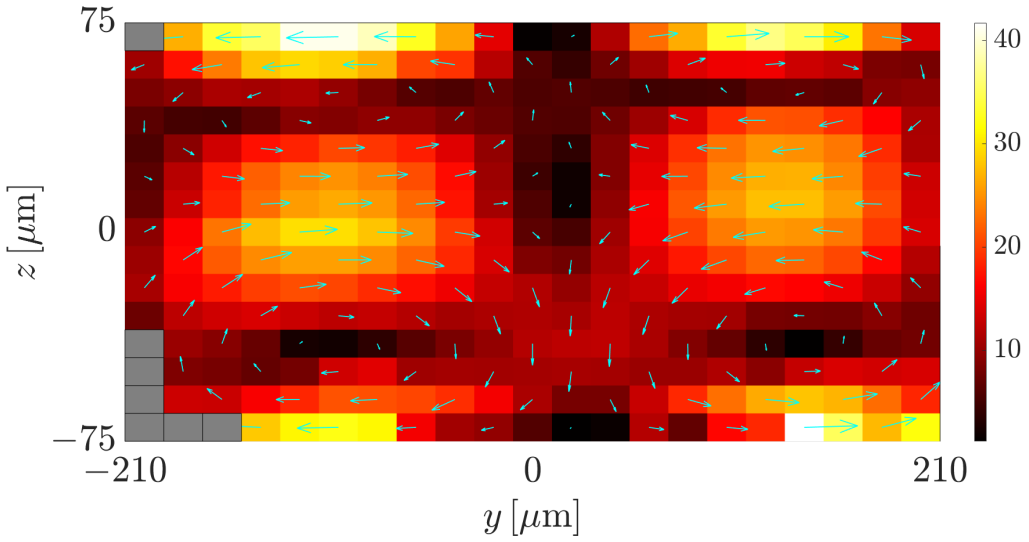

Figure 3.14: Acoustic streaming observed in the channel cross-section. The particle (1µm-diameter polystyrene) motion was recorded with a sampling rate of 10 Hz and then tracked using GDPT. Scale is in µm.

As one can easily see in Fig. 3.14, also in this case the four classic rolls appear with a standing wave along the width of the channel, as explained in section 2.2.4. It is worth noting that the two rolls at the bottom are slightly bigger than the ones in the upper part: this may be due to the trapezoidal cross-section of the channel, with the long base at the bottom. It is important to point out as well that there are some clear outliers at high velocity (top left and bottom right), that are at the boundaries of the channel where the tracking becomes more difficult, due to the high defocused shape of the particles. The average velocity at the channel mid height can be attested around 25 µm/s. Despite the cross-section not being rectangular, the measured acoustic streaming resembles pretty well the one expected and predicted by the theory, as reported in Fig. 2.6.

3.4 Thermal acoustic actuation

The novelty in this thesis work was the combination of the thermal gradient with the acoustic field. In order to do so, the temperature controllers were set at the same T as in the thermal field characterization, and then the piezo-electric actuator was turned on initially at the same frequency (1.562 MHz) as in the acoustic actuation. The temperature gradient in this case was measured with RB as previously showed, with the acoustic field on as well, to see if there was any interaction between the two. The temperature gradient map shown in Fig. 3.15 is comparable with the one without acoustic actuation (Fig. 3.10), with the only difference that the hot temperature seems to fade in a milder fashion (i.e. at the center there are mainly warm colors).

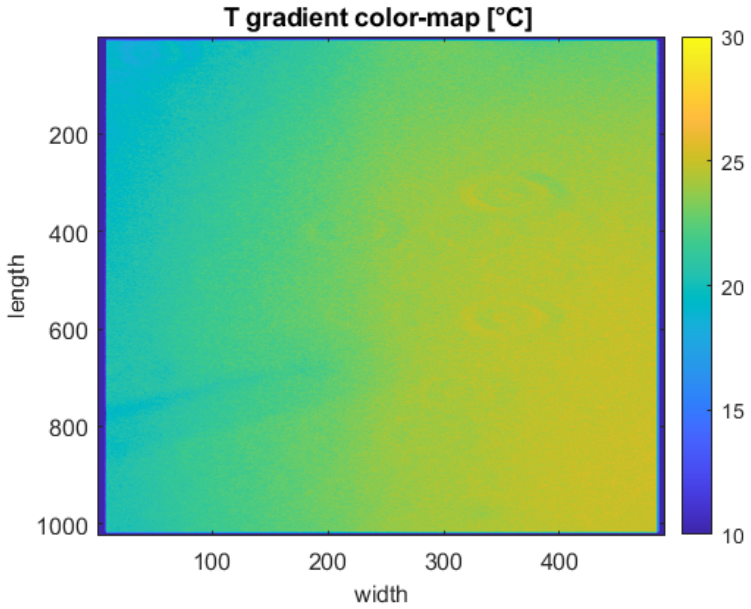

Figure 3.15: Temperature gradient color-map, in which every pixel intensity was correlated with its position-specific calibration curve from the coefficient matrix.

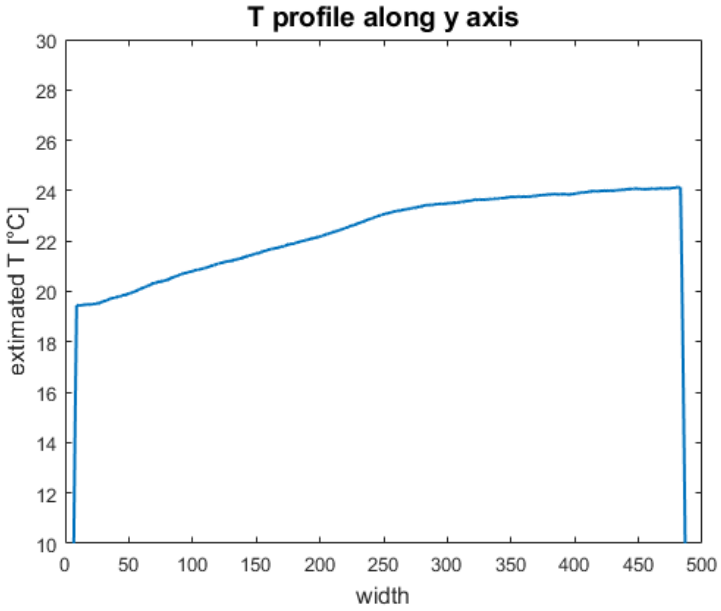

Figure 3.16: T gradient along the channel width, obtained by averaging temperature values in the length direction. As one can see, the gradient is roughly linear.

As one can see from Fig. 3.16, the temperature gradient is still roughly linear, but the major change is in the magnitude. If the ΔT was around 8°C with only the thermal field, now it is just about 4°C: the T at the hot wall has remained approximately the same, but the temperature at the cold one has increased by almost 4°C. This is most likely due to the fact that the PZT was placed on the chip side that was cooled down. With the actuation, the piezo-electric element heated up, thus conducting the heat to the channel and consequently decreasing the magnitude of the temperature gradient. This was an unexpected effect: it is known from literature the heating effect of piezo-electric transducers [85],

but it wasn't expected of this magnitude. This might be due to the high peak-to-peak voltage applied in order to obtain a good acoustic field, plus the non optimal gluing of the transducer to the chip and its use not at the optimal frequency. Thus, there can be a substantial damping effect of the PZT energy, from mechanical to thermal, which implies the heating of the element and, consequently, the conduction to the channel.

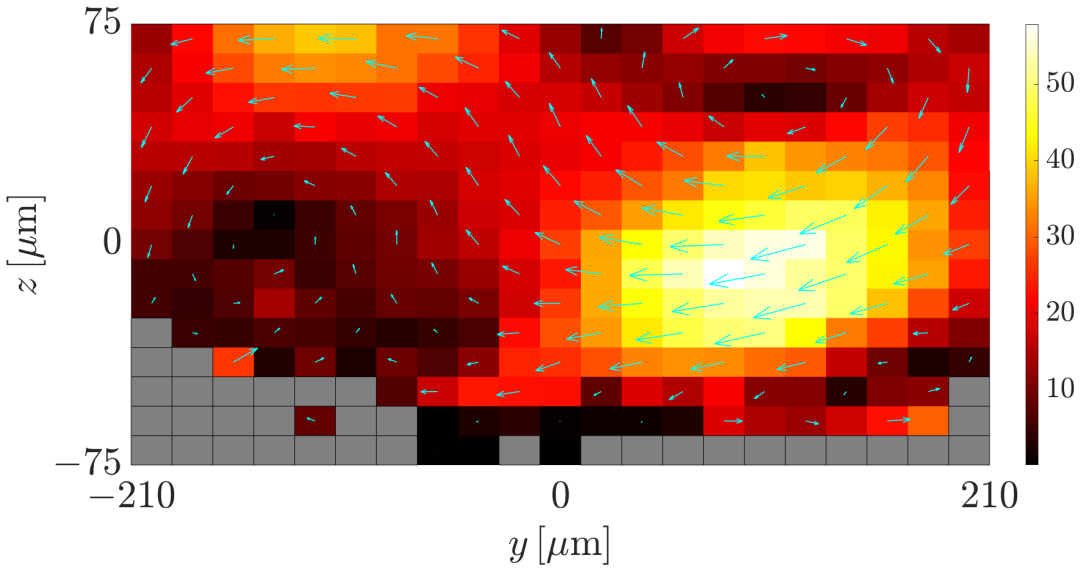

Figure 3.17: Thermal acoustic streaming observed in the channel cross-section. The particle (1µm-diameter polystyrene) motion was recorded with a sampling rate of 12 Hz and then tracked using GDPT. Scale is in µm.

The first thing to notice is the velocity magnitude distribution in the cross-section: as shown in Fig 3.17, the maximum velocity ($\approx$ 60 µm/s) is in this case at the mid-height of the channel. The trajectory seems to do some kind of "eight" shape, with two points at zero velocity almost anti-symmetric with respect to the center of the channel. It is worth noting that this particle tracking was more difficult than the previous ones, especially close to the bottom; this was due to the fact that the particles were sticking much more to the bottom and also the sampling rate was higher, thus necessarily diminishing the exposure time. The combination of these two effects caused the tracking algorithm to fail more often, resulting in a larger number of gray boxes (i.e. no velocity data).

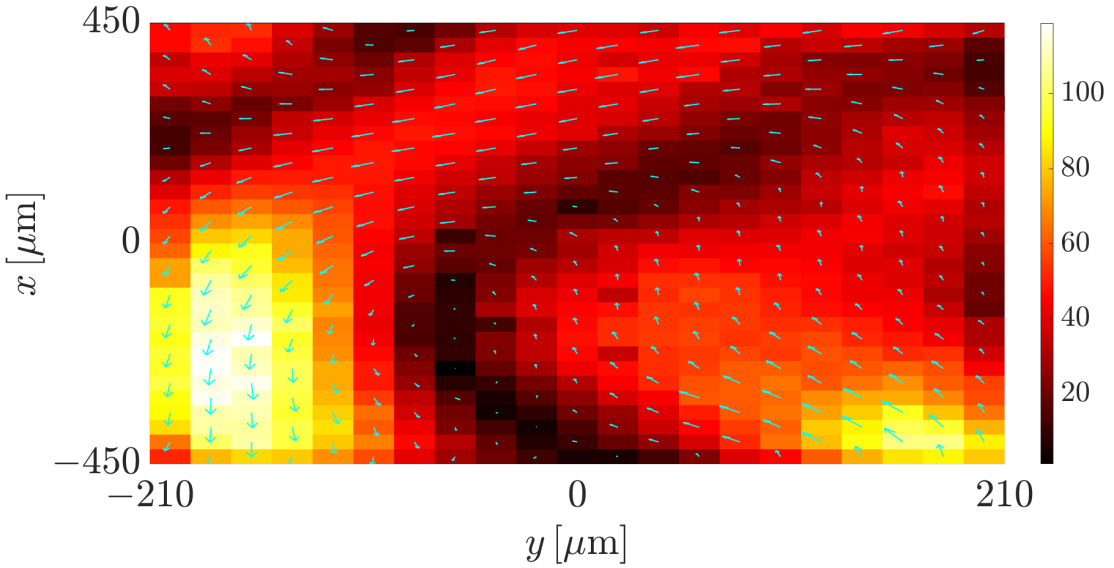

Figure 3.18: Thermal acoustic streaming observed along the channel length (x). The particle (1µm-diameter polystyrene) motion was recorded with a sampling rate of 12 Hz and then tracked using GDPT. Scale is in µm.

Looking at the in-plane motion (Fig. 3.18), one can observe that there is some fast moving fluid going along the length of the channel: all these differences in behaviour can heavily affect the recorded cross-sectional motion (already shown in Fig. 3.17). One of the first things to notice is the different magnitude of the velocity (the scale-bar goes roughly double than in the cross-sectional movement, with highest velocity > 100 µm/s). Then it is worth thinking about the flow pattern along the length of the channel, trying to understand the particle behaviour (and thus the fluid one). With a more classic chip and acoustic field, one would expect some more ordered plane rolls: starting from an acoustic focal point (positions along the length with highest acoustic energy density), the fluid would be pushed from the cold to the hot side due to the acoustic body forces (caused by the changes in both density and compressibility) and then circulating along the hot wall symmetrically both upstream and downstream along x. Then the fluid would be expected to go from the hot to the cold side in the position with the lowest acoustic energy density (and thus lowest body forces) and then flow along the cold wall to close the stream circulation. Nothing of this was observed during the experiments. However, these discrepancies between theory and experimental observations can have some justifications. First of all, in models the acoustic field is always perfect, with narrow resonance peaks and little or no contributions of the channel resonating modes along the length; in reality there is always some contribution (sometimes a lot) of these undesirable standing waves. Secondly, the geometry of the used chip is not optimal, meaning that it might induce some strange pattern in the streaming: different orientation of the liquid columns at the same T (they start parallel to one side wall, for then becoming perpendicular to the channel floor at the mid-width and in the end it would be skewed again with opposite orientation on the other wall) and non-classical acoustic streaming would add other components to the body forces.

The fluid motion was recorded in other two spots in which the fast flow more evidently appeared and the cross sectional velocity plots are shown in Fig. 3.19a and 3.19b.

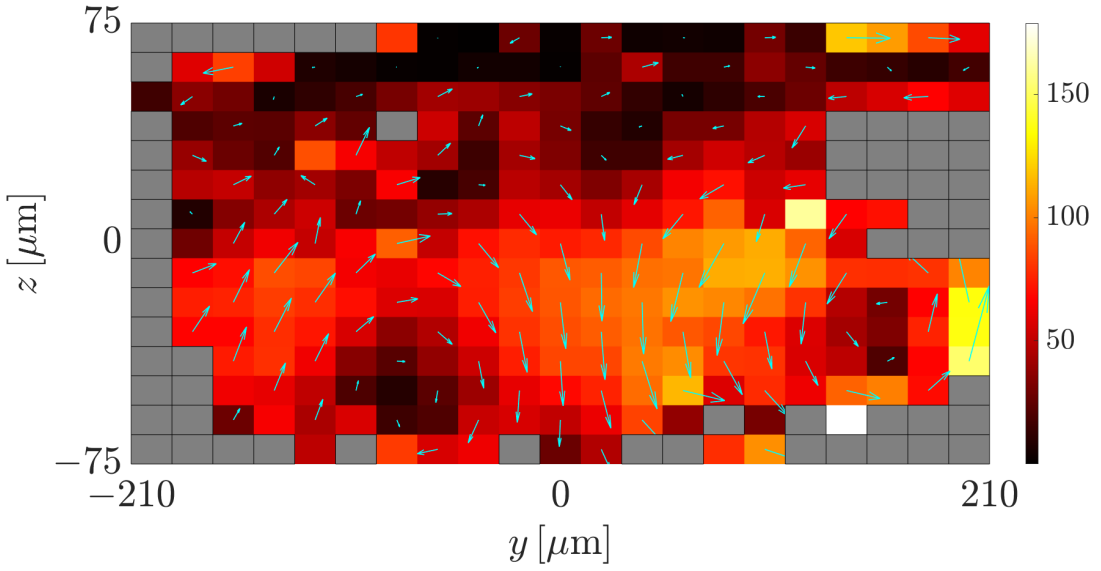

(a)

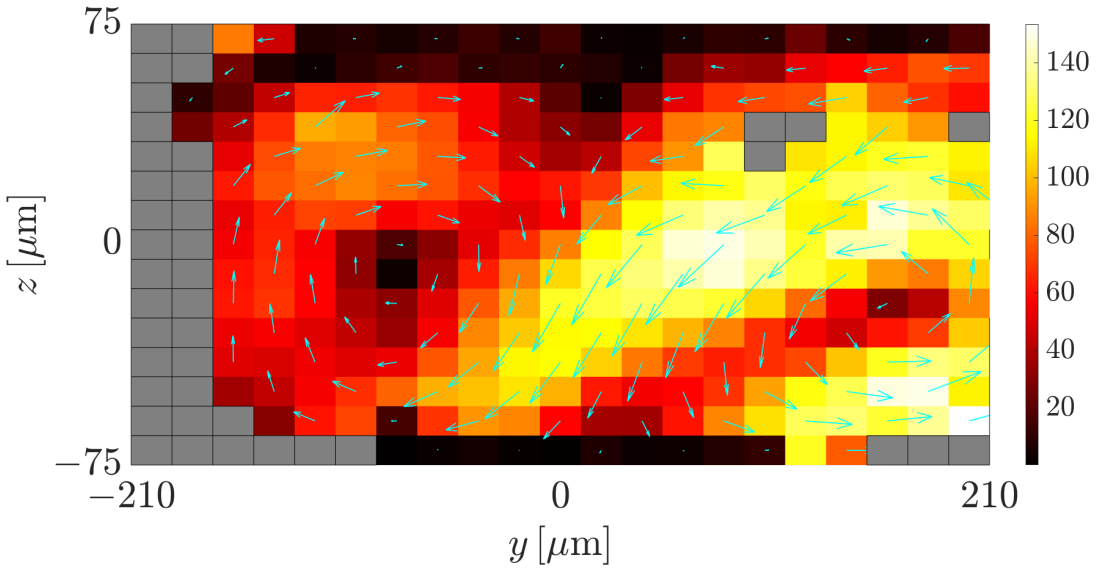

(b)

Figure 3.19: Thermal acoustic streaming observed in the channel cross-section in two different spots other than the one used for taking also the thermal and acoustic measurements. The particle (1µm-diameter polystyrene) motion was recorded with a sampling rate of 14 Hz and then tracked using GDPT. Scale is in µm.

These measured velocity fields demonstrate that very fast flow can occur even in the channel cross-section. Due to the high velocity (up to ≈100 µm/s in Fig. 3.19a and to ≈150 µm/s in Fig. 3.19b), the frame rate had to be increased, thus decreasing exposure time for image acquisition: this clearly causes a decrease in detected particles tracks, as proven by the higher number of grey boxes with no data in Fig. 3.19a and 3.19b. Particularly in Fig. 3.19b, the flow is clearly directed from the hot wall to the cold one, with really high velocity: the reason might be that in the channel section analyzed in that experiment there was the acoustic focal point. It is also quite interesting the behaviour along the height of the channel: being that the chip is in thermal contact with the aluminum only at the

bottom thin glass, there will be a temperature gradient also along the height of the channel. On the right side the higher T is at the bottom, while the top is little lower; on the contrary, on the left side it will be the bottom at the lowest T, with the top at a slightly higher one. These opposite gradients in temperature along z will generate changes in the thermo-physical properties of the fluid as well, thus not only creating body forces in the z direction, but, most of all, generating non-uniform acoustic body forces directed as the channel width depending on the height. Nonetheless, both these components should be negligible: the z-component of the acoustic body force is orders of magnitude smaller than the one parallel to the sound field and the thermal gradient along the channel height should be really small, thus creating really small changes in density and compressibility.

Chapter 4

Conclusion and Outlook

The temperature control system that was built during this thesis project has proved itself to be efficient and rubust. Especially the automation of such a system can be useful for non-expert users to manage the temperature controllers: the interface via LabView makes it easy and straightforward to set the T ranges independently for the two controllers, while at the same time transcribing on file the temperature recorded by the thermal resistances. Both the time intervals for changing the temperature and the sampling rate of the temperature probes can be easily adjusted in the user-interface. Regarding the precision of the temperature probes, for the future it would be necessary to check all of them with several known T to assure they all have the same offset and temperature dependent behaviour. Doing so, it would guarantee a better and more reliable thermal control system. Furthermore, more investigation is needed about which temperature should be taken as reference for the Rhodamine B calibration curves. In the current work, the temperature feed from the peltier controllers is used to find the relationship between RB intensity and temperature. This is wrong to a certain extent because there is no perfect thermal coupling between the holder and the chip, meaning that the temperature of the aluminum plate will always be different (even if slightly) from the one in the chip. This is due to non-uniform surface contact and heat dissipation: thermal paste had been tested to guarantee better thermal contact, but no net improvement has been observed. It would make more sense to link the temperature measured by the thermal resistance on top of the channel with the RB intensity. Despite realizing this, there was not enough space for placing the temperature probe on the chip in contact with the small region able to conduct heat in the holder. The aluminum underneath the chip had a length of 2 cm and, considering also the presence of the PZT element on the side and the need of a clean top surface for imaging, the thermal resistance had offered too big of an hindrance. Due to time restriction it was not possible to deepen the issue and find suitable solutions, so the RB intensity was linked to the controller T, acknowledging the non-correctness of the measure.

Regarding the holder, thermal bending represented an issue throughout the whole project. The used design, with very thin aluminum plates (400 µm) well insulated by the PMMA in which they are placed, was thought to limit the position changes among the dfferent set temperatures. However, the problem was not solved and both blurring and drifting kept occurring. This complicated the image processing for the temperature calibration, making necessary post-processing adjustments (like the channel cropping) to make the analysis coherent at different temperatures. Better solution for finding

the channel are needed, so that one can be sure to always take the same section when analysing the channel intensity. The used solution is satisfactory but for sure not perfect. Slight changes in the central line positioning can affect the whole calibration matrix, being that pixel that are not at the same position in the real image will be consider as such in the cropped one. The local averaging approach, though, tries to cope with this issue and with the optic aberrations present in the microscope. The obtained calibration curves as in Fig. 3.9 seem to confirm the goodness of such an approach.

The interaction between thermal and acoustic field is heavily dependent on the piezo-electric transducer positioning. As shown by the comparison between Fig. 3.11 and 3.16, the PZT actuation has an effect on the thermal gradient. This might be due to the convective contribution to the heat transport, considering the fairly comparable time scales for conduction and convection (considering the highest recorded velocity), as explained in Section 2.3.6. One sure reason is to be searched in the energy dissipation of the PZT: not working at the optimal resonance frequency can already increase the amount of generated thermal energy, but a great part of this energy is due to the gluing. Without an ideal mechanical coupling between the actuator and the chip, there is an higher risk for energy to be dissipated, thus generating heat that is then conducted to the channel through the glass. One possible solution would be to monitor also the temperature on the PZT by bonding a thermal resistance to it, so to understand when it needs to be switched off and cooled down. Furthermore, pulsed actuation can be used in order to lower the dissipated heat: this could be implemented in an automated way, controlling via LabView the wave-generator that excites the PZT. Of course for future experiments the PZT will be placed on the same side of the hot plate, so that its heating would not interfere as much on the temperature gradient; it will nonetheless affect the T distribution, but to a greatly reduced extend.

Confronting the particle trajectories and velocities used to map the fluid motion in the channel cross-section (Fig. 3.12, 3.14 and 3.17), some comments have to be made. The thermal gravity-induced convection (Fig. 3.12) has the lowest velocity, mainly due to the low driving force that moves the liquid: the realtive density difference due to the applied temperature gradient is quite small, as shown in Fig. 2.8a, so as it will be the difference in hydrostatic pressure which drives the motion.
The acoustic streaming (Fig. 3.14) has a velocity one order of magnitude higher than the thermal convective one. It has been proven that, even with a non-optimal channel geometry and some imperfections in the PZT-chip mechanical coupling, it is possible to obtain an acoustic streaming that resembles fairly well the theoretical one. A difference that can be noted is the non perfect symmetry between the higher and lower half of the channel: the bigger rolls at the bottom are most likely due to the larger bottom base (and thus different boundary conditions and streaming). It is impossible, though, to assert this with certainty due to the lack of theoretical background and consequent simulations done in such a geometry.
Regarding the interaction between thermal and acoustic field (Fig. 3.17), the first thing to comment on is the shape of the streaming: it seems to point from the hotter to the colder side. It is however tricky to draw any conclusion about this, mainly due to the large channel portion along the length that has been considered to extract such a plot ($\approx$900 µm). Large components of in-plane motion have been observed, as shown in Fig. 3.18. This latter is anyway a lot different from the trajectory that one would expect: as explained in the experimental section, it was expected to have some ordered in-plane rolls, going form cold to hot in the acoustic focal point (high energy density), then along the

walls until the places with lowest energy density, finally going back to the cold wall and closing the circulation, as schematised in Fig. 4.1.

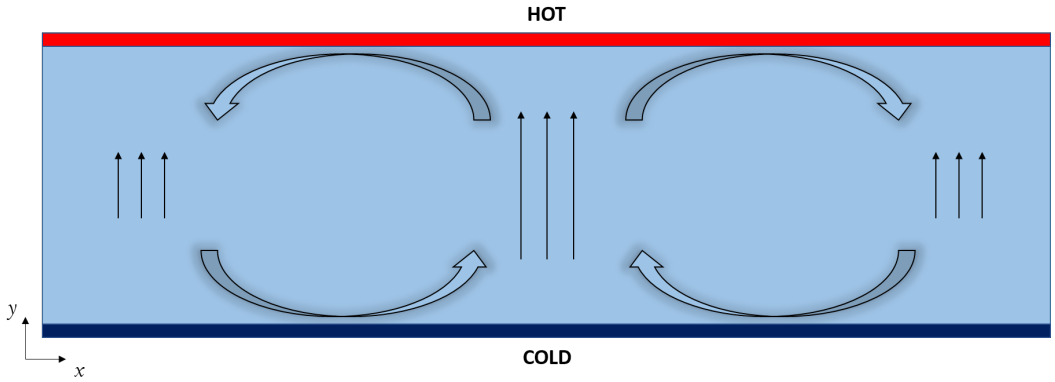

Figure 4.1: Scheme of the expected in-plane motion, with fluid rolls (light blue arrows), a thermal gradient (hot at the red wall, cold at the dark blue one) and an acoustic field. At the acoustic focal point in the center it would have been expected an higher acoustic body force (long black arrows), causing recirculation in the $x - y$ plane.

Furthermore, it is interesting to look at the velocity magnitudes in Fig. 3.17, 3.19a and 3.19b. Even considering the first one, displaying the slowest motion, it is clear that it's much faster (at least twice as much) than the one generated only by acoustic (Fig. 3.14). Comparing this latter one with the other two spots (Fig. 3.19a and 3.19b) and the velocity becomes one order of magnitude higher, going roughly up to 100 µm/s and 150 µm/s respectively. This is another demonstration of how much variability in the acoustic field is present along the channel length: such different velocities and shapes are worth deeper studies and theoretical explanations.

For future work, the holder could be modified to obtain direct contact between the silicon and the aluminum. Considering that the thermal bending happens even with small thickness and the heat path showed and commented in section 3.2.1, one can think of building the whole holder with two separate aluminum plates able to slide and perfectly clamp the chip between them. A step milled in the aluminum at the contact surface would guarantee both the clamping and the thermal coupling between the metal and the silicon. In Fig. 4.2 one can see the temperature map of such a system, as predicted by the COMSOL model with the same gradient (36 °C on the right and 16°C on the left).

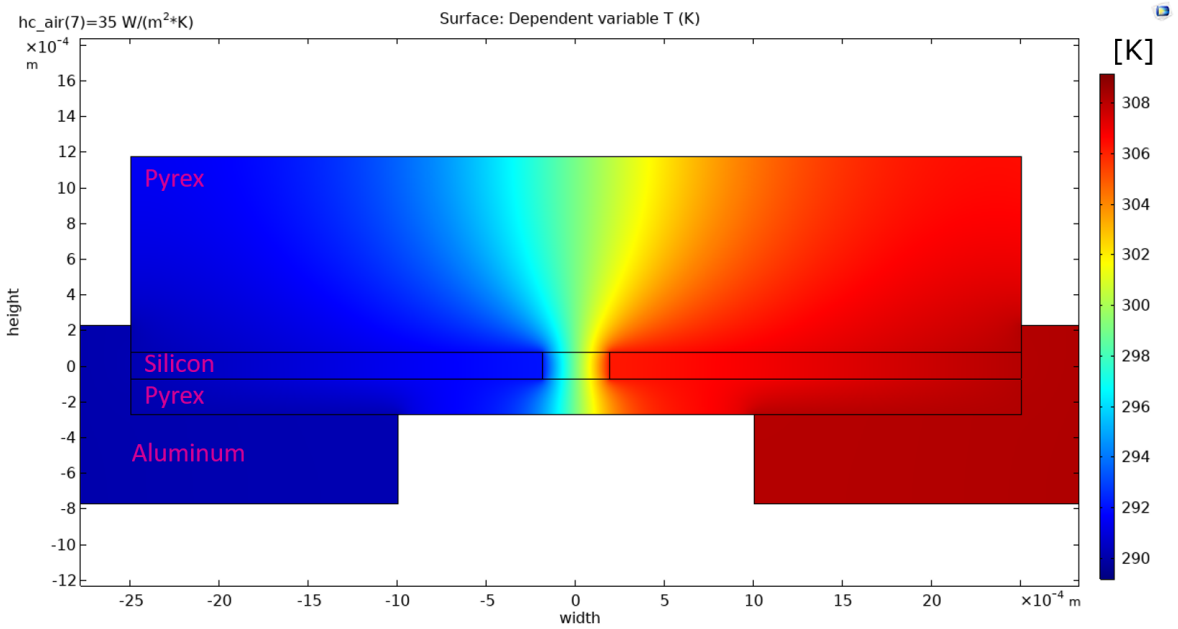

Figure 4.2: Temperature map for the new holder concept. At the side of the chip one can see the two aluminum plates with the step to allocate the glass-silicon-glass chip. This feature allow direct contact between silicon and aluminum, thus enabling an heat flux to go preferably through this path. A standard rectangular cross-section channel has been modelled. The different materials of the chip are indicated in magenta.

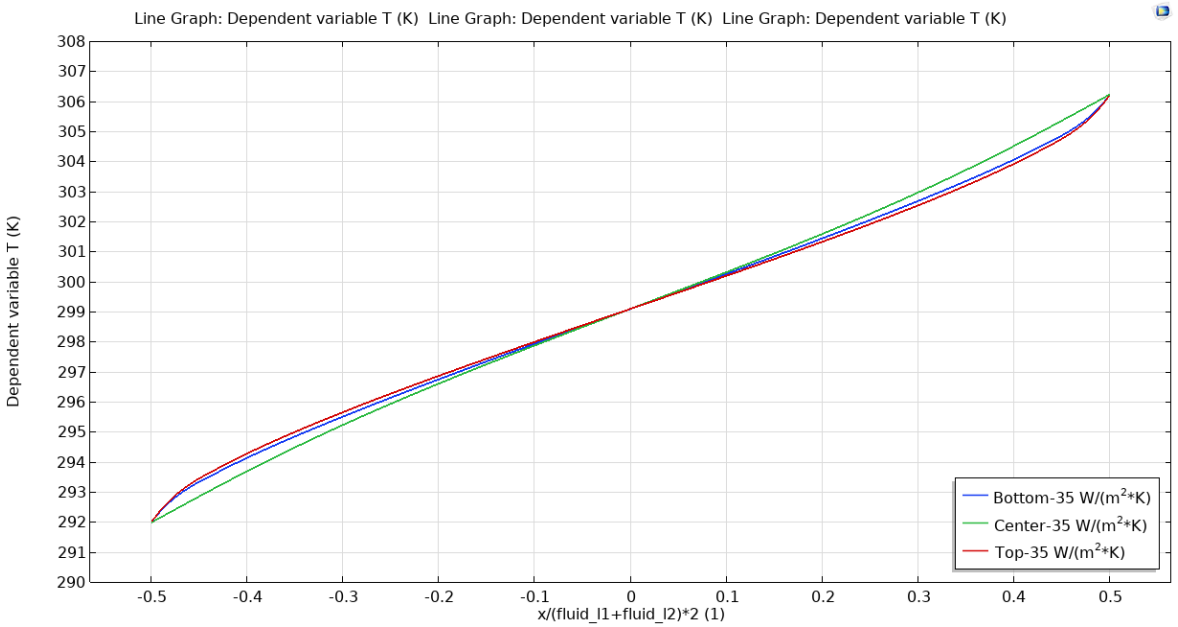

Figure 4.3: Temperature plot along the width of the channel with the new holder concept. As one can notice, the T is predicted perfectly linear in the center, while at the bottom and top of the channel there are some non-linearities due to heat dissipation.

As shown in Fig. 4.3, the temperature drop basically occurs just across the channel, with a T trend between the walls. Here it is possible to see that the temperature difference is almost 15°C, 75% of the ΔT set between the two peltier elements. This is due both to the fact that a more bulky

aluminum plates would have the possibility to conduct more heat, but mainly to the thermal coupling between aluminum and silicon: Al-Si-Al would be the thermal path with lowest resistance and the channel is in between. This configuration would imply that the preferable way for heat conduction has to go through the channel, thus generating there a thermal gradient.

Another substantial improvement would be to use a chip with a rectangular cross-section channel. This would make the thermal gradient have components only in the width direction, but most of all it would allow fair comparison between the generated acoustic field with the established literature (in which most of the silicon-glass chips have rectangular cross-section channels). Furthermore, with suitable channel geometry, the PZT element could be used closer to its resonance frequency, thus greatly diminishing the energy damping (hypothesising a better gluing, of course). This, combined with a more regular geometry, would greatly increase the acoustic energy density inside the channel and make it less dependent on the position for the same frequency. Looking at the issue from another perspective, it will be much easier to find a good resonance frequency at which the energy density is high if the acoustic field is not highly dependent on the position along the length.

Better understanding of the interaction between inhomogeneity and acoustic field could open up a better solution for cells sorting. Furthermore, the ability to enhance the acoustic effects due to density and compressibility gradient could give researchers the possibility to manipulate particles in the nanometric scale, such as vira and extracellular vesicles. Thermal gradients have been proved to be a reliable and stable way to generate inhomogeneity in microfluidic systems. Further studies in more standard conditions are needed to understand better this interaction and hence to be able to apply it in biomedical devices. Exciting new way to apply such an approach could involve micro-heaters embedded in the microfluidic system or electromagnetic heating such as lasers, able to localize the temperature increase in 3D spots with micrometric precision. The author of this thesis is sure that the Acoustofluidic group at Lund University will soon master this technique and apply it in the near future, enlarging the medical research capabilities with new useful tools.

Appendix A

Materials and Methods

This thesis work had been conducted at the BME deparment at Lund University, with the resources and tools already available in the E-house or purchased by my supervisor Per Augustsson.

Microfluidic device

The chip used was produced by silicon etching through a 150 µm thick silicon buffer, at which two Pyrex glass lids (thickness of 200 µm and 1100 µm) were anodically bonded. Thus, the chip thickness was 1450 µm, while the length was 7 cm and the width 5 mm. The channel, for which the trapezoidal cross-section has already been explained in chapter 3, had the following dimensions: length 65 mm, depth 150 µm and the width was 420 µm at the ceiling and 520 µm at the bottom (Fig. 3.1). The inlets were done on the thickest glass-lid and silicon tubing (VWRI 228-07, outer diameter 3 mm, inner diameter 1 mm) was glued with silicon glue (ELASTOSIL, A07, Wacker, Germany) to allow easy fluidic connections. The tubing to conduct the fluids to the inlet and form the outlet was in Teflon (SUPELCO, outer diameter 1.58 mm, inner diameter 0.5 mm). On thick glass a piezo-electric transducer, PZT (PZ26, FerropermPiezoceramics, Denmark), was glued with rapid glue (Loctite Bruch-on Super Glue, Henkel Corporation, Connecticut) slightly on the side to not cover the channel for visualisation.

Holder design and fabrication

Autodesk® Fusion 360™ was used to design the holder, from the drawing to the CNC milling commands set-up. The milling machine used was SOLECTRO ICP4030. The polymeric base was mainly a parallelepiped (140mm x 110 mm x 3 mm) made of PMMA XT, while the two metals plates (isosceles trapezoidal face, with bases of 4 and 2 cm and height if 5 cm, and thickness 400 µm) were made in aluminum 6082-T6. Two pockets with the Al plates dimensions were engraved on the polymeric support and a 1 mm slot was cut through in between those, to allow perfect heat decoupling. The metal plates were glued with rapid glue (Loctite Bruch-on Super Glue, Henkel Corporation, Connecticut) to the PMMA base onto the predisposed pockets.

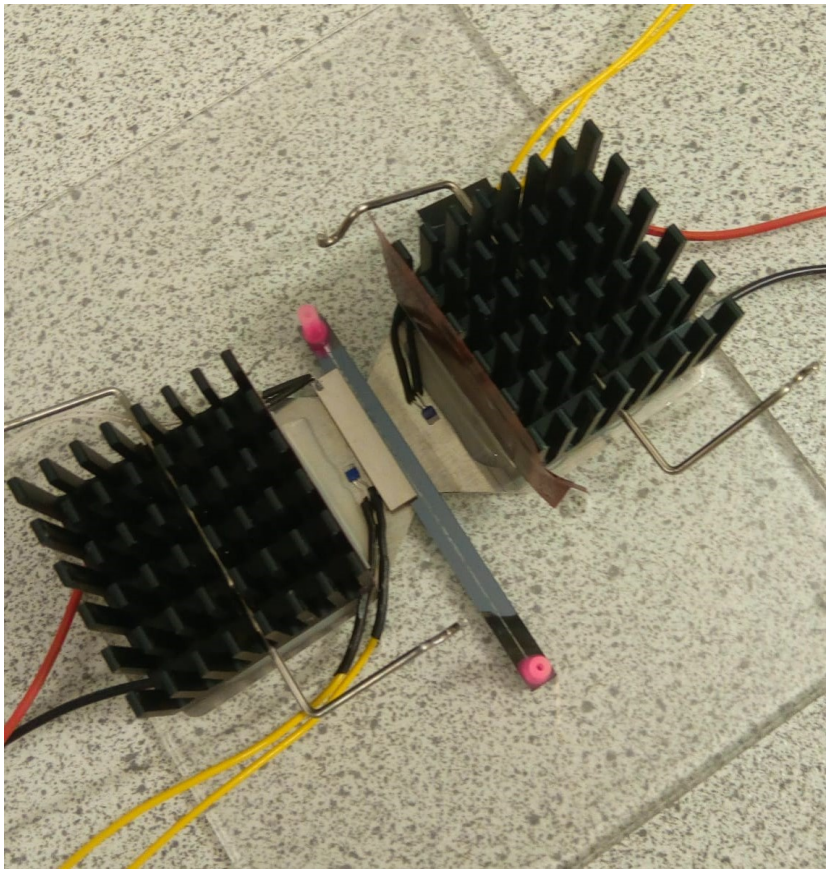

Figure A.1: Set-up that was built and used for this thesis. On the side of the chip one can see the two heat sinks that lie on the peltier elements, the thermo-resistances Pt1000 (with yellow wires) used to give feedback to the temperature controllers. On the chip it is possible to notice the piezoelectric transducer (white), glued on one side of the chip to allow visualisation.

Water	
ρ	$996.79\ kg\ m^{-3}$
κ	$4.5138e-10\ Pa^{-1}$
c_p	$4180.9\ J(kg\ K)^{-1}$
k_{th}	$0.60814\ W(m\ K)^{-1}$
c	$1499.3\ m\ s^{-1}$

Table A.1: Water properties set in the COMSOL model at T=26°C.

Pyrex	
ρ	$2230\ kg\ m^{-3}$
c_p	$800\ J(kg\ K)^{-1}$
k_{th}	$1.14W(m\ K)^{-1}$
α	$6.3901e-7\ m^2\ s^{-1}$

Table A.2: Pyrex properties set in the COMSOL model at T=26°C.

Silicon	
ρ	2329 $kg\ m^{-3}$
c_p	750 $J(kg\ K)^{-1}$
k_{th}	$149W(m\ K)^{-1}$
α	$8.5301e-5\ m^2\ s^{-1}$

Table A.3: Silicon properties set in the COMSOL model at T=26°C.

Aluminum	
ρ	2700 $kg\ m^{-3}$
c_p	900 $J(kg\ K)^{-1}$
k_{th}	$237W(m\ K)^{-1}$
α	$9.7531e-5\ m^2\ s^{-1}$

Table A.4: Aluminum properties set in the COMSOL model at T=26°C.

Experimental set-up for thermal field characterization

A 0.1 mMol Rhodamine B (laser grade, 99+%, ACROS organics, $M_w = 478.68$) solution was used. The microscope was an Olympus BX51WI, with motorized z-stage (ES10ZE, PRIOR Scientific) and light Olympus TH4-200 for bright field and CoolLED pE-4000 for fluoresce. Imaging was performed using an HAMAMATSU ORCA-ER C4742-95 digital camera controlled via MicroManager 2.0 gamma. External trigger was sent to the camera and to the pE-4000 for blinking light by a KEYSIGTH 33210A function/arbitrary waveform generator 10 MHz, controlled by LabView 2017 SP1 32-bit (National Instrument). One peltier element (CP393365H, CUI Inc.) was attached to each aluminum plate with thermal paste (High-DendityPolysynthetic Silver Thermal Compound, Artic Silver 5, USA) and silicon glue (ELASTOSIL, A07, Wacker, Germany). The thermal resistances used were Pt1000 (NB-PTCO-165, TE connectivity) and two of them were attached with rapid glue (Loctite Bruch-on Super Glue, Henkel Corporation, Connecticut) on the aluminum plates, one each, while the third one was embedded in paraffin () and used as mobile thermal probe, sending data to a 6 Digit Multimeter (Agilent, 34401A). The two peltier-element PID controllers (TC0806-RS232, CoolTronic) were fed 14 V by two DC power supplies: VELLEMAN PS925 (double output) and Hewlett Packard E3631A (triple output); the maximum output to the peltier elements was set to 3.5 V. The controllers received commands via LabView 2017 SP1 32-bit (National Instrument) and the feedback temperature from all the thermal resistances were recorded on .xlsx files.

The calibration needed to link Rhodamine B intensity with the corresponding T was done by setting both the controllers at the same temperature, waiting for T stabilisation (intervals from 60 to 240 s were tested) and then changing temperature. The range was between 20°C to 30°C, with step of 2°C. Images collected in two ways: either continuously sampled at 1 Hz or an image stack for each temperature was collected (sampling 2 Hz) at the last 10 seconds before changing T. The thermal gradient was then characterized by setting the two PID controllers at different T (in this report 36°C and 16°C), letting the temperature stabilize and then collecting an image stack (20 images) sampled at 2 Hz. The same procedure was done also with the acoustic field on.

The images were analysed with Matlab 2020a (MathWorks) via a custom made script. First the channel central line was identified in a in-focus image, considering the averaged intensity plot along the width and taking the median of the list of points in which the intensity was higher than half the maximum intensity. The channel width was also calculated from this distribution, meaning 80% of the length. Thus, a channel was selected to be 0.4 from each side of the central line: for each analysed image the central line was found and then the fix-dimension channel cropped (Fig. 3.8b). This process was useful to overcome the issue of blurring and sliding at the different temperatures. All the cropped images at the same T were averaged so that the noise would decrease. Then the pixel-wise calibration matrix was compiled: using the Matlab function `filter2`, an averaging filter was convoluted with the images. Then each locally-averaged pixel in each image was fit with the different T (Matlab function

`polyfit`) in order to get the first order polynomial approximating the Rhodamine B dependence on the temperature at each location (Fig. 3.9). This approach was needed in order to overcome the optics defects present in the set-up, that made the light intensity inhomogeneus. Lastly, the thermal gradient images were processed linking back the intensity with an estimate of the temperature at that specific pixel.

Experimental set-up for particle tracking

1 µm fluorescent beads (G1000 green fluorescent polymer microspheres, 1% solid, ThermoScientific, USA) were diluted 16 times in MilliQ (purified water produced in-house) to obtain a suitable concentration for effective tracking. The microscope was an Olympus BX51WI, with motorized z-stage (Marzhauser Wetzlar, Tango Desktop) and light Olympus TH4-200 for bright field and CoolLED pE-2000 for fluoresce. Furthermore, this microscope was equipped with cylindrical lens to give astigmatism in the focus. Imaging was performed using an HAMAMATSU ORCA-FLASH4.0 C13440 digital camera controlled via MicroManager 2.0 gamma. External trigger was sent to the camera by one channel of a function/arbitrary waveform generator Tektronix AFG3022B Dual Channel 25 MHz. The other channel was used to actuate the PZT when needed.
The GDPT approach [84] consists in getting a calibration stack obtained by having a steady particle (usually sticking to the bottom) and moving the stage by fixed steps (here 1 µm). Doing so it is possible to obtain a set of differently defocused particle shapes, representing different distances from where the focus was first set. Then, fixed the stage at the initial position, the particle are recorded with suitable sampling rate in the situation of study and then processed by an algorithm able to identify the shape of particles in every frame. Linking the shapes with the calibration stack, it is thus possible to reconstruct the behaviour of a particle in the depth, making complete 3D trajectories.
The particles were recorded in three different situations: only thermal field applied (36°C to 16°C) with 2 Hz sampling rate, only acoustic field applied (1.562 MHz and 10 V peak-to-peak actuation) with 10 Hz sampling rate and applying the two combined, with 12 or 14 Hz sampling rate. The image processing was done in Matlab 2018b using the GDPTlab GUI.

Bibliography

[1] R.G. Sweet, *High frequency recording with electrostatically deflected ink jets*, Rev Sci Instrum. 36 (2) (1965), 131–136.

[2] E. Bassous, H.H. Taub, L. Kuhn, *Ink jet printing nozzle arrays etched in silicon*, Appl. Phys. Lett. 31 (2) (1977), 135–137.

[3] S.C. Terry, J.H. Herman, J.B. Angell, *A gas chromatographic air analyzer fabricated on a silicon wafer, IEEE Trans Electron Devices*, 26 (12) (1979), 1880–1886

[4] A Manz, N Graber, H.M. Widmer, *Miniaturized total chemical analysis systems: a novel concept for chemical sensing*, Sensors and actuators B: Chemical, 1(1-6) (1990), 244-248.

[5] G. Core, V. Vitali, *Methods for selecting optimal operation frequencies in bulk acoustophoretic devices*, Master's thesis, Lund University, 2018.

[6] A. Lenshof, *Acoustic Standing Wave Manipulation of Particles and Cells in Microfluidic Chips*, PhD's thesis, Lund University, January the 30th 2009.

[7] P Pal and K Sato, *Silicon wet bulk micromachining for MEMS* , CRC Press (2017).

[8] S Franssila, *Introduction to microfabrication*, John Wiley and Sons (2010).

[9] F.K. Balagadde, L. You, C.L. Hansen, F.H. Arnold, S.R. Quake, *Long-term monitoring of bacteria undergoing programmed population control in a microchemostat*, Science 309 (5731) (2005), 137–140.

[10] Neil Convery and Nikolaj Gadegaard, *30 years of microfluidics*, Micro and Nano Engineering 2 (2019), 76-91.

[11] T.S. Hansen, D. Selmeczi, N.B. Larsen, *Fast prototyping of injection molded polymer microfluidic chips*, J. Micromech. Microeng. 20 (1) (2010).

[12] S.J. Li, A. Han, P.J. Kitson, et al., *Configurable 3D-Printed millifluidic and microfluidic "lab on a chip" reactionware devices*, Lab a Chip Pages 121218 (18) (2012), 3199–3522.

[13] E.C. Spivey, B. Xhemalce, J.B. Shear, I.J. Finkelstein, *3D-printed microfluidic microdissector for high-throughput studies of cellular aging*, Anal. Chem. 86 (15) (2014), 7406–7412.

[14] S. Kawata, H.B. Sun, T. Tanaka, K. Takada, *Finer features for functional microdevices*, Nature 412 (6848) (2001), 697–698.

[15] G. Xu, D. Nolder, J. Reboud, et al., *Paper-origami-based multiplexed malaria diagnostics from whole blood*, Angew Chemie – Int Ed. 55 (49) (2016), 15250–15253.

[16] A. Nilghaz, D. R. Ballerini, and W. Shen, *Exploration of microfluidic devices based on multi-filament threads and textiles: A review*, Biomicrofluidics 7, 051501 (2013).

[17] S. Xing, J. Jianga and T. Pan, *Interfacial microfluidic transport on micropatterned superhydrophobic textile*, Lab on a Chip 13 (2013), 1937-1947.

[18] A.W. Martinez, S.T. Phillips, G.M. Whitesides, *Three-dimensional microfluidic devices fabricated in layered paper and tape*, Proc. Natl. Acad. Sci. 105 (50) (2008), 19606–19611.

[19] A.H. Free, E.C. Adams, M.L. Kercher, H.M. Free, M.H. Cook, *Simple specific test for urine glucose*, Clin. Chem. 3 (3) (1957), 163–168.

[20] F.W. Payne, B. Ledden, G. Lamps, *Capabilities of Next-Generation Patch Pump: Improved Precision, Instant Occlusion Detection, and Dual-Hormone Therapy*, J Diabetes Sci Technol. 13(1) (2019), 49-54.

[21] G. Chen, J. Zheng, L. Liu, L. Xu, *Application of Microfluidics in Wearable Devices*, Small Methods 3 (2019), 1900688.

[22] M. Reches, K.A. Mirica, R. Dasgupta, M. D. Dickey, M.J. Butte, G.M. Whitesides, *Thread as a Matrix for Biomedical Assays*, Appl. Mater. Interfaces 2, 6, (2010), 1722–1728.

[23] C.S. Effenhauser, A. Paulus, A. Manz, H.M. Widmer, *High-speed separation of antisense oligonucleotides on a micromachined capillary electrophoresis device*, Anal. Chem. 66 (18) (1994) 2949–2953

[24] M.A. Northrup, M.T. Ching, R.M. White, R.T. Watson, *DNA amplification with a microfabricated reaction chamber*, Transducer '93-The 7th Int. Conf. on SolidState Sensors and Actuators, Yokohama, 1993, pp. 925–926.

[25] X. Qiu, M.G. Mauk, D. Chen, C. Liua, H.H. Bau, *A large volume, portable, real-time PCR reactor*, Lab on a Chip 22 (2010), 3170–3177.

[26] DD. Huh, *A human breathing lung-on-a-chip*, Ann Am Thorac Soc. 12 (2015), Suppl 1(Suppl 1), S42-S44.

[27] P: Rifes, M. Isaksson, G.S. Rathore et al. *Modeling neural tube development by differentiation of human embryonic stem cells in a microfluidic WNT gradient*, Nat Biotechnol (2020).

[28] R. Visone, G. Talo, P. Occhetta, D. Cruz-Moreira, S. Lopa, O.A. Pappalardo, A. Redaelli, M. Moretti, M. Rasponi, *A microscale biomimetic platform for generation and electro-mechanical stimulation of 3D cardiac microtissues*, APL Bioengineering 2 (2018), 046102.

[29] D. Huh, G.A. Hamilton, D.E. Ingber, *From 3D cell culture to organs-on-chips*, Trends in Cell Biology 21 (12) (2011), 745-754.

[30] H.W. Hou, A.A. Bhagat, A.G. Chong et al. *Deformability based cell margination–a simple microfluidic design for malaria-infected erythrocyte separation*, Lab Chip. 10(19) (2010), 2605-2613.

[31] L.R. Huang, E.C. Cox, R.H. Austin, J.C. Sturm, *Continuous particle separation through deterministic lateral displacement*, Science 304(5673) (2004), 987-990.

[32] C. Lay, C.Y. Teo, L. Zhu, X.L. Peh, H.M. Ji, B.R. Chew, R.M., H.H. Fenga, W.T. Liu, *Enhanced microfiltration devices configured with hydrodynamic trapping and a rain drop bypass filtering architecture for microbial cells detection*, Lab Chip 8 (2008), 830–833.

[33] S. Bhattacharya, S. Salamat, D. Morisette, P.Banada, D. Akin, Y.S. Liu, A.K. Bhunia, M. Ladische, R. Bashir, *PCR-based detection in a micro-fabricated platform*, Lab Chip 8 (2008), 1130–1136.

[34] T. Laurell, F. Petersson, A. Nilsson, *Chip integrated strategies for acoustic separation and manipulation of cells and particles*, Chem. Soc. Rev. 36 (2007), 492-506.

[35] A. Lenshof, C Magnusson, T. Laurell, *Acoustofluidics 8: Applications of acoustophoresis in continuous flow microsystems*, Lab Chip 12 (2012), 1210-1223.

[36] K. Petersson, O. Jakobsson, P. Ohlsson, P. Augustsson, S. Scheding, J. Malm, T. Laurell, *Acoustofluidic hematocrit determination*, Analytica Chimica Acta 1000 (2018), 199-204.

[37] C. Grenvall, J.R. Folkenberg, P. Augustsson, T. Laurell, *Label-free somatic cell cytometry in raw milk using acoustophoresis*, Cytometry 81A (2012), 1076-1083.

[38] M. Antfolk, C. Antfolk, H. Lilja, T. Laurell, P. Augustsson, *A single inlet two-stage acoustophoresis chip enabling tumor cell enrichment from white blood cells*, Lab Chip 15 (2015), 2102-2109.

[39] P. Augustsson, J.T. Karlsen, H. Su et al *Iso-acoustic focusing of cells for size-insensitive acoustomechanical phenotyping*, Nat Commun 7 (2016), 11556.

[40] J.S. Bach, H. Bruus, *Suppression of Acoustic Streaming in Shape-Optimized Channels*, Phys. Rev. Lett. 124 (2020), 214501.

[41] W. Qiu, J.T. Karlsen, H. Bruus, P. Augustsson, *Experimental Characterization of Acoustic Streaming in Gradients of Density and Compressibility*, Phys. Rev. Applied 11 (2019), 024018.

[42] J.T. Karlsen, P. Augustsson, H. Bruus, *Acoustic Force Density Acting on Inhomogeneous Fluids in Acoustic Fields*, Phys. Rev. Lett. 117 (2016), 114504.

[43] V. Miralles, A. Huerre, F. Malloggi, M.C. Jullien, *A Review of Heating and Temperature Control in Microfluidic Systems: Techniques and Applications*, Diagnostics 3 (2013), 33-67.

[44] C. Gosse, C. Bergaud, P. Löw, *Molecular Probes for Thermometry in Microfluidic Devices*, in: Volz S. (eds) Thermal Nanosystems and Nanomaterials. Topics in Applied Physics, vol 118 (2009). Springer, Berlin, Heidelberg.

[45] H. Mao, T. Yang, P. S. Cremer, *A Microfluidic Device with a Linear Temperature Gradient for Parallel and Combinatorial Measurements*, J. Am. Chem. Soc. 124 (16) (2002), 4432–4435.

[46] D. Vigolo, R. Rusconi, R. Piazza, H.A. Stone, *A portable device for temperature control along microchannels*, Lab Chip 10 (2010), 795–798.

[47] G. Maltezos, M. Johnston, K. Taganov, C. Srichantaratsamee, J. Gorman, *Exploring the limits of ultrafast polymerase chain reaction using liquid for thermal heat exchange: A proof of principle*, Appl. Phys. Lett. 97 (2010), 264101:1–264101:3.

[48] R.M. Guijt, A. Dodge, G.W.K. van Dedem, N.F. de Rooij, E. Verpoorte, *Chemical and physical processes for integrated temperature control in microfluidic devices*, Lab Chip 3 (2003), 1–4.

[49] G. Maltezos, A. Rajagopal, A. Scherer. *Evaporative cooling in microfluidic channels*, Appl. Phys. Lett. 89 (2006), 074107:1–074107:3.

[50] M.P. Dinca, M. Gheorghe, M. Aherne, P. Galvin, *Fast and accurate temperature control of a PCR microsystem with a disposable reactor*, J. Micromech. Microeng. 19 (2009), 065009:1–065009:15.

[51] T.-M. Hsieh, C.-H. Luo, J.-H. Wang, J.-L. Lin, K.-Y. Lien, G.-B. Lee, *Enhancement of thermal uniformity for a microthermal cycler and its application for polymerase chain reaction*, Microfluid. Nanofluid. 6 (2009), 797–809.

[52] C. Fermer, P. Nilsson, M. Larhed, *Microwave-assisted high-speed PCR*, Eur. J. Pharm. Sci. 18 (2003), 129–132.

[53] H. Kim, S. Vishniakou, G.W. Faris, *Petri dish PCR: Laser-heated reactions in nanoliter droplet arrays*, Lab Chip 9 (2009), 1230–1235.

[54] A.T. Ohta, A. Jamshidi, J.K. Valley, H.-Y. Hsu, M.C. Wu, *Optically actuated thermocapillary movement of gas bubbles on an absorbing substrate*, Appl. Phys. Lett. 91 (2007), 074103:1–074103:3.

[55] H.F. Arata, Y. Rondelez, H. Noji, H. Fujita, *Temperature Alternation by an On-Chip Microheater To Reveal Enzymatic Activity of β-Galactosidase at High Temperatures* Anal. Chem. 77 (2005), 4810.

[56] E.T. Lagally, C.A. Emrich, R.A. Mathies, *Fully integrated PCR-capillary electrophoresis microsystem for DNA analysis*, Lab Chip (2001) 1, 102-107.

[57] C.R. Smith, D.R. Sabatino, T.J. Praisner, *Temperature sensing with thermochromic liquid crystals*, Exp. Fluids 30 (2001), 190-201.

[58] D. Ross, M. Gaitan, L.E. Locascio, *Temperature Measurement in Microfluidic Systems Using a Temperature-Dependent Fluorescent Dye*, Anal. Chem. 73 (2001), 4117-4123.

[59] J.C. Fister, D. Rank, J.M. Harris, *Delayed fluorescence optical thermometry* Anal. Chem. 67 (1995), 4269-4275.

[60] T. Yamamoto, T. Nojima, T. Fujii, *PDMS–glass hybrid microreactor array with embedded temperature control device. Application to cell-free protein synthesis*, Lab Chip 2 (2002), 197-202.

[61] K. Swinney, D. J. Bornhop, *Quantification and Evaluation of Joule Heating in On-Chip Capillary Electrophoresis*, Electrophoresis 23 (2002), 613-620.

[62] R.B. Bird, W.E. Stewart, E.N. Lightfoot, *Transport Phenomena, 2nd Edition*, Jhon Wiley & Sons Inc. (2002).

[63] H. Bruus, *Theroretical Microfluidics*, Oxford Master Series in Physics 18 (2008).

[64] R. Barnkob, *Physics of microparticle acoustophoresis- Bridging theory and experiments*, PhD thesis, DTU Nanotech, August the 31st 2012.

[65] McGraw-Hill Concise Encyclopedia of Physics. © 2002 by The McGraw-Hill Companies, Inc.. Retrieved from https://encyclopedia2.thefreedictionary.com/ the 28/06/20.

[66] L.E. Kinsler, A.R. Frey, *Fundamentals of Acoustics*, Jhon Wiley & Sons Inc. (1950).

[67] P. Augustsson, *On microchannel acoustophoresis- Experimental considerations and life science applications*, PhD thesis, Lund University, December the 2nd 2011.

[68] H. Bruus, J. Dual, J. Hawkes, M. Hill, T. Laurell, J. Nilsson, S. Radel, S. Sadhalg, M. Wiklund, *Forthcoming Lab on a Chip tutorial series on acoustofluidics: Acoustofluidics—exploiting ultrasonic standing wave forces and acoustic streaming in microfluidic systems for cell and particle manipulation*, Lab Chip 11 (2011), 3579-3580.

[69] D.V. Assche, *Acoustophoretic manipulation of sub-micron particles*, Master's thesis, Lund University, 2017.

[70] L. V. King, *On the acoustic radiation pressure on spheres*, P Roy Soc Lond A Mat 147 (1934), 212–240.

[71] K. Yosioka, Y. Kawasima, *Acoustic radiation pressure on a compressible sphere*, Acustica 5 (1955), 167–173.

[72] L. P. Gorkov, *On the forces acting on a small particle in an acoustical field in an ideal fluid*, Soviet Physics - Doklady 6 (1962), 773–775.

[73] M. Settnes, H. Bruus, *Forces acting on a small particle in an acoustical field in a viscous fluid*, Phys Rev E 85 (2012), 016327.

[74] P. B. Muller, M. Rossi, Á. G. Marín, R. Barnkob, P. Augustsson, T. Laurell, C. J. Kähler, and H. Bruus, *Ultrasound-induced acoustophoretic motion of microparticles in three dimensions*, Phys. Rev. E 88 (2013), 023006.

[75] H. Bruus, *Acoustofluidics 2: Perturbation theory and ultrasound resonance modes* — Lab Chip 12 (2012), 20–28.

[76] H. Mitome, *The Mechanism of Generation of Acoustic Streaming*, Electron. Comm. Jpn. Pt. III, 81 (1998), 1-8.

[77] L. Rayleigh, *On the circulation of air observed in Kundt's tubes, and on some allied acoustical problems*, Philosophical Transactions of the Royal Society of London 175 (1884), 1–21.

[78] Mark F. Hamilton, Yurii A. Ilinskii, and Evgenia A. Zabolotskaya, *Acoustic streaming generated by standing waves in two-dimensional channels of arbitrary width*, The Journal of the Acoustical Society of America 113:1 (2003), 153-160.

[79] P.B. Muller, R. Barnkob, M.J.H. Jensen, H. Bruus, *A numerical study of microparticle acoustophoresis driven by acoustic radiation forces and streaming-induced drag forces*,Lab Chip 12 (2012), 4617-4627.

[80] Jonas T. Karlsen, Wei Qiu, Per Augustsson, and Henrik Bruus, *Acoustic Streaming and Its Suppression in Inhomogeneous Fluids*, Phys. Rev. Lett. 120 (2018), 054501.

[81] Jonas T. Karlsen, Per Augustsson, and Henrik Bruus, *Acoustic Force Density Acting on Inhomogeneous Fluids in Acoustic Fields*, Phys. Rev. Lett. 117 (2016), 114504.

[82] Wei Qiu, Henrik Bruus, Per Augustsson, *Three-dimensional Acoustophoretic Motion of Microparticles in Homogeneous and Inhomogeneous Fluids*, arXiv:2003.01931v1 [physics.flu-dyn] (2020).

[83] S.J. Blundell, K.M. Blundell, *Concepts in Thermal Physics*, Oxford Scholarship Online (2010).

[84] R. Barnkob, C.J. Kähler, M. Rossi, *General defocusing particle tracking*, Lab Chip 15 (2015), 3556.

[85] M. Evander, L. Johansson, T. Lilliehorn, J. Piskur, M. Lindvall, S. Johansson, M. Almqvist, T. Laurell, J. Nilsson, *Noninvasive Acoustic Cell Trapping in a Microfluidic Perfusion System for Online Bioassays*, Anal. Chem. 79 (2007), 2984-2991.

[86] R. Bitter, T. Mohiuddin, M. Nawrocki, *LabVIEW: Advanced programming techniques*, Crc Press (2006).

[87] A. Edelstein, N. Amodaj, K. Hoover, R. Vale, N. Stuurman, *Computer Control of Microscopes Using μManager*, Current Protocols in Molecular Biology 92 (2010), 14.20.1-14.20.17.